Authors' response to the referee's comment for Olin et al.: "Inversely modeling homogeneous H_2SO_4-H_2O nucleation rate in exhaust-related conditions"

We thank the referee for a beneficial comment and have corrected the manuscript according to it.

Referee report is in *black italic* and authors' response is in blue roman font. The marked-up manuscript and Supplement showing the changes and the new versions are included at the end of this file.

Referee 1 comments:

The authors have carefully addressed my criticism and revised the manuscript accordingly. Its message has been significantly clarified now and it might therefore be suitable for publication in ACP. Still, I have some concerns about the complexity of uncertainties in this study. It's not only the measurement of the sulfuric acid concentration that is still a challenging task but also size distribution measurement in the few nanometer size range is typically far from being quantitative. The size distribution results presented in this study are the best example. The authors themselves summarize all the critical aspects of size distribution measurement such as charging probability, sampling losses and instrument related transfer functions. The measured signal (number concentration at a certain DMA voltage) needs a sophisticated INVERSION algorithm to finally obtain a size distribution. In that sense it may be questioned whether the inverse modeling really brings the benefit one would hope for. Does the inversion of the inversion reduce error bars after all? I guess a careful analysis of measurement uncertainties is obligatory to get some feeling on the reliability of the results.

We have made a more careful examination on the particle size distributions in the smallest particle size range. Firstly, we found that there has been an error in our code used to import the Nano-SMPS data: the particle diameter vector has been misaligned with the concentration matrix; thus, all size distributions have been shifted towards larger diameters with a factor of about 1.2. After correcting this error, all Nano-SMPS distributions are now in 1.2 times smaller sizes. Fortunately, this correction narrows the gaps between the distributions obtained from the PSM+CPC system and from the Nano-SMPS, as is seen in Fig. AR1. Additionally, we have changed the CPC 3776 detection efficiency curve from the one reported by the manufacturer to the curve measured by Mordas et al. (2008) because it seems that the curve can deviate clearly from the manufacturer's curve, as seen by Hermann et al. (2007) and Mordas et al. (2008).

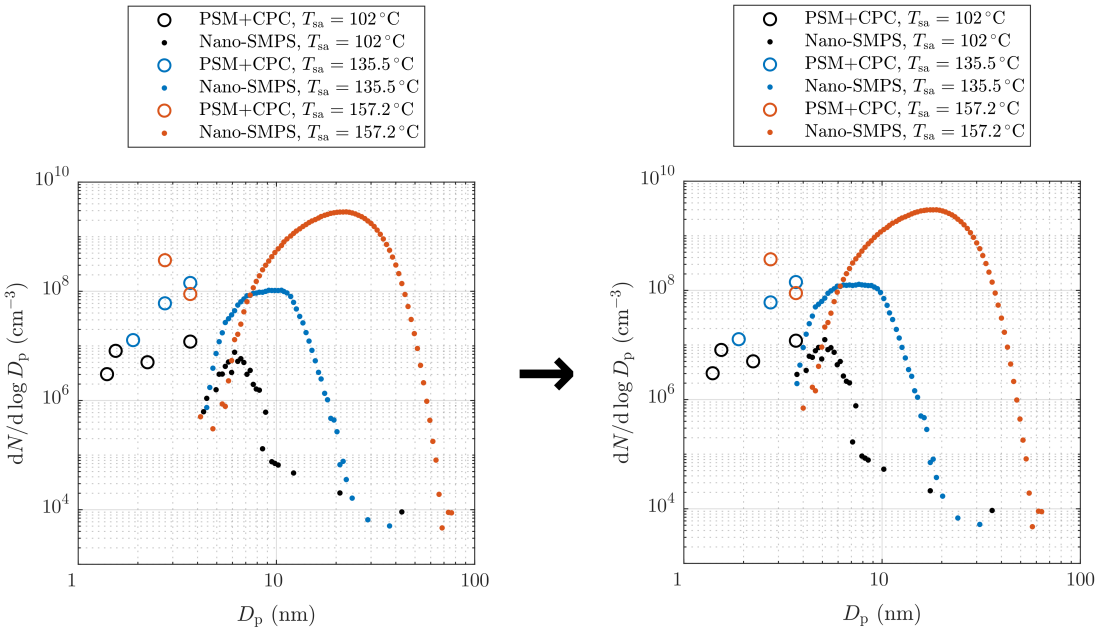

Figure AR1. The change of the example size distributions after the correction of the error in the code.

However, there are still some discrepancies between the distributions after the correction. We have made a careful analysis of the uncertainties involved in the size distribution measurements by calculating the error bars for all the size distribution points at specific diameters. For the PSM+CPC system, systematical errors, due to the uncertainties in the detection efficiency curves and in the diffusional loss correction function, are taken into account. For the Nano-SMPS system, systematical errors, due to the uncertainties in the radioactive charger efficiency, in the CPC 3776 detection efficiency curve, and in the diffusional loss correction function, are taken into account. Random error, caused by the instability in the particle generation and by the low counting statistics of the Nano-SMPS for the particle sizes having very low detection efficiency or low concentration, are also taken into account for the both devices. The detailed information on calculating the error bars is now included in the Supplement; the error bars for the example distributions are also shown here in Fig. AR2. Error bars are now added also to some main manuscript's figures for which the clarity of the figures can be maintained; the remaining figures with the error bars are added to the Supplement.

High error bars in the PSM+CPC distributions arise when the standard deviation of the measured concentrations are at a same level as the difference between the concentrations measured with the adjacent cut-diameters. Therefore, using all the measured concentrations typically cause high error bars if there is instability in the measured signal. Alternative way to obtain the size distribution in the PSM+CPC size range is to use only the concentrations measured with the smallest and with the largest cut-diameter. The alternative method will produce smaller error bars (shown as green shaded areas), but this will, of course, diminish the information on the shape of the distribution within that size range. Considering the error bars of the distributions, it seems that in the cases in panes (a) and (b), there are particles in the PSM+CPC size range although the Nano-SMPS distributions show log-normal-like edges for the smaller sizes. In the case in pane (c), although there are two size distribution points in the PSM+CPC distribution, particles in that size range are, according to the alternative method, inexistent. However, high error bars for the alternative method, caused by the standard deviation of the measured concentrations due to instabilities in particle generation, denote that the probability of the existence of particle in that size range is high. Nevertheless, the fraction of particles in that size range compared to the total particle count is, definitely, some orders of magnitude smaller than in the cases in panes (a) and (b). Due to the incapability of the Nano-SMPS in determining the size distribution reliably

in sub-10 nm diameter range, in all of the cases studied here, the PSM+CPC system is more suitable than the Nano-SMPS in measuring the size distribution for that particle size range.

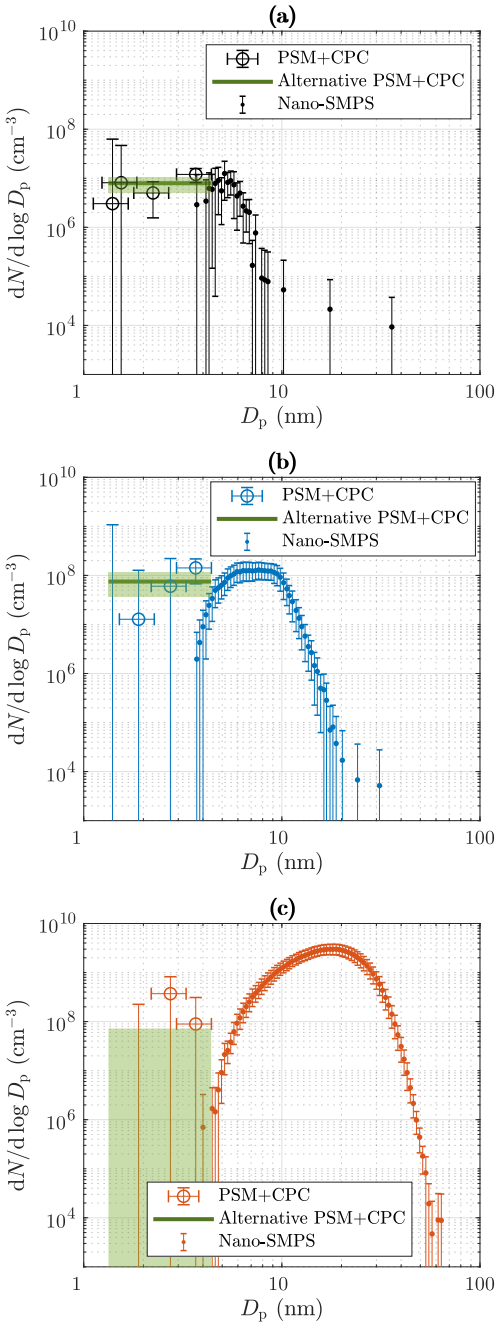

Figure AR2. The example size distributions shown with the error bars.

The inverse modeling in this work is based on predicting the concentrations measured with the different saturator flow rates of the PSM and with the CPC 3775 and on predicting the size distribution which is reported by the Nano-SMPS software. In other words, the inverse modeling does not try to predict the concentrations measured by the CPC 3776, acting as a particle counter in the Nano-SMPS system, as a function of time, or as a function of a specific DMA voltage. Concluding, there are two distinct parts of inversion involved: (1) the inverse modeling performed in this work and (2) the inversion algorithm which is included in the software of the Nano-SMPS device. These two inversion parts are not overlapped; thus, there is no "inversion of the inversion" in the analysis. The inverse modeling in this work takes the diffusional losses in the sampling lines and the detection efficiencies of the particle counters into account, while the inversion algorithm of the Nano-SMPS device takes at least the charger efficiency and the diffusional losses inside the device into account.

A consequence from correcting the error in the Nano-SMPS importing code is that because the particle diameters are now smaller, the diameters with the average mass of the distributions are also smaller now. Therefore, Fig. 13(b) and its interpretation is slightly changed now, as seen in Fig. AR3. The measured $D_{\bar{m}}$ values are now shifted towards the smaller diameters, which causes that the smallest diameters have now better agreement with the simulated diameters, but however, some diameters become less agreed with the simulated ones. The lining of the points is, nevertheless, the same: the fitted points form a slightly curved line in which the mid-ranged sizes are slightly overestimated. As some of the points now lie on the other side of the 1:1 line, minor changes to the text related to this figure are also made, but the final interpretation still remains as before.

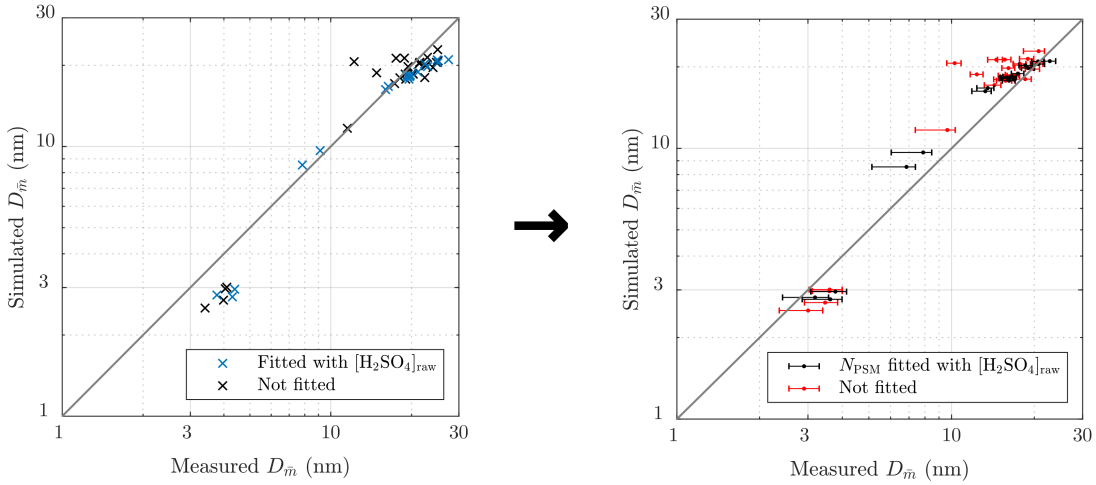

Figure AR3. The change of the diameters with the average mass after the correction of the error in the code. The error bars are also added, and the colors are also changed for better clarity.

References

Hermann, M., Wehner, B., Bischof, O., Han, H.-S., Krinke, T., Liu, W., Zerrath, A., and Wiedensohler, A.: Particle counting efficiencies of new TSI condensation particle counters, J. Aerosol Sci., 38, 674 – 682, https://doi.org/https://doi.org/10.1016/j.jaerosci.2007.05.001, http://www.sciencedirect.com/science/article/pii/S0021850207000705, 2007.

Mordas, G., Manninen, H., Petäjä, T., Aalto, P., Hämeri, K., and Kulmala, M.: On operation of the ultra-fine water-based CPC TSI 3786 and comparison with other TSI models (TSI 3776, TSI 3772, TSI 3025, TSI 3010, TSI 3007), Aerosol Sci. Tech., 42, 152–158, https://doi.org/10.1080/02786820701846252, 2008.

Inversely modeling homogeneous H_2SO_4-H_2O nucleation rate in exhaust-related conditions

Miska Olin[1], Jenni Alanen[1,a], Marja R.T. Palmroth[2], Topi Rönkkö[1], and Miikka Dal Maso[1]

[1]Aerosol Physics Laboratory, Physics Unit, Tampere University, P.O. Box 692, 33014 Tampere, Finland
[2]Bio and Circular Economy, Faculty of Engineering and Natural Sciences, Tampere University, P.O. Box 541, 33014 Tampere, Finland
[a]now at: AGCO Power, Linnavuorentie 8-10, 37240 Linnavuori, Finland

Correspondence: Miska Olin (miska.olin@tuni.fi)

Abstract. Homogeneous sulfuric acid-water nucleation rate in conditions related to vehicle exhaust was measured and modeled. The measurements were performed by evaporating sulfuric acid and water liquids and by diluting and cooling the sample vapor with a sampling system mimicking the dilution process occurring in a real-world driving situation. The nucleation rate inside the measurement system was modeled inversely using CFD (computational fluid dynamics) and the aerosol dynamics code, CFD-TUTMAM (Tampere University of Technology Modal Aerosol Model for CFD). The nucleation exponents for the concentrations of sulfuric acid and water and for the saturation vapor pressure of sulfuric acid were found to be 1.9 ± 0.1, 0.50 ± 0.05, and 0.75 ± 0.05, respectively. These exponents can be used to examine the nucleation mechanisms occurring in exhaust from different combustion sources (internal combustion engines, power plant boilers, etc.) or in the atmosphere. Additionally, nucleation rate can be expressed with the exponents as a function of the concentrations of sulfuric acid and water and of temperature. The obtained function can be used as a starting point for inverse modeling studies of more complex nucleation mechanisms involving extra compounds in addition to sulfuric acid and water. More complex nucleation mechanisms, such as hydrocarbon-involving, are observed with real vehicle exhaust and are also supported by the results obtained in this study. Furthermore, the function can be used to improve air quality models by using it to model the effect of sulfuric acid-emitting traffic and power generation on the particle concentration in urban air.

1 Introduction

Airborne particles are related to adverse health effects (Dockery et al., 1993; Pope et al., 2002; Beelen et al., 2014; Lelieveld et al., 2015) and various effects on climate (Arneth et al., 2009; Boucher et al., 2013). In particular, adverse health effects are caused by the exposure to vehicle emissions which increase ultrafine particle concentration in urban air (Virtanen et al., 2006; Johansson et al., 2007; Pey et al., 2009) in the size range with high probability of lung deposition (Alföldy et al., 2009; Rissler et al., 2012).

Vehicles equipped with internal combustion engines generate nonvolatile particles (Rönkkö et al., 2007; Sgro et al., 2008; Maricq et al., 2012; Rönkkö et al., 2014; Chen et al., 2017); however, volatile particles are also formed after the combustion process during exhaust cooling (Kittelson, 1998; Lähde et al., 2009), i.e., when the exhaust is released from the tailpipe. Thus, volatile particles are formed through nucleation process; hence, they are called here nucleation mode particles.

An important characteristic of fine particles is the particle size distribution, as it determines the behavior of particles in the atmosphere and particle deposition to the respiratory system. Modeling studies provide information on the formation and evolution of exhaust-originated particles in the atmosphere (Jacobson et al., 2005; Stevens et al., 2012). To model the number concentration and the particle size of nucleation mode, the governing nucleation rate needs to be known.

The detailed nucleation mechanism controlling particle formation in cooling and diluting vehicle exhaust is currently unknown (Keskinen and Rönkkö, 2010). The nucleation mode particles contain at least water, sulfuric acid (H_2SO_4), and hydrocarbons (Kittelson, 1998; Tobias et al., 2001; Sakurai et al., 2003; Schneider et al., 2005). Therefore, it is likely that these compounds are involved in the nucleation process, but, on the other hand, some of them can end up in the nucleation mode through the initial growth of the newly-formed clusters. The most promising candidate for the main nucleating component in the particle formation process occurring in diesel exhaust is H_2SO_4, as it has been shown that the H_2SO_4 vapor concentration in vehicle exhaust (Rönkkö et al., 2013; Karjalainen et al., 2014), fuel sulfur content (Maricq et al., 2002; Vogt et al., 2003; Vaaraslahti et al., 2005; Kittelson et al., 2008), lubricating oil sulfur content (Vaaraslahti et al., 2005; Kittelson et al., 2008), and exhaust after-treatment system (Maricq et al., 2002; Vogt et al., 2003) correlate with nucleation mode number concentration, at least in the cases when the test vehicle has been equipped with an oxidative exhaust after-treatment system. The sulfur contents of fuel and lubricating oil are connected to the H_2SO_4 vapor concentration in the exhaust because the combustion of sulfur-containing compounds produces sulfur dioxide (SO_2) that is further oxidized to sulfur trioxide (SO_3) in an oxidative exhaust after-treatment system (Kittelson et al., 2008), and SO_3 finally produces H_2SO_4 when contacting with water (H_2O) vapor (Boulaud et al., 1977).

Particle formation due to H_2SO_4 in real vehicle exhaust plumes and in laboratory sampling systems has been previously simulated by several authors (Uhrner et al., 2007; Lemmetty et al., 2008; Albriet et al., 2010; Liu et al., 2011; Arnold et al., 2012; Li and Huang, 2012; Wang and Zhang, 2012; Huang et al., 2014), but all of them have modeled nucleation as binary homogeneous nucleation (BHN) of H_2SO_4 and water. Other possible nucleation mechanisms include activation-type (Kulmala et al., 2006), barrierless kinetic (McMurry and Friedlander, 1979), hydrocarbon-involving (Vaaraslahti et al., 2004; Paasonen et al., 2010), ternary H_2SO_4-H_2O-ammonia (Meyer and Ristovski, 2007), and ion-induced nucleation (Raes et al., 1986). The choice of binary homogeneous H_2SO_4-H_2O nucleation in studies involving vehicle exhaust is mainly made because it has been the only nucleation mechanism for which an explicitly defined formula for the nucleation rate (J) can be presented (Keskinen and Rönkkö, 2010). An explicit definition is required when the nucleation rate in cooling exhaust is modeled, as the nucleation rate has a steep temperature-dependency according to theory (Hale, 2005) and experiments (Wölk and Strey, 2001). The nucleation rate of BHN is derived from classical thermodynamics; thus, the theory is called the classical nucleation theory (CNT). The nucleation rate according to the CNT is explicitly defined as a function of H_2SO_4 and H_2O vapor concentrations ($[H_2SO_4]$ and $[H_2O]$) and temperature (T). The derivation of the CNT contains, however, a lot of assumptions and it is thus

quite uncertain (Vehkamäki and Riipinen, 2012). The largest uncertainty rises from the capillarity approximation, i.e. the physical properties of small newly-formed critical clusters can be expressed as the properties of bulk liquid (Wyslouzil and Wölk, 2016). Comparing experimental and theoretical nucleation rates, the CNT underestimates the temperature-dependency (Hung et al., 1989) and overestimates the sensitivity of J on $[\mathrm{H_2SO_4}]$ (Weber et al., 1996; Olin et al., 2014). These discrepancies entail that theoretically derived nucleation rates need to be corrected with a factor, ranging in several orders of magnitude, to agree with experimental nucleation rates.

Conversely, the nucleation rates of the other nucleation mechanisms are typically modeled as (Zhang et al., 2012)

$$J = k[\mathrm{H_2SO_4}]^n, \tag{1}$$

where k is an experimentally derived coefficient and n is the nucleation exponent presenting the sensitivity of J on $[\mathrm{H_2SO_4}]$. According to the first nucleation theorem (Kashchiev, 1982), n is also connected to the number of molecules in a critical cluster; however, due to assumptions included in the theorem, n is not exactly the number of molecules in a critical cluster in realistic conditions (Kupiainen-Määttä et al., 2014). The value for k is typically a constant that includes the effect of T and $[\mathrm{H_2O}]$, i.e., relative humidity (RH), (Sihto et al., 2009; Stevens and Pierce, 2014). A constant coefficient can be a satisfactory approximation in atmospheric nucleation experiments, where T and RH remain nearly constants. However, T and RH in a cooling and diluting exhaust are highly variable; thus, a constant coefficient cannot be used. The nucleation exponents, n, for $\mathrm{H_2SO_4}$ obtained from the atmospheric nucleation measurements (Sihto et al., 2006; Riipinen et al., 2007) and from the atmospherically-relevant laboratory experiments (Brus et al., 2011; Riccobono et al., 2014) lie usually between 1 and 2, which are much lower than the theoretical exponents ($n \gtrsim 5$, Vehkamäki et al. (2003)).

The first step in examining nucleation mechanisms, other than the CNT, in vehicle exhaust using experimental data was performed by Vouitsis et al. (2005). They concluded that nucleation mechanisms having $n = 2$, including barrierless kinetic nucleation mechanism, can predict nucleation rates in vehicle exhaust. Later, Olin et al. (2015) and Pirjola et al. (2015) focused on obtaining nucleation rates inversely, i.e. an initial function for J acts as an input to the model and is altered until the simulated particle concentration and distribution correspond to the measured ones. These modeling studies are based on the experiments (Vouitsis et al., 2005; Arnold et al., 2012; Rönkkö et al., 2013) where the exhaust of a diesel engine was sampled using a laboratory setup containing an engine dynamometer and a diluting sampling system (Ntziachristos et al., 2004).

Inverse modeling is a preferable method in obtaining nucleation rates in a diluting domain over the method based on calculating J by dividing the measured number concentration with an estimated volume of a nucleation region, because the volume of a nucleation region depends on n also. In the case of inverse modeling, there is no need to estimate the nucleation region because the model simulates J at every time step, in a model using temporal coordinates, or in every computational cell, in a model using spatial coordinates. Pirjola et al. (2015) modeled the dilution system with an aerosol dynamics model using temporal coordinates and concluded that hydrocarbons could be involved in the nucleation mechanism, and n lies between 1 and 2. However, because particle formation in diluting vehicle exhaust involves strong gradients in temperature and the concentrations of the compounds involved, information in spatial dimensions is also required to fully understand the particle formation process. For this reason, Olin et al. (2015) simulated aerosol dynamics using computational fluid dynamics (CFD) and concluded

that n is 0.25 or 1, depending on whether solid particles acting as an condensation sink for sulfuric acid are emitted or not, respectively. These values are very low compared to other studies and to the first nucleation theorem that restricts n to at least 1. Values below unity imply that there can be other compounds involved in the nucleation mechanism in addition to H_2SO_4.

Ammonia (NH_3) involved in H_2SO_4-H_2O nucleation (ternary H_2SO_4-H_2O-NH_3 nucleation), has a notable effect if the H_2SO_4 concentration is low and the NH_3 concentration is high (Lemmetty et al., 2007; Kirkby et al., 2011). The H_2SO_4 concentration in the atmosphere is low enough for the effect of NH_3 to be relevant (Kirkby et al., 2011), but in vehicle exhaust higher H_2SO_4 concentrations make the effect of NH_3 probably negligible. However, more recent vehicles are equipped with the selective catalytic reduction (SCR) system which decreases nitrogen oxide emissions but, on the other hand, increases NH_3 emissions. Therefore, NH_3 can be involved in the nucleation process occurring in vehicle exhaust of vehicles equipped with the SCR system (Lemmetty et al., 2007). The SCR system was not included in the experiments of Arnold et al. (2012) and Rönkkö et al. (2013) mentioned earlier; thus, other compounds involving in the nucleation process in those experiments are more likely hydrocarbons rather than NH_3.

In this paper, an improved aerosol dynamics model, CFD-TUTMAM (Tampere University of Technology Modal Aerosol Model for CFD), based on our previous model, CFD-TUTEAM (Tampere University of Technology Exhaust Aerosol Model for CFD) described in the reference Olin et al. (2015), is presented. The main improvement in the model is its capability to model the initial growth of the newly-formed clusters modally using our novel representation of the particle size distribution, the PL+LN (combined power law and log-normal distribution) model described in the reference Olin et al. (2016).

Laboratory experiments designed for nucleation rate modeling purposes are presented, in which the examination of the nucleation rate was aimed towards pure H_2SO_4-H_2O nucleation instead of nucleation associated with some unknown compounds existing in real vehicle exhaust. Although the pure binary nucleation seems not to be the principal nucleation mechanism in real exhaust (Saito et al., 2002; Vaaraslahti et al., 2004; Meyer and Ristovski, 2007; Pirjola et al., 2015), neglecting the unknown compounds is reasonable at this stage of nucleation studies because the knowledge of the nucleation mechanism of the pure binary nucleation is still at a very low level, and it should be examined more to better understand the nucleation process in real exhaust. Adding only one additional compound to nucleation experiments would cause one additional dimension to the measurement matrix of all changeable parameters considered and would thus increase the complexity of the experiments. Similarly, adding the concentration of an additional compound to inverse modeling, the complexity and the computational cost of the simulations would increase significantly. Therefore, it is reasonable to begin the inverse modeling studies using only the pure binary nucleation mechanism. Additionally, although there are studies suggesting that other compounds are involved in the nucleation process in real vehicle exhaust, it has not yet been directly shown that nucleation rate would be lower or higher with the absence of those compounds. Comparing the experiments with pure H_2SO_4-H_2O nucleation to the experiments with real exhaust can provide information on that.

The pure H_2SO_4-H_2O nucleation was generated by evaporating H_2SO_4 and H_2O liquids and using the dilution system that mimics a real-world dilution process of a driving vehicle (Ntziachristos et al., 2004). A similar principle of generating H_2SO_4 by evaporating it from a saturator has been used in the study of Neitola et al. (2015), in which the concentrations of H_2SO_4 and H_2O and temperatures were kept in an atmospherically-relevant range. In this study, they were kept in a vehicle

exhaust-relevant range; thus, the output is an explicitly defined formula for the H_2SO_4-H_2O nucleation rate in exhaust-related conditions. The formula is in the form of

$$J([H_2SO_4],[H_2O],T) = k\frac{[H_2SO_4]^{n_{sa}}[H_2O]^{n_w}}{{p_{sa}}^{\circ}(T)^{m_{sa}}}, \quad (2)$$

which is based on the formula hypothesized by Olin et al. (2015) but with an additional exponent m_{sa} for the saturation vapor pressure of sulfuric acid (${p_{sa}}^{\circ}$) to take temperature also into account. In Eq. (2), n_{sa} and n_w represent the nucleation exponents for $[H_2SO_4]$ and $[H_2O]$, respectively. The exponents may also depend on the concentration levels but due to the unknown dependency, only constant values are considered in this study.

The formulation obtained from this study helps in finding the nucleation mechanisms occurring in real vehicle exhaust or in the atmosphere. Similarly, it can be used to examine particle formation in coal-fired power plant exhaust, which is known to contain H_2SO_4 too (Stevens et al., 2012). E.g., the values of the nucleation exponents obtained in this study can provide information on the nucleation mechanisms because the values differ with respect to different nucleation mechanisms. Another use of the formulation is in improving air quality models by using it to model the effect of sulfuric acid-emitting traffic and power generation on the particle concentration in urban air.

2 Laboratory experiments

Laboratory experiments were designed to enable the examination of the effects of three parameters ($[H_2SO_4]$, $[H_2O]$, and T) on the H_2SO_4-H_2O nucleation rate. The experimental setup is presented in Fig. 1.

2.1 Artificial raw exhaust generation

The artificial raw exhaust sample was generated (the top part of Fig. 1) by evaporating 98 % H_2SO_4 liquid and deionized Milli-Q water. H_2SO_4 was held in a PTFE container and water in a glass bottle. The liquids were heated to temperatures T_{sa} and 43 °C, respectively, which determine the concentrations in the gas phase theoretically through the saturation vapor pressure. Dry and filtered compressed air was flown through the evaporators and mixed before heating to 350 °C. 2.7 % of carbon dioxide (CO_2) was also mixed with a sample to act as a tracer to determine the dilution ratio (DR) of the diluters. CO_2 was selected because it has no effect on the particle formation process and because it exists in real exhaust as well.

The computational domain in the CFD simulation shown in the bottom part of Fig. 1 begins before the sample enters to the PTD; thus, the concentrations of H_2SO_4 and H_2O, temperature, pressure (p), and flow rate need to be known at that point due to the requirement of the boundary conditions in the CFD simulation. T and p were measured at that point, $[H_2O]$ was calculated from the measured RH, and the flow rate was calculated from the DR of the porous tube diluter (PTD) with the aid of measured CO_2 concentrations.

The temperature of the raw sample was 243 °C and the mole fraction of H_2O (x_w) was 0.036, in average. Temperature before the PTD was lower than the heater temperature, 350 °C, because the sample cooled in the sampling lines, but the temperature of 243 °C corresponds well with the temperature of real exhaust when released from the tailpipe. In NTP conditions, $x_w = 0.036$

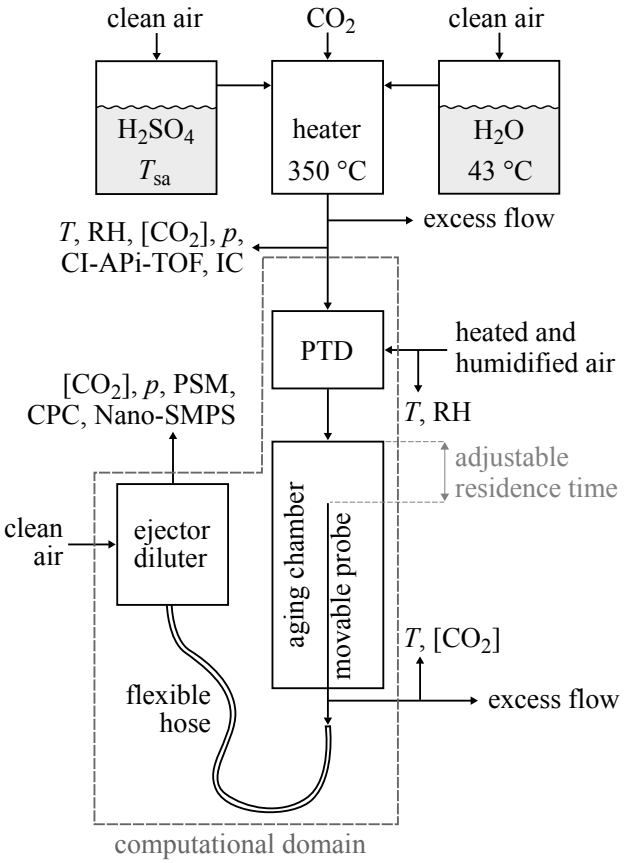

Figure 1. The experimental setup used to generate artificial exhaust and sample it with a diluting sampling system. The top part of the figure represents the artificial raw exhaust generation, which contains mixing and heating H_2SO_4 and H_2O vapors evaporated from liquids. The bottom part of the figure represents the raw exhaust sampling system, which consists of a porous tube diluter (PTD), an aging chamber, and an ejector diluter (ED). The computational domain of the CFD simulation is also shown in the figure.

corresponds to $[H_2O] = 9.0 \times 10^{17}\,\mathrm{cm}^{-3}$. The mole fractions in real diesel or gasoline exhaust range between 0.06 and 0.14, but the values higher than 0.036 with this experimental setup were not used, because a more humid sample caused the water vapor to condense as liquid water in the sampling lines.

The temperature of the H_2SO_4 evaporator, T_{sa}, was varied between $85\,^{\circ}\mathrm{C}$ and $164.5\,^{\circ}\mathrm{C}$ which correspond to the mole fractions (x_{sa}) between 2.2×10^{-7} and 1.1×10^{-5} in the raw sample. In NTP conditions, this range corresponds to the $[H_2SO_4]$ values between $5.7\times10^{12}\,\mathrm{cm}^{-3}$ and $2.8\times10^{14}\,\mathrm{cm}^{-3}$. These concentrations are higher than concentrations in real vehicle exhaust (typically between $10^8\,\mathrm{cm}^{-3}$ and $10^{14}\,\mathrm{cm}^{-3}$), because particle formation was not observed with the concentrations below $5.7\times10^{12}\,\mathrm{cm}^{-3}$. However, with real vehicle exhaust, in the same sampling system used here, particle formation has been observed even with the concentration of $2.5\times10^{9}\,\mathrm{cm}^{-3}$ (Arnold et al., 2012), indicating other compounds involving in the nucleation process.

The determination of $[H_2SO_4]$ in the raw sample in our experiment was not straightforward due to the uncertainties involved in the measurement of $[H_2SO_4]$. The detailed information on measuring it using a nitrate ion (NO_3^-) based chemical ionization Atmospheric Pressure interface Time-Of-Flight mass spectrometer (CI-APi-TOF, Jokinen et al. (2012)) and Ion Chromatography (IC, Sulonen et al. (2015)) is described in the Supplement. Estimating $[H_2SO_4]$ theoretically through the saturation vapor pressure in the temperature of T_{sa} provides some information on the dependency of $[H_2SO_4]$ on T_{sa} in the raw sample. However, the absolute concentrations cannot be satisfactorily estimated, firstly, because diffusional losses of H_2SO_4 onto the sampling lines between the H_2SO_4 evaporator and the PTD are high and uncertain, and secondly, because measuring H_2SO_4 is generally a challenging task due to high diffusional losses onto the walls of the sampling lines between the measurement point and the measurement device. High diffusional losses are caused by high diffusion coefficient of H_2SO_4. Additionally, a low flow rate from the H_2SO_4 evaporator (0.5 slpm) increases the diffusional losses before the measurement point. The diffusional losses before the measurement point, according to the equations reported by Gormley and Kennedy (1948) and to the humidity-dependent diffusion coefficient of H_2SO_4 reported by Hanson and Eisele (2000), are 98 % if the walls of the sampling lines are assumed fully condensing. However, some parts in the sampling lines have high concentrations of H_2SO_4 with high temperature, especially with high T_{sa} values. Therefore, these lines are probably partially saturated with H_2SO_4, which can act as preventing H_2SO_4 condensation onto the walls. Thus, the actual diffusional losses are estimated to be between 0 and 98 % and they can also depend on T_{sa} and on the saturation status of the sampling lines during a previous measurement point. In conclusion, the determination of $[H_2SO_4]$ in the raw sample was done through inverse modeling using measured particle diameter information (see Sec. 4.5). The output of the concentrations from inverse modeling denotes the diffusional losses of 43 ... 95 % depending on T_{sa}.

2.2 Raw exhaust sampling system

The sampling system used to dilute and cool the raw exhaust, presented in the bottom part of Fig. 1, was a modified partial flow sampling system (Ntziachristos et al., 2004) mimicking the dilution process occurring in a real-world driving situation. It consists of a PTD, an aging chamber, and an ejector diluter (ED). The PTD dilutes and cools the sample rapidly, which leads to new particle formation. The aging chamber is used to grow the newly-formed particles to detectable sizes and to continue the nucleation process. The ED is used to stop the particle formation and growth processes and to obtain the conditions of the sample required for measurement devices.

Dilution air used with the PTD and the ED was filtered compressed air. The ED used only dry ($RH \approx 3.6\,\%$) and unheated ($T \approx 20\,^\circ C$) dilution air, but the dilution air for the PTD was humidified ($RH_{PTD} = 2 ... 100\,\%$) and heated ($T_{PTD} = 27.5 ... 70\,^\circ C$). Humidifying the dilution air of the PTD was done by directing the compressed air flow through a container filled with deionized Milli-Q water. RH_{PTD} and T_{PTD} are the variable parameters used in examining the effect of $[H_2O]$ and T on J, which represent the conditions of the outdoor air acting in a dilution process in a real-world driving situation. The range of T_{PTD} represent higher temperatures compared to the temperature of the outdoor air, but lower temperatures were not used because 27.5 °C was the coldest temperature available with the laboratory setup having no cooling device.

In this experiment, the residence time in the aging chamber was made adjustable by a movable sampling probe inside the aging chamber. The sampling probe was connected to the ED with a flexible Tygon hose. The residence time from before the PTD to after the ED was altered within a range of 1.4 ... 2.8 s. Using a movable probe to alter the residence time has only a minor effect on the flow and temperature fields compared to altering the residence time with changing the flow rate in the aging chamber. Maintaining constant flow and temperature fields when studying the effect of the residence time is important, because variable fields would alter the turbulence level and temperatures in the aging chamber, both having effects on the measured particle concentration and thus causing difficulties to separate the effect of the residence time from the effect of turbulence or temperature on measured particle concentrations.

The DR of the PTD (DR_{PTD}) was controlled by the excess flow rate after the aging chamber and calculated by the measured $[CO_2]$ before the PTD and after the aging chamber. The DR_{PTD} was kept around 20 in all measurements. The DR of the ED (DR_{ED}) was controlled by the pressure of the dilution air used with the ED and calculated also using CO_2 measurements. The calculated DR_{ED} was around 10. Because the dilution ratios varied between different measurement points, all the aerosol results are multiplied with the total DR thus making the results comparable.

2.3 Particle measurement

Particle number concentration and size distribution was measured after the ED using Airmodus PSM A11 (Particle Size Magnifier A10 using Airmodus Condensation Particle Counter A20 as the particle counter), TSI CPC 3775 (Ultrafine Condensation Particle Counter), and TSI Nano-SMPS (Nano Scanning Mobility Particle Sizer using TSI CPC 3776 as the particle counter). The PSM and the CPC 3775 measure the particle number concentration (N_{PSM} and N_{CPC}) by counting particles with diameters larger than $\sim$ 1.15 nm (PSM) or $\sim$ 2.15 nm (CPC 3775). The D_{50}-cut-size (the particle diameter having the detection efficiency of 50 %) of the PSM can be altered, by adjusting its saturator flow rate, within the diameter range of 1.3 ... 3.1 nm. Additionally, the CPC 3775 has the D_{50}-cut-size of 4.0 nm and the CPC 3776 of ~~2.4~~ 3.4 nm. The detection efficiency curves of the particle ~~counter~~ counters used are presented in Fig. 2. The Nano-SMPS measured, with the settings used in this experiment, the particle size distribution within the diameter range of 2 ... 65 nm; however, the detection of particles having diameters smaller than $\sim$ ~~7~~ 6 nm are weakly detectable due to very low charging efficiency of the radioactive charger, low detection efficiency of the particle counter, and high diffusional losses ~~of very small particles~~ inside the device, for very small particles. Nevertheless, using the data from the different saturator flow rates of the PSM together with the data from the CPC 3775, information on the particle size distribution around the range of 1.15 ... ~~7~~ 6 nm is also obtained.

Due to too high particle number concentration for the PSM, aerosol measured with the PSM and the CPC 3775 was diluted with a bridge diluter (BD). It dilutes the concentration of larger particles ($D_p > 10\,nm$) with the ratio of 250, but the DR increases with decreasing particle size due to diffusional losses, finally to the ratio of 1200 ($D_p = 1.15\,nm$). The DR was measured with aerosol samples having the count median diameters (CMDs) of 2 ... 25 nm. The ratio of the sampling line length and the flow rate of the BD, a partially unknown variable, used in the diffusional losses function reported by Gormley and Kennedy (1948) was fitted to correspond with the DR measurement results; the obtained DRs are presented in Fig. 3.

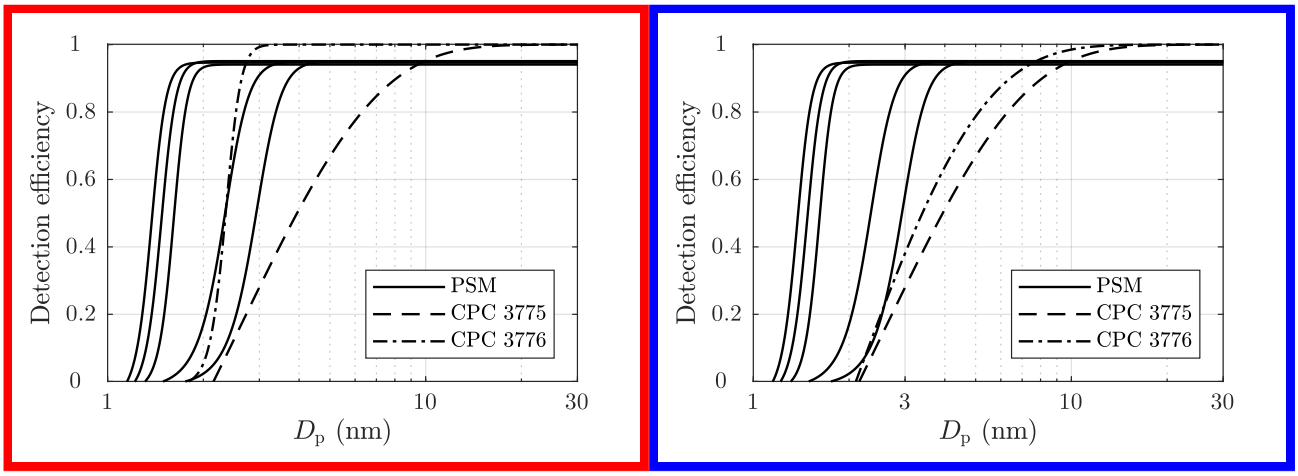

Figure 2. The detection efficiencies of the PSM, with five different saturator flow rates used in this experiment, and of the CPCs. The curves are exponential fittings based on the detection efficiencies reported by the manufacturers of the devices, excluding the CPC 3776 curve which is based on the efficiency measured by Mordas et al. (2008) .

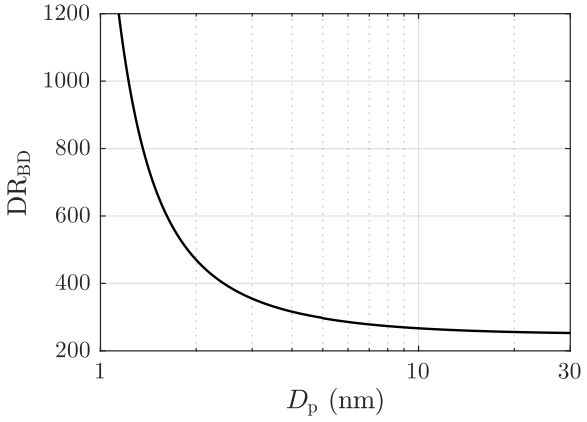

Figure 3. The dilution ratio of the bridge diluter with different particle diameters.

2.4 Measurement sets

By varying $[H_2SO_4]$ of the artificial raw exhaust sample and $[H_2O]$ and T of the dilution air separately and measuring the aerosol formed in the sampling system, the effects of the parameters on J can be examined. The effects of the parameters are included in Eq. (2) simply with the exponents n_{sa}, n_w, and m_{sa}. To obtain these three yet unknown values, at least three parameters were required to be varied in the experiments. Nevertheless, a fourth parameter, the residence time, was also varied to provide some validation for the obtained exponents. $[H_2O]$ and T of the dilution air were varied simply by humidifying and heating the dilution air flowing to the PTD and measuring RH and T from the dilution air. Varying $[H_2SO_4]$ of the raw sample was done by varying T_{sa}, and the values for $[H_2SO_4]$ in the raw sample were obtained through inverse modeling.

The varied conditions of the measurements are presented in Tab. 1, in which all the measurement points are divided according to the main outputs (n_{sa}, n_w, m_{sa}, and $\partial J/\partial t$) that measurement sets were designed to provide. Examining the effect of temperature (m_{sa}) was performed with the measurements of two types: varying T_{PTD} while keeping RH_{PTD} as a constant (Set 3a) and varying T_{PTD} while keeping the mole fraction of H_2O in the dilution air of the PTD ($x_{w,PTD}$) as a constant (Set 3b). The time-dependence of the nucleation rate ($\partial J/\partial t$) or, in the other words, the diminishment rate of J in a diluting sampling system is mainly the product of the exponents n_{sa} and m_{sa} in the following way: $[H_2SO_4]$ decreases steeply due to dilution, losses to walls, and condensation to particles resulting in diminishing J with the power of n_{sa}; simultaneously T decreases due to dilution and cooling of the sampling lines resulting in strengthening J with the power of m_{sa}. Examining the diminishment rate provides validation for the relation of n_{sa} and m_{sa} obtained from the simulations. We waited 2 ... 40 min for the particle size distributions to stabilize after the conditions was changed between the measurement points. When the particle formation process was satisfactorily stabilized, measurement data for each measurement point were recorded for 5 ... 40 min, depending on the stability of the particle generation.

Table 1. The varied conditions of the measurement points.

Set	Main output	T_{sa} (°C)	T_{PTD} (°C)	$x_{w,PTD}$ (10^{-3})	RH_{PTD} (%)	Residence time (s)
1	n_{sa}	85 ... 164.5	27.5	7.7	22	2.8
2	n_w	150	30	0.7 ... 42	2 ... 100	2.8
3a	m_{sa}	150	30 ... 70	9 ... 65	22	2.8
3b	m_{sa}	150	30 ... 70	44	22 ... 100	2.8
4	$\partial J/\partial t$	135.5 ... 164.5	27.5	7.7	22	1.4 ... 2.8

3 Experimental results

Figure 4 represents examples of particle size distributions measured with different H_2SO_4 evaporator temperatures, T_{sa}. The PSM+CPC data are calculated using the number concentrations measured with different saturator flow rates of the PSM and

with the CPC 3775, i.e. with different D_{50}-cut-sizes. To properly compare the data measured with different dilution ratios and sampling line lengths, the comparison requires backwards-corrected data, i.e., all data in the figure are corrected with the DR of the BD and with the diffusional losses caused by the sampling lines between the ED and the measurement devices. However, correcting the distributions backwards from the measured data to the distributions after the ED is not simple because that requires the shapes of the distributions within the whole diameter range to be known. The data of the PSM and the CPC 3775 cannot always provide real size distributions because the cumulative nature of the method using particle counters as the size distribution measurement can suffer from noise in measured concentration. For example, the PSM+CPC data with $T_{\mathrm{sa}} = 157.2\,^{\circ}\mathrm{C}$ shown in Fig. 4 implies that the concentration could increase with decreasing particle size, but the placing of the data points can be caused by the noise in the measured concentrations. On the other hand, the data implies that there are no particles smaller than $\sim$ 2.5 nm in diameter, but the data of the smaller particles can be invisible due to the noise in the measured concentrations (see the Supplement for the detailed error estimation of the size distributions). Hence, the unknown concentration of the particles smaller than $\sim$ 2.5 nm in diameter can have a significant effect on the total number concentration after the ED calculated from the measured data because these particles play the major role in the effect of the diffusional losses in the sampling lines and in the BD. Due to these uncertainties, the backwards-corrected data (denoting the distributions right after the ED) are not used when comparing the measured results with the simulated results later in this article. Nevertheless, the backwards-corrected data are used when presenting the distributions from all the aerosol devices together because the distributions cannot be presented without correcting them backwards due to different particle losses in the sampling lines of the different devices.

It can be observed that though the Nano-SMPS data are in a nearly log-normal form, there are also size distributions in the PSM+CPC diameter range. Particles generated with lower T_{sa} are lower in concentration and smaller than ones with higher T_{sa}; and higher ~~amount~~ fraction of particles are in the PSM+CPC diameter range. The smaller diameter edges of the log-normal size distributions measured by the Nano-SMPS do not connect with the distributions measured by the PSM and the CPC 3775 due to ~~high diffusional losses of very small particles inside the~~ the weak detection efficiency of very small particles by the Nano-SMPS~~device, due to low charging efficiency of small particles, and due to the inversion algorithm of the device which favors features from a log-normal size distribution~~. Thus, the smaller diameter edges of the measured log-normal size distributions are not accurate. Similar disagreements of the data from these devices have been observed elsewhere also both in exhaust-related (Alanen et al., 2015; Rönkkö et al., 2017) and in atmospherically-related studies (Kulmala et al., 2013). By examining the combination of the size distributions measured by the PSM and the CPC 3775 and the size distributions measured by the Nano-SMPS, the real size distributions are not in a log-normal form. The detailed error estimation of the measured distributions and discussion on this disagreement can be found in the Supplement.

The particle number concentrations measured with the highest saturator flow rate of the PSM (N_{PSM}), i.e. the particles with diameters larger than $\sim$ 1.3 nm, and the diameters with the average mass ($D_{\bar{m}}$) of the measurement set 1 are presented in Fig. 5. $D_{\bar{m}}$ are calculated using the size distributions measured with the combination of the PSM, the CPC 3775, and the Nano-SMPS which are corrected with the diffusional losses in the sampling lines. The figure consists of data measured at two different days. It can be observed that N_{PSM} increases steeply with increasing $[\mathrm{H_2SO_4}]_{\mathrm{raw}}$ with lower $[\mathrm{H_2SO_4}]_{\mathrm{raw}}$ values, but the steepness

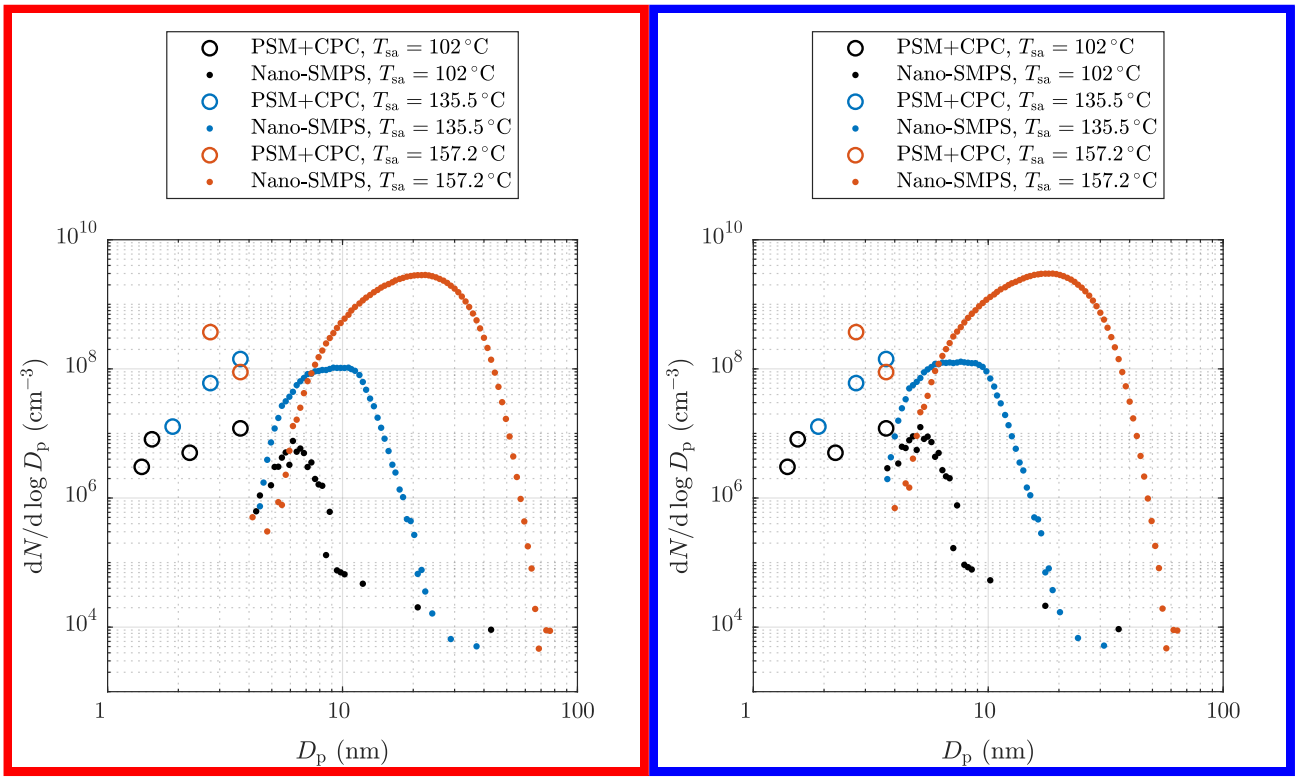

Figure 4. Examples of particle size distributions after the ED measured with different H_2SO_4 evaporator temperatures in the measurement set 1. The data are corrected with the DR of the BD and with the diffusional losses in the sampling lines after the ED. The concentrations are multiplied with the total DR of the sampling system. See the Supplement for error bars.

decreases with increasing $[H_2SO_4]_{raw}$ due to increasing self-coagulation rate. With lower $[H_2SO_4]_{raw}$ values the slope of N_{PSM} versus $[H_2SO_4]_{raw}$ in a log-log scale,

$$n_{N_{PSM}\text{ vs. }[H_2SO_4]_{raw}} = \frac{\partial \ln N_{PSM}}{\partial \ln [H_2SO_4]_{raw}}, \tag{3}$$

is approximately 10, but decreases to approximately 0.4 with decreasing $[H_2SO_4]_{raw}$. The slope of J versus $[H_2SO_4]$ is, by the definition of J (Eq. (2)),

$$n_{J\text{ vs. }[H_2SO_4]} = \frac{\partial \ln J}{\partial \ln [H_2SO_4]} = n_{sa}, \tag{4}$$

which is also the nucleation exponent for $[H_2SO_4]$. The slope $n_{N_{PSM}\text{ vs. }[H_2SO_4]_{raw}}$ can provide a rough estimate of the slope n_{sa} but due to the other aerosol processes, especially coagulation, having effects on the particle concentrations, the estimated slope can differ a lot from the real n_{sa} in the nucleation rate function. The slope at higher $[H_2SO_4]_{raw}$ values is usually decreased due to coagulation and the slope at lower $[H_2SO_4]_{raw}$ values can be increased due to decreased particle detection efficiency of smaller particles. Therefore, n_{sa} is expected to be within the range of 0.4 ... 10. Additionally, the estimated slope can also

differ from n_{sa} because $n_{N_{\mathrm{PSM}}\,\mathrm{vs.}\,[\mathrm{H_2SO_4}]_{\mathrm{raw}}}$ is based on $[\mathrm{H_2SO_4}]$ in the raw sample rather than the value of $[\mathrm{H_2SO_4}]$ in a specific location: $[\mathrm{H_2SO_4}]$ decreases from the concentration in the raw sample several orders of magnitude during the dilution process.

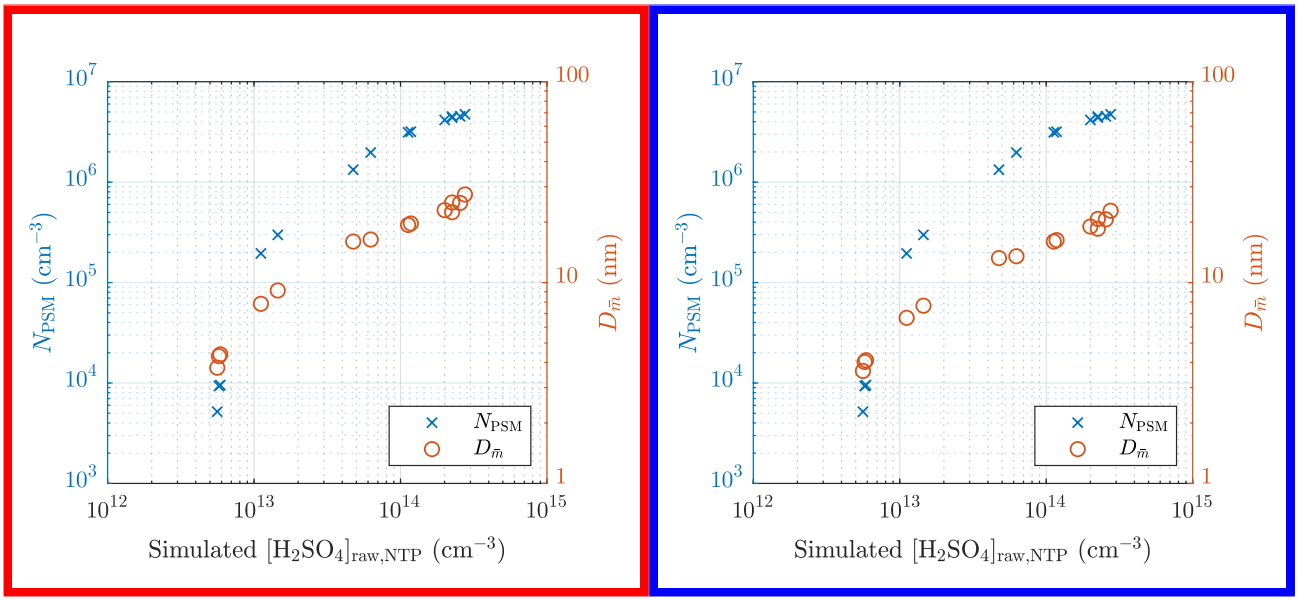

Figure 5. The measured number concentrations of the particles larger than $\sim$ 1.3 nm and the diameters with the average mass of the measurement set 1 as a function of the simulated $\mathrm{H_2SO_4}$ concentration in the raw sample. The concentrations are multiplied with the total DR of the sampling system. The error bars for these values are shown later in Fig. 13.

The effect of humidity on the particle concentration (Set 2) is shown in Fig. 6. The slope of N_{PSM} versus $\mathrm{RH_{PTD}}$ in a log-log scale,

$$n_{N_{\mathrm{PSM}}\,\mathrm{vs.}\,\mathrm{RH_{PTD}}} = \frac{\partial \ln N_{\mathrm{PSM}}}{\partial \ln \mathrm{RH_{PTD}}}, \tag{5}$$

is roughly between 0.1 and 0.2. The slope $n_{N_{\mathrm{PSM}}\,\mathrm{vs.}\,\mathrm{RH_{PTD}}}$ nearly equals the slope of N_{PSM} versus $[\mathrm{H_2O}]_{\mathrm{PTD}}$ ($n_{N_{\mathrm{PSM}}\,\mathrm{vs.}\,[\mathrm{H_2O}]_{\mathrm{PTD}}}$) because T_{PTD} is nearly a constant. The slope $n_{N_{\mathrm{PSM}}\,\mathrm{vs.}\,[\mathrm{H_2O}]_{\mathrm{PTD}}}$ corresponds to the slope n_{w} with the same uncertainties as involved with the slopes $n_{N_{\mathrm{PSM}}\,\mathrm{vs.}\,[\mathrm{H_2SO_4}]_{\mathrm{raw}}}$ and n_{sa}. Nevertheless, the effect of decreased particle detection is not involved because, in this case, particle size has only a weak dependency of $\mathrm{RH_{PTD}}$. Additional uncertainty in estimating n_{w} arises from the origin of $\mathrm{H_2O}$ vapor in the system, which is both the dilution air and the raw sample. Because $[\mathrm{H_2O}]$ in the raw sample was kept constant, it has a higher effect on the total $[\mathrm{H_2O}]$ with lower values of $\mathrm{RH_{PTD}}$; thus, the estimated n_{w} is lower than the real n_{w} in the nucleation rate function.

The effect of T_{PTD} can be observed in Figs. 6 and 7. Lower temperatures result in higher concentrations of N_{PSM}. However, the examination is problematic because keeping $\mathrm{RH_{PTD}}$ as a constant while increasing T_{PTD} (Set 3a) increases $[\mathrm{H_2O}]$, which results in lower N_{PSM} with lower temperatures. Therefore, keeping $x_{\mathrm{w,PTD}}$ as a constant (Set 3b) is better in examining m_{sa}.

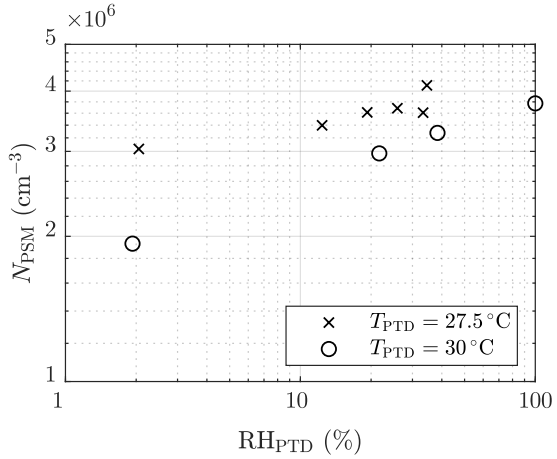

Figure 6. The measured number concentrations of the particles larger than $\sim$ 1.3 nm of the measurement set 2 as a function of the RH of the PTD dilution air. The concentrations are multiplied with the total DR of the sampling system. The error bars are within the marker sizes.

One of the measurements with $T_{\mathrm{PTD}} = 50\,^{\circ}\mathrm{C}$ is, however, a significant outlier in Set 3b. Estimating the exponent m_{sa} from the slope in Fig. 7 is not straightforward because temperature is included also in the concentrations having yet unknown exponents.

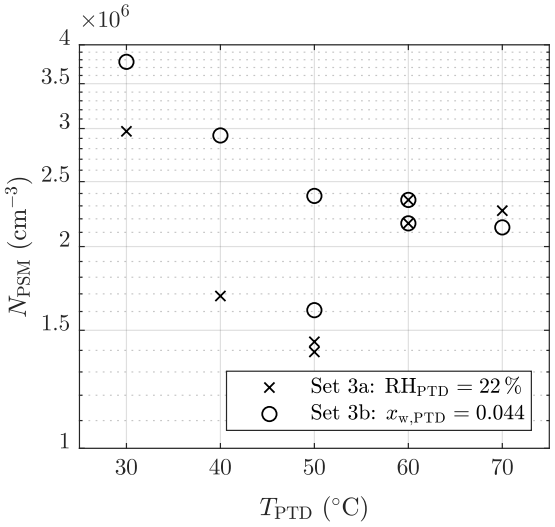

Figure 7. The measured number concentrations of the particles larger than $\sim$ 1.3 nm of the measurement set 3 as a function of the T of the PTD dilution air. The concentrations are multiplied with the total DR of the sampling system. The error bars are within the marker sizes.

The effect of the residence time on the particle concentrations is presented in Tab. 2. With $T_{\mathrm{sa}} = 135.5\,^{\circ}\mathrm{C}$ the ratio of N with the residence times of 1.4 s and with the residence time of 2.8 s is below unity, but above unity with higher temperatures. The

ratio below unity denotes that the nucleation process is not diminished yet at the time of 1.4 s, e.g., the ratio of 0.74 denoting 74% of particles are formed within the time range of 0 ... 1.4 s and the remaining 26% within the time range of 1.4 ... 2.8 s. With higher temperatures the ratio is above unity because self-coagulation begins to decrease the number concentration, especially at the later times where the number concentration is the highest. The nucleation process may continue after 1.4 s but it cannot be easily seen with higher temperatures. Because coagulation has no effect on the mass concentrations (M), the ratios of M measured with the combination of the PSM, the CPC 3775, and the Nano-SMPS with the residence time of 1.4 s and with the residence time of 2.8 s are near unity with higher temperatures. The effect of particle growth and wall losses, however, have effects on the ratios too. The temperature with which the coagulation process would eliminate the effect of the nucleation process, resulting in the number concentration ratio of unity, is near 142 °C.

Table 2. The ratios of the measured number concentrations and mass concentrations with the residence times of 1.4 s and 2.8 s, in the measurement set 4. The values are corrected with the DR of the BD and with the diffusional losses in the sampling lines after the ED; thus, the values correspond with the distributions existing after the ED.

T_{sa} (°C)	$\frac{N(1.4\mathrm{s})}{N(2.8\mathrm{s})}$	$\frac{M(1.4\mathrm{s})}{M(2.8\mathrm{s})}$
135.5	0.74	0.28
150	1.29	0.92
160	1.72	0.96
164.5	1.74	1.10

4 Simulations

Every measurement point presented in Tab. 1 was simulated with the model consisting of four phases: (1) the CFD simulations to solve the flow and the temperature field of the sampling system, (2) the CFD-TUTMAM simulations to solve the aerosol processes in the sampling system, (3) correcting the particle sizes decreasing rapidly in the dry ED, and (4) calculating the penetration of the particles due to diffusional losses in the sampling lines after the sampling system and the detection efficiencies of the particle counting devices.

4.1 CFD model

The CFD simulations to solve the flow and the temperature fields for every simulation case were performed with a commercially available software ANSYS FLUENT 17.2. It is based on a finite volume method in which the computational domain is divided into a finite amount of cells. Governing equations of the flow are solved in every computational cell iteratively until sufficient convergence is reached. In this study, the governing equations in the first phase are continuity, momentum, energy, radiation, and turbulence transport equations.

The computational domain in the CFD simulations is an axial symmetric geometry consisting of the PTD, the aging chamber, and the ED (Fig. 1). An axial symmetric geometry was selected over a three-dimensional geometry due to high computational demand of the model and a nearly axial symmetric profile of the real measurement setup. The domain was divided into $\sim 8 \times 10^5$ computational cells, of which the major part was located inside the PTD where the smallest cells are needed due to the highest gradients. The smallest cells were 20 μm in side lengths and were located in the beginning of the porous section, where the hot exhaust and the cold dilution air meet.

In contrast to our previous study (Olin et al., 2015), the ED was also included in the computational domain though the ED has only a minor effect on nucleation (Lyyränen et al., 2004; Giechaskiel et al., 2009). Because the ED has a high speed nozzle that cools the flow locally to near -30 °C, including it in the domain provides partial validation for m_{sa} in the following way: if too high value for m_{sa} were used, nucleation would be observed in the ED, being in contradiction with the former studies. The internal fluid inside the sampling lines is modeled as a mixture of air, H_2O vapor, and H_2SO_4 vapor. The sampling lines are modeled as solid zones of steel or Tygon. 10 cm of the external fluid, modeled as air, is also included in the domain to simulate natural cooling of the sampling lines.

Flow rate and temperature boundary conditions for the simulated sampling system were set for the each simulation case to the measured values. Due to steady-state conditions and high computational demand, all governing equations were time-averaged; thus, the simulations were performed with a steady-state type. Turbulence was modeled using the SST-k-ω model, which is one of the turbulence models used with a steady-state simulation. It produced the most reliable results of the available steady-state turbulence models based on the pressure drop in the porous section. Turbulence, however, can have a significant role in the wall losses of the vapors and the particles in the regions where the turbulence level is high. In this sampling system, the turbulence level is high in the upstream part of the aging chamber where the diameter of the sampling line increases steeply. Validating the suitability of the turbulence model for this geometry would require a measurement of, e.g., solid seed particle concentrations after and before the sampling system without any aerosol processes, such as nucleation, condensation, and coagulation. However, that kind of measurement has not been performed yet.

4.2 CFD-TUTMAM

The main functionality of the CFD-TUTMAM based on the previous aerosol model, CFD-TUTEAM, is described by Olin et al. (2015). However, because the measured distributions are not in a log-normal form, the inclusion of the PL+LN model (Olin et al., 2016) was beneficial. The PL+LN model simulates the initial growth of newly-formed very small particles by modeling the particle size distribution with the combination of a power law (PL) and a log-normal (LN) distribution. Newly-formed particles are first put to the PL distribution, after which they are transferred to the LN distribution by particle growth.

The CFD-TUTMAM adds three governing equations per a distribution (denoted by j) to the CFD model using a modal representation of the particle size distribution, i.e. the distributions are modeled by three variables: number ($M_{j,0} = N_j$), surface area-related ($M_{j,2/3}$), and mass ($M_{j,1}$) moment concentrations. $M_{j,1}$ are further divided into different components in a multi-component system. Due to small particle size and low particle loading, the aerosol phase has only a minor effect on the gas phase properties. Therefore, continuity, momentum, energy, radiation, and turbulence transport equations can be excluded

from the computation after the flow and temperature fields are solved, and only gas species equations and the aerosol model equations are solved. The governing equation of the aerosol model for the concentration of a kth moment of a distribution j is

$$\frac{\partial M_{j,k}}{\partial t} = -\nabla\cdot(M_{j,k}\boldsymbol{u}) + \nabla\cdot\left(\rho_{\mathrm{f}}\overline{D}_{j,k,\mathrm{eff}}\nabla\frac{M_{j,k}}{\rho_{\mathrm{f}}}\right) + \mathrm{nucl}_{j,k} + \mathrm{cond}_{j,k} + \mathrm{coag}_{j,k} + \mathrm{transfer}_{j,k}, \tag{6}$$

where $\boldsymbol{u}$, ρ_{f}, and $\overline{D}_{j,k,\mathrm{eff}}$ are the fluid velocity vector, the fluid density, and the kth moment-weighted average of the particle effective diffusion coefficient, respectively. The last terms in Eq. (6) represent source terms for nucleation, condensation, coagulation, and intermodal particle transfer. In this study, aerosol is modeled with two distributions: a PL distribution ($j = \mathrm{PL}$) and a LN distribution ($j = \mathrm{LN}$). In this study, two gas species equations, which model the internal fluid mixture as the mass fractions of H_2O and H_2SO_4, are built in the CFD model, but the opposite numbers of the source terms of nucleation and condensation are added to them to maintain the mass closure of the species.

After each iteration step of the CFD-TUTMAM simulation, the parameters of the distributions are calculated for every computational cell by using the three moment concentrations. The parameters for the PL distribution are the number concentration (N_{PL}), the slope parameter (α), and the largest diameter (D_2). The smallest diameter (D_1) has a fixed value of 1.15 nm which is the smallest detectable particle diameter with the devices used. The density function for the PL distribution is

$$\left.\frac{\mathrm{d}N}{\mathrm{d}\ln D_{\mathrm{p}}}\right|_{\mathrm{PL}} = \begin{cases} N_{\mathrm{PL}}\left(\frac{D_{\mathrm{p}}}{D_2}\right)^{\alpha}\beta_0, & D_1 \le D_{\mathrm{p}} \le D_2 \\ 0, & \text{otherwise} \end{cases}, \tag{7}$$

where β_0 is a function

$$\beta_l\left(\alpha, \frac{D_1}{D_2}\right) = \begin{cases} \frac{\alpha+l}{1-\left(\frac{D_1}{D_2}\right)^{\alpha+l}}, & \alpha \neq -l \\ \frac{1}{-\ln\left(\frac{D_1}{D_2}\right)}, & \alpha = -l \end{cases}. \tag{8}$$

The parameters for the LN distribution are the number concentration (N_{LN}), the geometric standard deviation (σ), and the geometric mean diameter (D_{g}). An analytical solution exists for the reconstruction of the parameters from the moment concentrations for the LN distribution but not for the PL distribution; thus, it is solved numerically. A numerical solution is obtained by using the Levenberg-Marquardt iteration algorithm, in contrast to a slower method using a pre-calculated interpolation table described by Olin et al. (2016).

The nucleation source terms in Eq. (6) for different moments are

$$\begin{aligned} \mathrm{nucl}_{\mathrm{PL},0} &= J \\ \mathrm{nucl}_{\mathrm{PL},2/3} &= J\left(m^*_{\mathrm{sa}} + m^*_{\mathrm{w}}\right)^{2/3} \\ \mathrm{nucl}_{\mathrm{PL},1,\mathrm{sa}} &= J m^*_{\mathrm{sa}} \\ \mathrm{nucl}_{\mathrm{PL},1,\mathrm{w}} &= J m^*_{\mathrm{w}} \\ \mathrm{nucl}_{\mathrm{LN},k} &= 0, \end{aligned} \tag{9}$$

where J is the nucleation rate as in Eq. (2) and m_{sa}^* and m_{w}^* are the masses of H_2SO_4 and H_2O in a newly-formed particle. The value of $D_1 = 1.15\,\mathrm{nm}$ was chosen for the diameter of the newly-formed particles. A particle of this diameter is in equilibrium with water uptake in the temperature of 300 K and in the relative humidity of 22 % if the mass fraction of H_2SO_4 in the particle is 0.71. This constant value is used with nucleation though the mass fraction would vary between 0.5 and 1 if the whole temperature and humidity range were considered, but the major part of nucleation occurs in the conditions having the equilibrium mass fraction of near 0.71. This mass fraction and particle diameter corresponds to a cluster containing 5.7 H_2SO_4 molecules and 12.4 H_2O molecules.

Diffusion, condensation, and coagulation are modeled as described in the reference Olin et al. (2015) and intermodal particle transfer as described in the reference Olin et al. (2016). Condensation is modeled with the growth by H_2SO_4 from which immediately follows the water uptake until the water equilibrium is achieved. The water equilibrium procedure is also described in the reference Olin et al. (2015). The coagulation modeling includes intramodal coagulation within the both distribution and intermodal coagulation between the distributions.

Intermodal particle transfer includes condensational transfer and coagulational transfer from the PL distribution to the LN distribution. In contrast to a constant condensational transfer factor γ of the PL+LN model described in the reference Olin et al. (2016), a function of α, D_1/D_2, and k is used in the CFD-TUTMAM due to a more complex particle growth modeling. The function used here is

$$\gamma\left(\alpha, \frac{D_1}{D_2}, k\right) = \begin{cases} 0.1\alpha + 0.5, & \alpha \geq 0 \\ 0, & \alpha < 0 \end{cases} \times \begin{cases} \frac{3}{\beta_0}, & k = 0 \\ \frac{2}{\beta_1} + \frac{1}{\beta_2}, & k = \frac{2}{3} \\ \frac{3}{\beta_2}, & k = 1 \end{cases} . \tag{10}$$

The functional form of γ is derived so that the condensational transfer eliminates the effect of increasing α by the condensation process and also tries to keep α positive because a PL distribution with a negative α in combination with a LN distribution represents a distribution having a nonphysical local minimum between the distributions. The form of γ also restricts α increasing too high, which would cause numerical difficulties. Particles are not lost or altered during the intermodal particle transfer, it is only controlling the ratio of particles represented in the PL distribution and in the LN distribution. Higher values of γ result in lower N_{PL}/N ratio.

Deposition of particles and condensation of vapors onto the inner walls of the sampling lines have direct effect on the aerosol concentrations at the measurement devices. The particle deposition was modeled by setting the boundary conditions for the aerosol concentrations at the walls to zero, which represents deposition driven by diffusion and turbulence. Condensation of H_2O and H_2SO_4 vapors onto the walls was modeled by setting the boundary conditions for the mass fractions of H_2O and H_2SO_4 at the walls to saturation mass fractions in an aqueous solution of H_2SO_4, in contrast to the simpler method in the previous study (Olin et al., 2015). The simpler method caused H_2SO_4 to be completely non-condensing onto the walls

because the saturation ratio of the pure vapor never exceeded unity. Instead, the method using the saturation mass fractions in the solution induces some condensation because the vapor pressure of a hygroscopic liquid over an aqueous solution is lower than over a pure liquid. This method provides also smoother behavior of the boundary conditions on the walls. The method is, however, strongly dependent of the chosen activity coefficient functions of the vapors, which have large differences between each other due to their exponential nature. Activity coefficients used here are based on the values reported by Zeleznik (1991). However, due to exponential and non-monotonic nature of activity coefficients, they cause numerical difficulties in CFD modeling; thus, a monotonic van Laar type equation fitted by Taleb et al. (1996) from the data of Zeleznik (1991) was used.

4.3 Dry particle model

The main trend of the RH inside the sampling system is increasing due to decreasing temperature. This results in increasing water uptake rate during the particle growth process, which can be modeled by the condensation rate of H_2O that is simply the condensation rate of H_2SO_4 multiplied with a suitable factor (the water equilibrium procedure described by Olin et al. (2015)). However, when the sample enters to the ED, the RH decreases rapidly due to a dry dilution air, but the growth process by the condensation of H_2SO_4 still continues. This results in increasing H_2SO_4 amount in the particles but rapidly decreasing H_2O amount, which cannot be modeled with the water uptake model. Hence, the particles after the ED simulated by the CFD-TUTMAM contain incorrectly too much water.

All the simulated particle size distributions output by the CFD-TUTMAM were corrected to correspond the water amount that would be in the conditions after the ED ($T \approx 23\,^{\circ}\mathrm{C}$ and RH $\approx 3.6\,\%$). These conditions are mainly caused by the conditions of compressed air directed to the ED. Additionally, the particle size measurement device (Nano-SMPS) used room air, having nearly equal conditions as compressed air, as the sheath flow air. Dry sheath flow air also dries particles rapidly inside the device. The theory behind the dry particle model equals the theory behind the water uptake model in the CFD-TUTMAM, but the drying process is significantly faster and in opposite direction, in contrast to the water uptake connected to the condensation rate of H_2SO_4 in the CFD-TUTMAM. Figure 8 represents examples of particle diameters in different humidities, e.g., a particle with the diameter of 40 nm in the RH of 60 % shrinks to the diameter of 30 nm when sampled with the ED.

4.4 Penetration and detection efficiency model

Particle size distributions output by the CFD-TUTMAM and corrected with the dry particle model were also corrected according to the penetration and detection efficiency model. Particle penetration in the sampling lines between the ED and the measurement devices were calculated with the equations of Gormley and Kennedy (1948). All the internal diameters of the used sampling lines were sufficiently large to keep the flows laminar to minimize the diffusional losses. The penetration-corrected size distributions were multiplied with the detection efficiency curves presented in Fig. 2 to simulate the measured number concentrations by the PSM and the CPC 3775 and the measured size distribution by the Nano-SMPS.

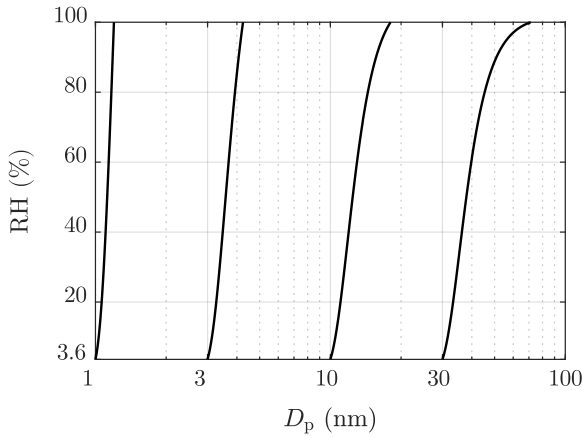

Figure 8. Examples of particle diameters in different humidities in the temperature of 23 °C. The lowest RH value represents the RH of the dilution air of the ED.

4.5 Inverse modeling

The simulated number concentrations measurable by the PSM with different saturator flow rates and by the CPC 3775 and the simulated size distributions measurable by the Nano-SMPS were compared with the measured ones during inverse modeling. The exponents n_{sa}, n_{w}, and m_{sa} were altered until the simulated and the measured variables corresponded satisfactorily in all simulated cases. The proportionality coefficient k in Eq. (2) is unknown and depends on the exponents. Because the value of k affects directly on the nucleation rate magnitude, it was obtained by fitting until the simulated and the measured number concentrations corresponded.

Due to the uncertainties involved in the measurement of $[\mathrm{H_2SO_4}]_{\mathrm{raw}}$ (see the Supplement), the boundary conditions for $[\mathrm{H_2SO_4}]$ in the CFD-TUTMAM simulations could not be set initially. Hence, $[\mathrm{H_2SO_4}]_{\mathrm{raw}}$ was considered a fitting parameter also. It was estimated by comparing the aerosol mass concentrations because it has a direct effect on the particle sizes, but affects also on J. Inverse modeling of the vapor concentrations is possible due to the condensational growth of particles. In conclusion, the inverse modeling requires fitting all the five parameters (n_{sa}, n_{w}, m_{sa}, k, and $[\mathrm{H_2SO_4}]_{\mathrm{raw}}$) to obtain the function for J. The first four parameters were fitted in a way they have the same value for every simulation case, but the last parameter, $[\mathrm{H_2SO_4}]_{\mathrm{raw}}$, was fitted in every simulation case separately. In the simulations related to the measurement sets 2 ... 4, T_{sa} was not altered between the measurement points; therefore, the value of $[\mathrm{H_2SO_4}]_{\mathrm{raw}}$ in the simulations was constant. Because only one parameter was fitted separately, only one of the outputs, the aerosol number or mass concentration, could correspond with the measured value exactly. In this study, the number concentration was chosen as the main output of which correspondence is preferred over the correspondence of the mass concentration because nucleation process is connected more straightly to the number concentration.

The uncertainties involved in modeling turbulence and the condensation of the vapors onto the walls affect the number and mass concentrations in the measurement devices. Nevertheless, these uncertainties become partially insignificant because k and $[H_2SO_4]_{raw}$ are considered fitting parameters, which partially neglect uncertainly modeled losses of particles and vapors.

5 Simulation results

In this section, the outputs of the simulations performed using the nucleation rate function with the best correspondence between the measured and the simulated data are described firstly. Finally, the used nucleation rate function is presented.

5.1 Sulfuric acid concentrations

Figure 9 represents the comparison of the inversely modeled $[H_2SO_4]_{raw}$ with the theoretical concentrations. The simulated concentrations vary between 0.05 and 0.57 times the theoretical concentrations where the lowest values are observed with lower T_{sa} values probably due to the effect of increasingly saturating H_2SO_4 liquid onto the sampling lines with higher temperatures that can decrease the diffusional losses onto the sampling lines. All values lie between the theoretical level assuming full diffusional losses and the lossless theoretical level. A weak agreement of the simulated concentrations with 0.15 times the theoretical curve can be seen, which implies the diffusional losses of 85 % onto the sampling lines between the H_2SO_4 evaporator and the PTD. Results and involved challenges of the additional $[H_2SO_4]_{raw}$ measurements are presented in the Supplement.

5.2 Particle size distributions

Examples of measured and simulated particle concentrations and size distributions of the measurement set 1 are presented in Fig. 10. The panes (a) and (c) in the figure represent the concentrations measured/measurable with the PSM and the CPC 3775. Because the concentrations decrease with increasing cut diameter in the case with $T_{sa} = 102\,°C$ (a), particle size distribution exists within this diameter range, which is also seen in the simulated data. However, the concentration measured with the cut diameter of 3.1 nm is two-fold compared to the simulated one, implying that the real distribution is not a pure PL+LN distribution or the shape of the distribution is modeled incorrectly near the diameter of 3.1 nm. Conversely, in the case with $T_{sa} = 157.2\,°C$ (c), the concentrations are in the same level, which implies no size distribution within that diameter range.

The panes (b) and (d) in Fig. 10 represent examples of measured and simulated Nano-SMPS data. The case with $T_{sa} = 102\,°C$, (b) represent an example of one of the worst agreements of measured and simulated size distributions. While the simulated total number concentration agrees with the measured one in that case, the particle diameter is underestimated with the factor of $\sim$ ~~2.~~ 1.6. The disagreement is discussed later in this section. Conversely, in the case with $T_{sa} = 157.2\,°C$ (d), the distributions agree well, except that the model predicts higher particle concentration in the diameter range of ~~2~~ 2.5 ...~~10~~ 7 nm. This disagreement can be due to ~~the decreased~~ lower particle detection efficiency of the Nano-SMPS ~~with very small particles due to very high diffusional losses inside the device . These diffusional losses are~~ than is included in the inversion algorithm of the device (see the Supplement). This is not included in the penetration and detection efficiency model and ~~are~~ is

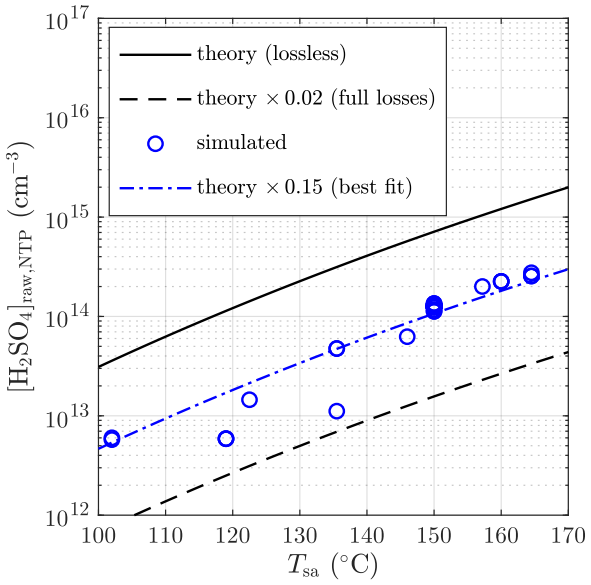

Figure 9. Simulated sulfuric acid concentrations in the raw sample compared to the theoretical concentrations with different sulfuric acid evaporator temperatures. The concentrations are presented as the concentrations in NTP conditions rather than in a hot raw sample.

thus not seen in the simulated distributions. Because the detection efficiency curve of the CPC 3776 is included in the model, the simulated size distributions measurable with the Nano-SMPS decrease steeply with decreasing particle diameter near the particle diameter of ~~$D_{50} = 2.4\,\mathrm{nm}$~~ $D_{50} = 3.4\,\mathrm{nm}$. The sharp peak at the diameter of $\sim$ 20 nm in the simulated distribution in (d) is caused by the nature of the PL+LN model where the PL distribution ends at the diameter of $D_2 \approx 20\,\mathrm{nm}$. While Fig. 10 represents the data at the measurement devices, Fig. 11 represents the example distributions after the ED. From the latter figure the PL distribution is seen as a whole, starting from the diameter of $D_1 = 1.15\,\mathrm{nm}$.

The requirement of the PL+LN model can be observed from Fig. 12, in which the particle number concentrations and sizes of a single simulation case with different values of $[H_2SO_4]_{raw}$ are presented. With low values of $[H_2SO_4]_{raw}$, both N and $D_{\bar{m}}$ behave discontinuously if only the LN distribution is simulated: particles are first small and in low concentration when $[H_2SO_4]_{raw}$ increases, and then suddenly rise to higher levels. This is, however, not seen with the PL+LN model, which has a smoother behavior. Therefore, by simulating with the LN distribution only, it is impossible to produce, e.g., a size distribution with $N = 10^4\,\mathrm{cm}^{-3}$ or $D_{\bar{m}} = 3\,\mathrm{nm}$ with this simulation setup, whereas with the PL+LN model it is possible.

5.3 Particle concentrations and sizes

Figure 13 represents the comparison of the simulated and the measured N_{PSM} and $D_{\bar{m}}$ values after the ED. The ~~blue crosses~~ black dots in the pane (a) correspond well with the measured concentrations because they represent the cases for which N_{PSM}

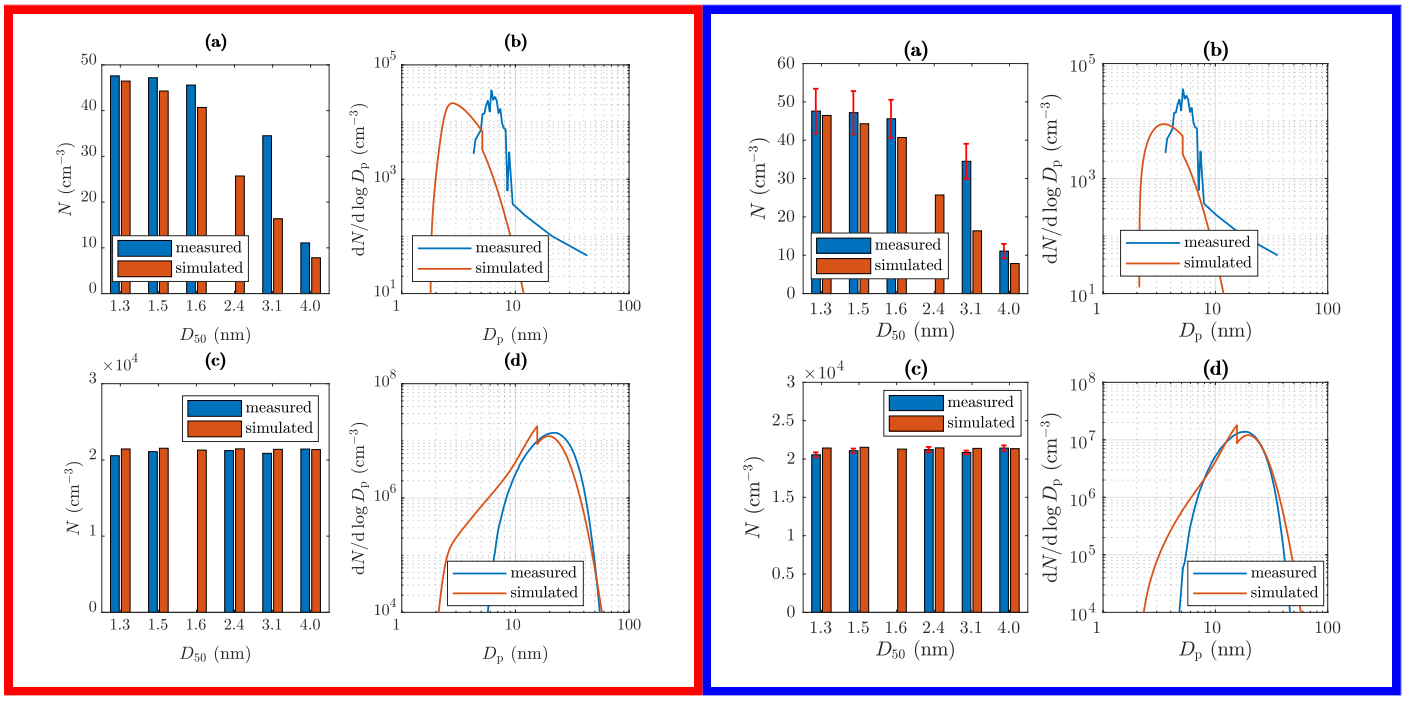

Figure 10. Examples of measured and simulated (a) number concentrations from the PSM and the CPC 3775 with $T_{sa} = 102\,°C$, (b) size distributions from the Nano-SMPS with $T_{sa} = 102\,°C$, (c) number concentrations from the PSM and the CPC 3775 with $T_{sa} = 157.2\,°C$, and (d) size distributions from the Nano-SMPS with $T_{sa} = 157.2\,°C$. The D_{50} values in the range of $1.3 \ldots 3.1$ nm represent the cut-sizes of the PSM with different saturator flow rates and the D_{50} value of 4.0 nm represents the cut-size of the CPC 3775. The error bars in the measured concentrations represent the standard deviations and are caused by instability in the particle generation.

was obtained by fitting the value of $[H_2SO_4]_{raw}$. The ~~black crosses have more deviations~~ red dots deviate more from the 1:1 line because they represent all the other cases, the N_{PSM} values of which originate from the simulations, e.g., simulated with different RH_{PTD}, T_{PTD}, or residence times. Nevertheless, all the simulated N_{PSM} values correspond with the measured values relatively well. The optimal scenario would be that all the N_{PSM} values would correspond exactly with the measured values, but that would imply the exponents n_w and m_{sa} in the nucleation rate function can be modeled exactly with constant values within the concentration and temperature ranges of this study. However, it is not expected that the constant exponents would represent exactly the nucleation rate function in all concentration and temperature ranges.

The ~~blue crosses~~ black dots in the pane (~~a~~b) of Fig. 13 correspond moderately with the measured $D_{\bar{m}}$ values. It can be observed that ~~with lower and higher values of $D_{\bar{m}}$ the model underestimates the~~ the points do not lie on a straight 1:1 line perfectly, instead they form a slightly curved line, on which simulated particle sizes are overestimated near 10 nm but underestimated in small particle sizes. There are several issues which can cause this discrepancy: (1) the exponent n_{sa} varies with $[H_2SO_4]$, (2) a problem in calculating $D_{\bar{m}}$ from the measurement data, (3) a problem in estimating a proper N_{PL}/N ratio in the PL+LN model, and (4) an uncertainty in simulating the condensation process. The most possible explanation is (1) be-

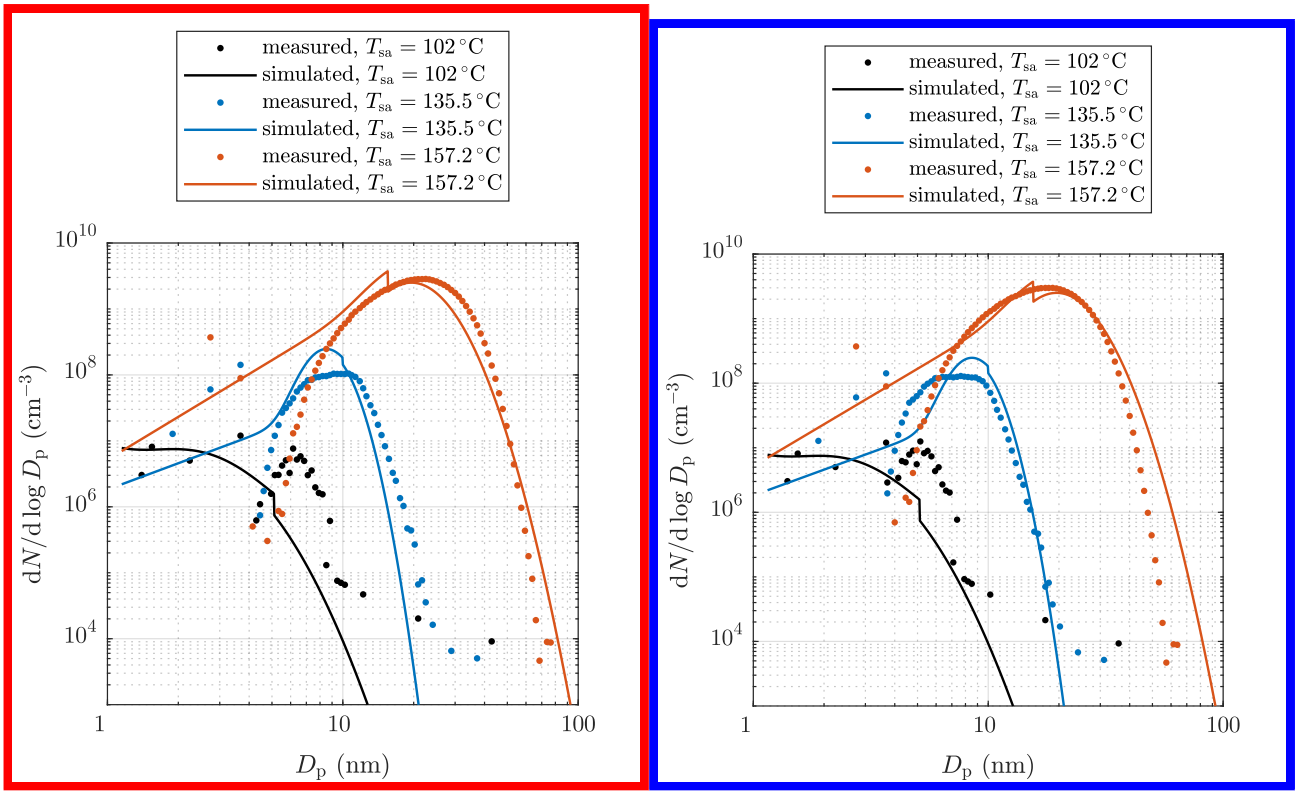

Figure 11. Examples of measured and simulated particle size distributions after the ED. The measured data are corrected with the DR of the BD and with the diffusional losses in the sampling lines after the ED. Additionally, all concentrations are multiplied with the total DR of the diluting sampling system. See the Supplement for error bars.

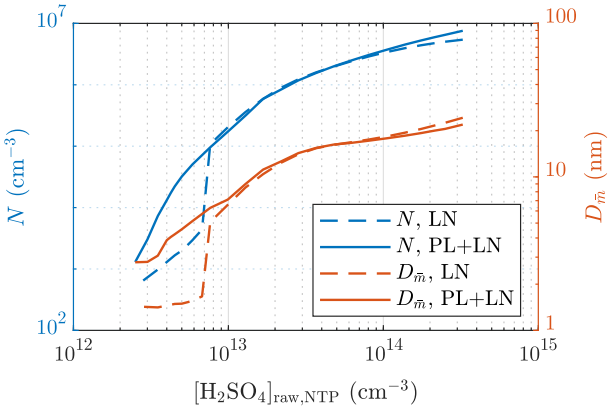

Figure 12. Comparison of the particle number concentrations and the diameters with the average mass after the ED simulated using the LN distribution only and using both the PL and the LN distributions.

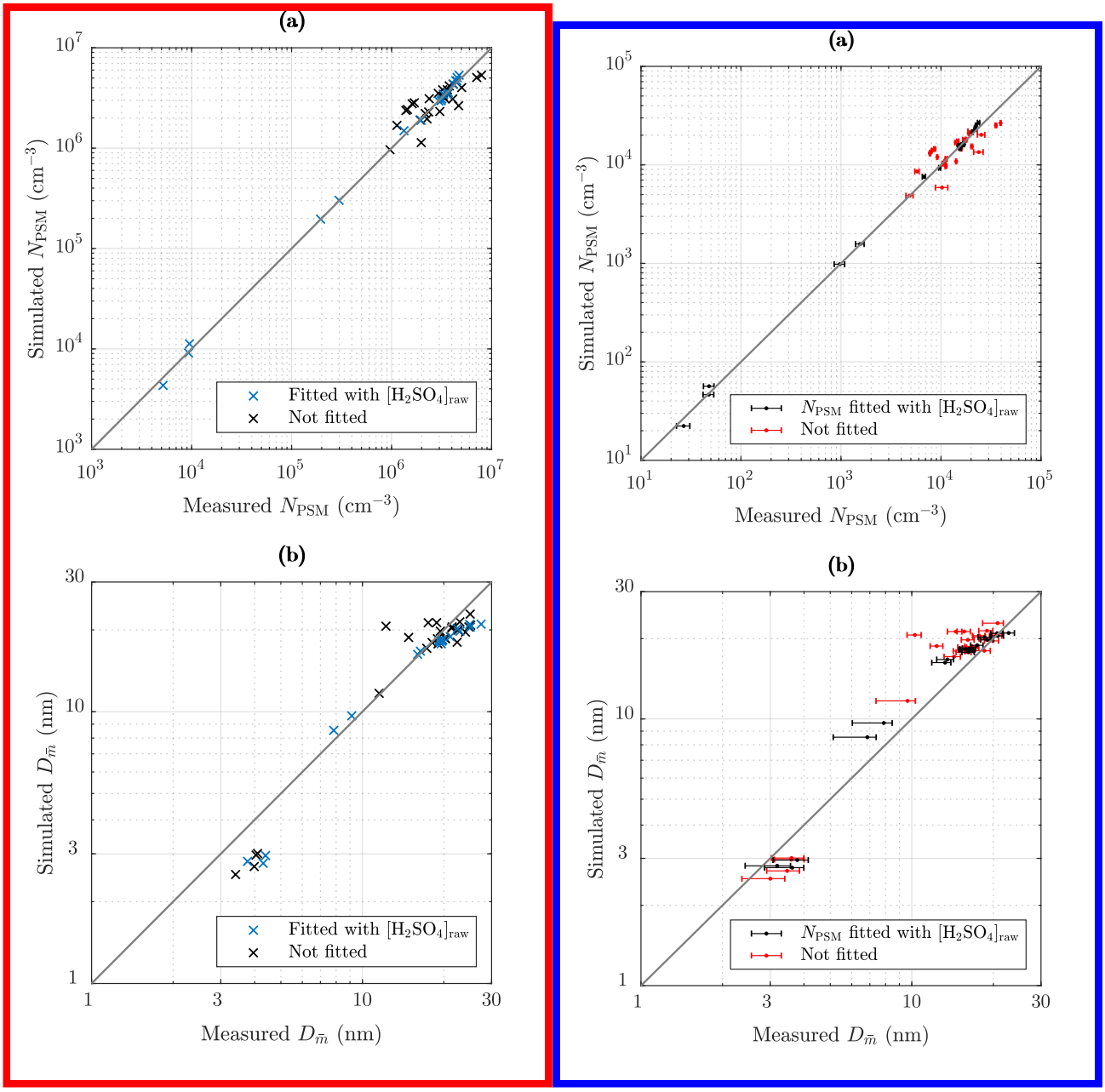

Figure 13. Comparison of the simulated and the measured (a) number concentrations of the particles larger than $\sim$ 1.3 nm and (b) the diameters with the average mass after the ED. The ~~blue crosses~~ black dots represent the cases for which N_{PSM} and $D_{\bar{m}}$ were obtained by fitting the value of $[H_2SO_4]_{\mathrm{raw}}$. The ~~black crosses~~ red dots represent the cases of the measurement sets 2 ... 4 in which the values of $[H_2SO_4]_{\mathrm{raw}}$ originated from an another case of the measurement set having the same T_{sa} value. The error bars in the pane (a) represent the standard deviations in concentration measurements, and the calculation of the error bars in the pane (b) is described in the Supplement.

cause according to the CNT, n_{sa} decreases with increasing $[H_2SO_4]$. This can be seen as ~~underestimated~~ overestimated particle sizes in mid-ranged particle sizes because ~~larger~~ smaller particle sizes would require ~~higher~~ lower $[H_2SO_4]_{raw}$ but that would cause ~~overestimated~~ underestimated N_{PSM}. To overcome the ~~overestimated~~ underestimated N_{PSM} in ~~low and high~~ mid-ranged $[H_2SO_4]$ values, k should be ~~decreased in low and high~~ increased in mid-ranged $[H_2SO_4]$ values, which indicates decreasing n_{sa} with increasing $[H_2SO_4]$. The point (2) can explain at least the discrepancy of the lower values of $D_{\bar{m}}$ because calculating $D_{\bar{m}}$ from the measured PSM, CPC 3775, and Nano-SMPS data is not straightforward, especially with the lower values of $D_{\bar{m}}$ in which the distributions measured by the Nano-SMPS are cut from the smaller diameter edge due to ~~diffusional losses~~very low detection efficiency. Therefore, $D_{\bar{m}}$ calculated from the measurement data may be overestimated with the lower values of $D_{\bar{m}}$. This is also seen as long error bars towards left, especially for $D_{\bar{m}}$ values smaller than 10 nm (see the Supplement for details). However, by comparing the measured and the simulated size distributions with $T_{sa} = 102\,°C$ in Fig. 11 (measured ~~$D_{\bar{m}} = 4.3\,nm$~~ $D_{\bar{m}} = 3.6\,nm$, simulated $D_{\bar{m}} = 2.8\,nm$), it can be seen that the larger diameter edges of the distribution do not correspond satisfactorily either, which implies (1) being the most possible explanation. Conversely, the discrepancy of the higher values of $D_{\bar{m}}$ can be partially explained by (3) because simulating those cases with the LN distribution only, even higher values of $D_{\bar{m}}$ are output. That implies the PL+LN model ~~overestimates~~ underestimates the N_{PL}/N ratio. The N_{PL}/N ratio is controlled by the value of γ, the proper functional form of which is still under development in the PL+LN model. The last point (4) can also explain the discrepancies but the direction of a discrepancy could be in one way or another. The ~~black crosses~~ red dots follow mainly the same curve as the ~~blue crosses~~ black dots with the exception of four cases in which the values of $D_{\bar{m}}$ are clearly overestimated. These cases belong to the measurement set 3 and have high T_{PTD}. This discrepancy raises the point (4) because there are clearly some uncertainties involved in the condensation process modeling when T_{PTD} is high. It can be related, e.g., to the activity coefficient function of H_2SO_4 because too low activity coefficient would cause too low vapor pressure of H_2SO_4 at the surface of a particle, which would cause too large particles.

Table 3 represents the ratios of the simulated N and M with the residence times of 1.4 s and 2.8 s. The simulated ratios follow the same behavior as the measured ratios: with a low T_{sa} value the ratios are below unity and with higher T_{sa} values the ratio of N increases but the ratio of M stays near unity. The ratios with a low T_{sa} value correspond well with the measured values, but according to the simulations, the ratio of N does not increase with increasing T_{sa} equally with the measured ratios. This implies the coagulation rate is underestimated in the model but the reason for that is unknown. The temperature with which the coagulation process would eliminate the effect of the nucleation process, resulting in the number concentration ratio of unity, is near 148 °C (near 142 °C according to the measurements).

5.4 Nucleation rate function

The nucleation rate function with the best correspondence between the measured and the simulated data having a type of Eq. (2) used in the simulations has the parameters presented in Tab. 4 and is thus

$$J([H_2SO_4],[H_2O],T) = 5.8 \times 10^{-26} \frac{[H_2SO_4]^{1.9}[H_2O]^{0.5}}{{p_{sa}}^{\circ}(T)^{0.75}}, \quad (11)$$

Table 3. The ratios of the simulated number concentrations and mass concentrations after the ED with the residence times of 1.4 s and 2.8 s, in the measurement set 4. The values in parentheses denote the measured values as presented in Tab. 2.

T_{sa} (°C)	$\frac{N(1.4\,\mathrm{s})}{N(2.8\,\mathrm{s})}$	$\frac{M(1.4\,\mathrm{s})}{M(2.8\,\mathrm{s})}$
135.5	0.66 (0.74)	0.25 (0.28)
150	1.04 (1.29)	0.88 (0.92)
160	1.07 (1.72)	0.99 (0.96)
164.5	1.06 (1.74)	0.96 (1.10)

where the concentrations are given in cm^{-3}, the saturation vapor pressure in Pa, and the nucleation rate is output in cm^{-3}. This function was applied within the environmental parameter ranges presented in Tab. 5. The ranges can be considered the ranges within which Eq. (11) is defined. However, because the major part of the nucleation occurs when $[\mathrm{H_2SO_4}]$ is high (nearer to the upper boundary than to the lower boundary), a wrong formulation of J in the $[\mathrm{H_2SO_4}]$ values lower than $2 \times 10^{11}\ \mathrm{cm}^{-3}$ would have only a minor effect on the model outputs. Therefore, an alternative range having $2 \times 10^{11}\ \mathrm{cm}^{-3}$ as a minimum boundary for $[\mathrm{H_2SO_4}]$ is a more credible range within which the obtained function for J produces reliable results.

Table 4. The parameters of the nucleation rate function with the best correspondence between the measured and the simulated data. The ranges of variation represent the resolution with which the exponents were altered during inverse modeling.

Parameter	Value
k	5.8×10^{-26}
n_{sa}	$1.9\,(\pm 0.1)$
n_{w}	$0.50\,(\pm 0.05)$
m_{sa}	$0.75\,(\pm 0.05)$

Because ${p_{\mathrm{sa}}}^{\circ}(T)$ has nearly equal exponential form with the saturation vapor pressure of $\mathrm{H_2O}$ (${p_{\mathrm{w}}}^{\circ}(T)$), ${p_{\mathrm{sa}}}^{\circ}(T)$ can be expressed approximately using ${p_{\mathrm{w}}}^{\circ}(T)$ with

$$ {p_{\mathrm{sa}}}^{\circ}(T) \approx 2.6 \times 10^{-10} {p_{\mathrm{w}}}^{\circ}(T)^2. \tag{12} $$

Hence, the magnitude of J remains as in Eq. (11) if it is expressed with ${p_{\mathrm{w}}}^{\circ}(T)$ using the form

$$ J([\mathrm{H_2SO_4}], [\mathrm{H_2O}], T) = 8.9 \times 10^{-19} \frac{[\mathrm{H_2SO_4}]^{1.9} [\mathrm{H_2O}]^{0.5}}{{p_{\mathrm{w}}}^{\circ}(T)^{1.5}} \tag{13} $$

or with both ${p_{\mathrm{sa}}}^{\circ}(T)$ and ${p_{\mathrm{w}}}^{\circ}(T)$ using, e.g., the form

$$ J([\mathrm{H_2SO_4}], [\mathrm{H_2O}], T) = 1.4 \times 10^{-23} \frac{[\mathrm{H_2SO_4}]^{1.9} [\mathrm{H_2O}]^{0.5}}{{p_{\mathrm{sa}}}^{\circ}(T)^{0.5}\, {p_{\mathrm{w}}}^{\circ}(T)^{0.5}} \tag{14} $$

Table 5. The environmental parameter ranges within which the nucleation rate function was applied.

Parameter	Unit	Lower boundary	Upper boundary
T	°C	-30	250
$[H_2SO_4]$	cm^{-3}	0 (2×10^{11})[a]	2×10^{14}
x_{sa}		0 (10^{-8})[a]	1.1×10^{-5}
$[H_2O]$	cm^{-3}	2×10^{16}	10^{18}
x_w		8×10^{-4}	0.04
RH	%	0.1	100

[a] Alternative range

or a different form

$$J([H_2SO_4],[H_2O],T) = 4.0 \times 10^{-25} \left(\frac{[H_2SO_4]}{p_{sa}{}^\circ(T)^{0.35}}\right)^{1.9} \left(\frac{[H_2O]}{p_w{}^\circ(T)^{0.35}}\right)^{0.5}. \quad (15)$$

The exponent $n_{sa} = 1.9$ is in agreement with the former nucleation studies related to vehicle exhaust (Vouitsis et al., 2005) or to the atmosphere (Sihto et al., 2006; Riipinen et al., 2007; Brus et al., 2011; Riccobono et al., 2014) where n_{sa} lies usually between 1 and 2. The exponent $n_{sa} = 1.9$ corresponds best with the kinetic nucleation theory (McMurry and Friedlander, 1979) where $n_{sa} = 2$. Estimating n_{sa} from the measured particle number concentration provided the slope $n_{N_{PSM} \text{ vs. } [H_2SO_4]} = 0.4 \ldots 10$. The exponent n_w estimated from the measurement data is $n_{N_{PSM} \text{ vs. } RH_{PTD}} = 0.1 \ldots 0.2$, which is remarkably lower than the inversely modeled exponent $n_w = 0.5$. The slope of N_{PSM} versus T_{PTD} of the measurement set 3b in Fig. 7 is

$$n_{N_{PSM} \text{ vs. } T_{PTD}} = \frac{\partial \ln N_{PSM}}{\partial \ln T_{PTD}} = -6 \ldots -4 \quad (16)$$

but the inversely modeled exponent $m_{sa} = 0.75$ corresponds to the slope of -27, which is remarkably more negative than $n_{N_{PSM} \text{ vs. } T_{PTD}}$ due to the same uncertainties as involved with the slopes $n_{N_{PSM} \text{ vs. } [H_2SO_4]}$ and $n_{N_{PSM} \text{ vs. } RH_{PTD}}$. In conclusion, inverse modeling provides significantly more accurately the exponents over the method based on the measurement data only.

Nucleation rate was the highest in the PTD where the hot sample and the cold dilution air met. The major part of nucleation occurred in the beginning part of the aging chamber. No noticeable nucleation occurred in the ED though temperature reaches $-30\,°C$ locally, which is in agreement with the former studies. It provides partial validation for the obtained m_{sa} value.

6 Conclusions

Homogeneous H_2SO_4-H_2O nucleation rate measurements using the modified partial flow sampling system mimicking the dilution process occurring in a real-world driving situation were performed. The aerosol formed in the diluting and cooling sampling system was measured using the PSM, the CPC 3775, and the Nano-SMPS. The particle size distribution near the

detection limit of the Nano-SMPS showed clear disagreement with the PSM and the CPC3775 data, with major underestimation of the smaller particles and distortion of the size distribution shape due to the limitations involved in detecting small particles with simultaneous nucleation and particle growth using the Nano-SMPS. Thus, the data without the PSM and the CPC 3775 would unrealistically suggest log-normal shape for the size distributions.

The measurements were simulated with the aerosol dynamics code CFD-TUTMAM using nucleation rate which is explicitly defined as a function of temperature and the concentrations of H_2SO_4 and H_2O. Equation (2) was used as the functional form of nucleation rate. The parameters for Eq. (2) which resulted in the best prediction for particle number concentrations and size distributions were $n_{\mathrm{sa}} = 1.9$, $n_{\mathrm{w}} = 0.5$, and $m_{\mathrm{sa}} = 0.75$, thus providing the nucleation rate function Eq. (11) (or any of Eqs. (13) – (15)). As discussed in Sec. 5.3, the obtained exponent $n_{\mathrm{sa}} = 1.9$ may be slightly overestimated in high concentrations and slightly underestimated in low concentrations. Estimating these exponents using only the measured particle concentrations resulted in markedly higher uncertainties when compared to modeling them inversely using the CFD-TUTMAM code.

The raw sample was generated by evaporating H_2SO_4 and H_2O liquids. The concentration of H_2SO_4 was controlled by adjusting the temperature of the liquid, T_{sa}. The boundary condition for H_2SO_4 concentration, $[H_2SO_4]_{\mathrm{raw}}$, was handled as a fitting parameter to correspond the simulated size distributions with the measured ones. Particle sizes were small with low T_{sa} and the size distributions were not in a log-normal form. Therefore, using the PL+LN model to represent the size distributions in the CFD-TUTMAM was necessary.

In these measurements, particle formation was not observed with the H_2SO_4 concentrations below $5.7\times10^{12}\,\mathrm{cm}^{-3}$ at exhaust condition temperatures. However, with real vehicle exhaust, in the same sampling system used here, particle formation has been observed even with the concentration of $2.5\times10^{9}\,\mathrm{cm}^{-3}$ (Arnold et al., 2012). This indicates that the nucleation rate of the binary H_2SO_4-H_2O nucleation mechanism is lower than the nucleation rate in real exhaust. Therefore, the binary H_2SO_4-H_2O nucleation cannot be fully controlling the particle formation process; instead, other compounds, such as hydrocarbons, existing in real exhaust are likely to be involved in the process as well, which is in agreement with the former exhaust-related nucleation studies (Saito et al., 2002; Vaaraslahti et al., 2004; Meyer and Ristovski, 2007; Pirjola et al., 2015; Olin et al., 2015).

The obtained exponent $n_{\mathrm{sa}} = 1.9$ is in agreement with the former nucleation studies related to the atmosphere or vehicle exhaust ($n_{\mathrm{sa}} = 1 \ldots 2$) and corresponds best with the kinetic nucleation theory. However, the effects of $[H_2O]$ and T obtained here may differ from the former studies because the effects are not extensively studied in them. The functional form and especially the values of the nucleation exponents for the homogeneous H_2SO_4-H_2O nucleation rate obtained in this study helps in finding the currently unknown nucleation mechanism occurring in real vehicle or power plant boiler exhaust or in the atmosphere. It provides also the starting point for inverse modeling studies purposed to examine hydrocarbon-involved H_2SO_4-H_2O nucleation mechanism, which is likely occurred in real vehicle exhaust. It can also be used to improve air quality models by using it to model the effect of H_2SO_4-emitting traffic and power generation on the particle concentration in urban air.

Author contributions. M.O., J.A., T.R., and M.D.M. designed the experiments and M.O. and J.A. carried them out. M.O. analyzed the measurement data, developed the model code, and performed the simulations. M.R.T.P. designed the IC analysis. M.O. prepared the manuscript with contributions from all co-authors.

Competing interests. The authors declare that they have no conflict of interest.

5 *Acknowledgements.* This work was funded by Tampere University of Technology Graduate School and by the Maj and Tor Nessling Foundation (project number 2014452). The authors thank CSC and TCSC for the computational time. We also thank prof. Mikko Sipilä from University of Helsinki for lending the CI-inlet for the APi-TOF, the tofTools team for providing tools for mass spectrometry analysis, and M.Sc. Kalle Koivuniemi for Ion Chromatography measurements.

References

Alanen, J., Saukko, E., Lehtoranta, K., Murtonen, T., Timonen, H., Hillamo, R., Karjalainen, P., Kuuluvainen, H., Harra, J., Keskinen, J., and Rönkkö, T.: The formation and physical properties of the particle emissions from a natural gas engine, Fuel, 162, 155–161, https://doi.org/10.1016/j.fuel.2015.09.003, 2015.

Albriet, B., Sartelet, K., Lacour, S., Carissimo, B., and Seigneur, C.: Modelling aerosol number distributions from a vehicle exhaust with an aerosol CFD model, Atmos. Environ., 44, 1126–1137, https://doi.org/10.1016/j.atmosenv.2009.11.025, 2010.

Alföldy, B., Giechaskiel, B., Hofmann, W., and Drossinos, Y.: Size-distribution dependent lung deposition of diesel exhaust particles, J. Aerosol Sci., 40, 652–663, https://doi.org/10.1016/j.jaerosci.2009.04.009, 2009.

Arneth, A., Unger, N., Kulmala, M., and Andreae, M.: Clean the air, heat the planet?, Science, 326, 672–673, https://doi.org/10.1126/science.1181568, 2009.

Arnold, F., Pirjola, L., Rönkkö, T., Reichl, U., Schlager, H., Lähde, T., Heikkilä, J., and Keskinen, J.: First online measurements of sulfuric acid gas in modern heavy-duty diesel engine exhaust: Implications for nanoparticle formation, Environ. Sci. Technol., 46, 11 227–11 234, https://doi.org/10.1021/es302432s, 2012.

Beelen, R., Raaschou-Nielsen, O., Stafoggia, M., Andersen, Z., Weinmayr, G., Hoffmann, B., Wolf, K., Samoli, E., Fischer, P., Nieuwenhuijsen, M., Vineis, P., Xun, W., Katsouyanni, K., Dimakopoulou, K., Oudin, A., Forsberg, B., Modig, L., Havulinna, A., Lanki, T., Turunen, A., Oftedal, B., Nystad, W., Nafstad, P., De Faire, U., Pedersen, N., Östenson, C.-G., Fratiglioni, L., Penell, J., Korek, M., Pershagen, G., Eriksen, K., Overvad, K., Ellermann, T., Eeftens, M., Peeters, P., Meliefste, K., Wang, M., Bueno-De-Mesquita, B., Sugiri, D., Krämer, U., Heinrich, J., De Hoogh, K., Key, T., Peters, A., Hampel, R., Concin, H., Nagel, G., Ineichen, A., Schaffner, E., Probst-Hensch, N., Künzli, N., Schindler, C., Schikowski, T., Adam, M., Phuleria, H., Vilier, A., Clavel-Chapelon, F., Declercq, C., Grioni, S., Krogh, V., Tsai, M.-Y., Ricceri, F., Sacerdote, C., Galassi, C., Migliore, E., Ranzi, A., Cesaroni, G., Badaloni, C., Forastiere, F., Tamayo, I., Amiano, P., Dorronsoro, M., Katsoulis, M., Trichopoulou, A., Brunekreef, B., and Hoek, G.: Effects of long-term exposure to air pollution on natural-cause mortality: An analysis of 22 European cohorts within the multicentre ESCAPE project, Lancet, 383, 785–795, https://doi.org/10.1016/S0140-6736(13)62158-3, 2014.

Boucher, O., Randall, D., Artaxo, P., Bretherton, C., Feingold, G., Forster, P., Kerminen, V.-M., Kondo, Y., Liao, H., Lohmann, U., Rasch, P., Satheesh, S., Sherwood, S., Stevens, B., and Zhang, X.: Clouds and Aerosols, book section 7, p. 571–658, Cambridge University Press, Cambridge, United Kingdom and New York, NY, USA, https://doi.org/10.1017/CBO9781107415324.016, 2013.

Boulaud, D., Madelaine, G., Vigla, D., and Bricard, J.: Experimental study on the nucleation of water vapor sulfuric acid binary system, J. Chem. Phys., 66, 4854–4860, https://doi.org/10.1063/1.433823, 1977.

Brus, D., Neitola, K., Hyvärinen, A.-P., Petäjä, T., Vanhanen, J., Sipilä, M., Paasonen, P., Kulmala, M., and Lihavainen, H.: Homogenous nucleation of sulfuric acid and water at close to atmospherically relevant conditions, Atmos. Chem. Phys., 11, 5277–5287, https://doi.org/10.5194/acp-11-5277-2011, 2011.

Chen, L., Liang, Z., Zhang, X., and Shuai, S.: Characterizing particulate matter emissions from GDI and PFI vehicles under transient and cold start conditions, Fuel, 189, 131 – 140, https://doi.org/10.1016/j.fuel.2016.10.055, 2017.

Dockery, D., Pope III, C., Xu, X., Spengler, J., Ware, J., Fay, M., Ferris Jr., B., and Speizer, F.: An association between air pollution and mortality in six U.S. cities, New Engl. J. Med., 329, 1753–1759, https://doi.org/10.1056/NEJM199312093292401, 1993.

Giechaskiel, B., Ntziachristos, L., and Samaras, Z.: Effect of ejector dilutors on measurements of automotive exhaust gas aerosol size distributions, Meas. Sci. Technol., 20, 045 703, https://doi.org/10.1088/0957-0233/20/4/045703, 2009.

Gormley, P. G. and Kennedy, M.: Diffusion from a Stream Flowing through a Cylindrical Tube, P. Roy. Irish Acad. A, 52, 163–169, https://doi.org/10.2307/20488498, 1948.

Hale, B. N.: Temperature dependence of homogeneous nucleation rates for water: Near equivalence of the empirical fit of Wölk and Strey, and the scaled nucleation model, J. Chem. Phys., 122, 204 509, https://doi.org/10.1063/1.1906213, 2005.

Hanson, D. R. and Eisele, F.: Diffusion of H_2SO_4 in Humidified Nitrogen: Hydrated H_2SO_4, J. Phys. Chem. A, 104, 1715–1719, https://doi.org/10.1021/jp993622j, 2000.

Huang, L., Gong, S. L., Gordon, M., Liggio, J., Staebler, R. M., Stroud, C. A., Lu, G., Mihele, C., Brook, J. R., and Jia, C. Q.: Aerosol-computational fluid dynamics modeling of ultrafine and black carbon particle emission, dilution, and growth near roadways, Atmos. Chem. Phys., 14, 12 631–12 648, https://doi.org/10.5194/acp-14-12631-2014, 2014.

Hung, C., Krasnopoler, M. J., and Katz, J. L.: Condensation of a supersaturated vapor. VIII. The homogeneous nucleation of n-nonane, J. Chem. Phys., 90, 1856–1865, https://doi.org/10.1063/1.456027, 1989.

Jacobson, M. Z., Kittelson, D. B., and Watts, W. F.: Enhanced Coagulation Due to Evaporation and Its Effect on Nanoparticle Evolution, Environ. Sci. Technol., 39, 9486–9492, https://doi.org/10.1021/es0500299, 2005.

Johansson, C., Norman, M., and Gidhagen, L.: Spatial & temporal variations of PM10 and particle number concentrations in urban air, Environ. Monit. Assess., 127, 477–487, https://doi.org/10.1007/s10661-006-9296-4, 2007.

Jokinen, T., Sipilä, M., Junninen, H., Ehn, M., Lönn, G., Hakala, J., Petäjä, T., Mauldin III, R. L., Kulmala, M., and Worsnop, D. R.: Atmospheric sulphuric acid and neutral cluster measurements using CI-APi-TOF, Atmos. Chem. Phys., 12, 4117–4125, https://doi.org/10.5194/acp-12-4117-2012, 2012.

Karjalainen, P., Rönkkö, T., Pirjola, L., Heikkilä, J., Happonen, M., Arnold, F., Rothe, D., Bielaczyc, P., and Keskinen, J. .: Sulfur driven nucleation mode formation in diesel exhaust under transient driving conditions, Environ. Sci. Technol., 48, 2336–2343, https://doi.org/10.1021/es405009g, 2014.

Kashchiev, D.: On the relation between nucleation work, nucleus size, and nucleation rate, J. Chem. Phys., 76, 5098–5102, https://doi.org/10.1063/1.442808, 1982.

Keskinen, J. and Rönkkö, T.: Can real-world diesel exhaust particle size distribution be reproduced in the laboratory? A critical review, J. Air Waste Manage., 60, 1245–1255, https://doi.org/10.3155/1047-3289.60.10.1245, 2010.

Kirkby, J., Curtius, J., Almeida, J. a., Dunne, E., Duplissy, J., Ehrhart, S., Franchin, A., Gagné, S., Ickes, L., Kürten, A., Kupc, A., Metzger, A., Riccobono, F., Rondo, L., Schobesberger, S., Tsagkogeorgas, G., Wimmer, D., Amorim, A., Bianchi, F., Breitenlechner, M., David, A., Dommen, J., Downard, A., Ehn, M., Flagan, R. C., Haider, S., Hansel, A., Hauser, D., Jud, W., Junninen, H., Kreissl, F., Kvashin, A., Laaksonen, A., Lehtipalo, K., Lima, J., Lovejoy, E. R., Makhmutov, V., Mathot, S., Mikkilä, J., Minginette, P., Mogo, S., Nieminen, T., Onnela, A., Pereira, P., Petäjä, T., Schnitzhofer, R., Seinfeld, J. H., Sipilä, M., Stozhkov, Y., Stratmann, F., Tomé, A., Vanhanen, J., Viisanen, Y., Vrtala, A., Wagner, P. E., Walther, H., Weingartner, E., Wex, H., Winkler, P. M., Carslaw, K. S., Worsnop, D. R., Baltensperger, U., and Kulmala, M.: Role of sulphuric acid, ammonia and galactic cosmic rays in atmospheric aerosol nucleation, Nature, 476, 429–433, https://doi.org/10.1038/nature10343, 2011.

Kittelson, D.: Engines and nanoparticles: A review, J. Aerosol Sci., 29, 575–588, https://doi.org/10.1016/S0021-8502(97)10037-4, 1998.

Kittelson, D., Watts, W., Johnson, J., Thorne, C., Higham, C., Payne, M., Goodier, S., Warrens, C., Preston, H., Zink, U., Pickles, D., Goersmann, C., Twigg, M., Walker, A., and Boddy, R.: Effect of fuel and lube oil sulfur on the performance of a diesel exhaust gas continuously regenerating trap, Environ. Sci. Technol., 42, 9276–9282, https://doi.org/10.1021/es703270j, 2008.

Kulmala, M., Lehtinen, K., and Laaksonen, A.: Cluster activation theory as an explanation of the linear dependence between formation rate of 3 nm particles and sulphuric acid concentration, Atmos. Chem. Phys., 6, 787–793, https://doi.org/10.5194/acp-6-787-2006, 2006.

Kulmala, M., Kontkanen, J., Junninen, H., Lehtipalo, K., Manninen, H., Nieminen, T., Petäjä, T., Sipilä, M., Schobesberger, S., Rantala, P., Franchin, A., Jokinen, T., Järvinen, E., Äijälä, M., Kangasluoma, J., Hakala, J., Aalto, P., Paasonen, P., Mikkilä, J., Vanhanen, J., Aalto, J., Hakola, H., Makkonen, U., Ruuskanen, T., Mauldin III, R., Duplissy, J., Vehkamäki, H., Bäck, J., Kortelainen, A., Riipinen, I., Kurtén, T., Johnston, M., Smith, J., Ehn, M., Mentel, T., Lehtinen, K., Laaksonen, A., Kerminen, V.-M., and Worsnop, D.: Direct observations of atmospheric aerosol nucleation, Science, 339, 943–946, https://doi.org/10.1126/science.1227385, 2013.

Kupiainen-Määttä, O., Olenius, T., Korhonen, H., Malila, J., Dal Maso, M., Lehtinen, K., and Vehkamäki, H.: Critical cluster size cannot in practice be determined by slope analysis in atmospherically relevant applications, J. Aerosol Sci., 77, 127–144, https://doi.org/10.1016/j.jaerosci.2014.07.005, 2014.

Lähde, T., Rönkkö, T., Virtanen, A., Schuck, T. J., Pirjola, L., Hämeri, K., Kulmala, M., Arnold, F., Rothe, D., and Keskinen, J.: Heavy Duty Diesel Engine Exhaust Aerosol Particle and Ion Measurements, Environ. Sci. Technol., 43, 163–168, https://doi.org/10.1021/es801690h, 2009.

Lelieveld, J., Evans, J. S., Fnais, M., Giannadaki, D., and Pozzer, A.: The contribution of outdoor air pollution sources to premature mortality on a global scale, Nature, 525, 367–371, https://doi.org/10.1038/nature15371, 2015.

Lemmetty, M., Vehkamäki, H., Virtanen, A., Kulmala, M., and Keskinen, J.: Homogeneous Ternary H2SO4-NH3-H2O Nucleation and Diesel Exhaust: a Classical Approach, Aerosol Air Qual. Res., 7, 489–499, https://doi.org/10.4209/aaqr.2007.02.0008, 2007.

Lemmetty, M., Rönkkö, T., Virtanen, A., Keskinen, J., and Pirjola, L.: The effect of sulphur in diesel exhaust aerosol: Models compared with measurements, Aerosol Sci. Tech., 42, 916–929, https://doi.org/10.1080/02786820802360682, 2008.

Li, X. and Huang, Z.: Formation and transformation of volatile nanoparticles from a diesel engine during exhaust dilution, Chinese Sci. Bull., 57, https://doi.org/10.1007/s11434-011-4927-8, 2012.

Liu, Y. H., He, Z., and Chan, T. L.: Three-dimensional simulation of exhaust particle dispersion and concentration fields in the near-wake region of the studied ground vehicle, Aerosol Sci. Tech., 45, 1019–1030, https://doi.org/10.1080/02786826.2011.580021, 2011.

Lyyränen, J., Jokiniemi, J., Kauppinen, E. I., Backman, U., and Vesala, H.: Comparison of Different Dilution Methods for Measuring Diesel Particle Emissions, Aerosol Sci. Tech., 38, 12–23, https://doi.org/10.1080/02786820490247579, 2004.

Maricq, M., Chase, R., Xu, N., and Laing, P.: The effects of the catalytic converter and fuel sulfur level on motor vehicle particulate matter emissions: Light duty diesel vehicles, Environ. Sci. Technol., 36, 283–289, https://doi.org/10.1021/es010962l, 2002.

Maricq, M. M., Szente, J. J., and Jahr, K.: The Impact of Ethanol Fuel Blends on PM Emissions from a Light-Duty GDI Vehicle, Aerosol Sci. Tech., 46, 576–583, https://doi.org/10.1080/02786826.2011.648780, 2012.

McMurry, P. and Friedlander, S.: New particle formation in the presence of an aerosol, Atmos. Environ., 13, 1635–1651, https://doi.org/10.1016/0004-6981(79)90322-6, 1979.

Meyer, N. and Ristovski, Z.: Ternary Nucleation as a Mechanism for the Production of Diesel Nanoparticles: Experimental Analysis of the Volatile and Hygroscopic Properties of Diesel Exhaust Using the Volatilization and Humidification Tandem Differential Mobility Analyzer, Environ. Sci. Technol., 41, 7309–7314, https://doi.org/10.1021/es062574v, 2007.

Mordas, G., Manninen, H., Petäjä, T., Aalto, P., Hämeri, K., and Kulmala, M.: On operation of the ultra-fine water-based CPC TSI 3786 and comparison with other TSI models (TSI 3776, TSI 3772, TSI 3025, TSI 3010, TSI 3007), Aerosol Sci. Tech., 42, 152–158, https://doi.org/10.1080/02786820701846252, 2008.

Neitola, K., Brus, D., Makkonen, U., Sipilä, M., Mauldin III, R. L., Sarnela, N., Jokinen, T., Lihavainen, H., and Kulmala, M.: Total sulfate vs. sulfuric acid monomer concenterations in nucleation studies, Atmos. Chem. Phys., 15, 3429–3443, https://doi.org/10.5194/acp-15-3429-2015, 2015.

Ntziachristos, L., Giechaskiel, B., Pistikopoulos, P., Samaras, Z., Mathis, U., Mohr, M., Ristimäki, J., Keskinen, J., Mikkanen, P., Casati, R., Scheer, V., and Vogt, R.: Performance evaluation of a novel sampling and measurement system for exhaust particle characterization, SAE J.-Automot. Eng., pp. 2004–01–1439, https://doi.org/10.4271/2004-01-1439, 2004.

Olin, M., Dal Maso, M., and Rönkkö, T.: Sulfur driven nucleation in diesel exhaust: Simulations of a laboratory sampling system, in: Proceedings of the 18$^{\mathrm{th}}$ ETH-Conference on Combustion Generated Nanoparticles, Zürich, Switzerland, 22-25 June 2014, 2014.

Olin, M., Rönkkö, T., and Dal Maso, M.: CFD modeling of a vehicle exhaust laboratory sampling system: sulfur-driven nucleation and growth in diluting diesel exhaust, Atmos. Chem. Phys., 15, 5305–5323, https://doi.org/10.5194/acp-15-5305-2015, 2015.

Olin, M., Anttila, T., and Dal Maso, M.: Using a combined power law and log-normal distribution model to simulate particle formation and growth in a mobile aerosol chamber, Atmos. Chem. Phys., 16, 7067–7090, https://doi.org/10.5194/acp-16-7067-2016, 2016.

Paasonen, P., Nieminen, T., Asmi, E., Manninen, H., Petäjä, T., Plass-Dülmer, C., Flentje, H., Birmili, W., Wiedensohler, A., Horrak, U., Metzger, A., Hamed, A., Laaksonen, A., Facchini, M., Kerminen, V.-M., and Kulmala, M.: On the roles of sulphuric acid and low-volatility organic vapours in the initial steps of atmospheric new particle formation, Atmos. Chem. Phys., 10, 11 223–11 242, https://doi.org/10.5194/acp-10-11223-2010, 2010.

Pey, J., Querol, X., Alastuey, A., Rodriguez, S., Putaud, J., and Van Dingenen, R.: Source apportionment of urban fine and ultra-fine particle number concentration in a Western Mediterranean city, Atmos. Environ., 43, 4407–4415, https://doi.org/10.1016/j.atmosenv.2009.05.024, 2009.

Pirjola, L., Karl, M., Rönkkö, T., and Arnold, F.: Model studies of volatile diesel exhaust particle formation: are organic vapours involved in nucleation and growth?, Atmos. Chem. Phys., 15, 10 435–10 452, https://doi.org/10.5194/acp-15-10435-2015, 2015.

Pope, C., Burnett, R., Thun, M., Calle, E., Krewski, D., Ito, K., and Thurston, G.: Lung cancer, cardiopulmonary mortality, and long-term exposure to fine particulate air pollution, J. Amer. Med. Assoc., 287, 1132–1141, https://doi.org/10.1001/jama.287.9.1132, 2002.

Raes, F., Janssens, A., and Dingenen, R. V.: The role of ion-induced aerosol formation in the lower atmosphere, J. Aerosol Sci., 17, 466–470, https://doi.org/10.1016/0021-8502(86)90135-7, 1986.

Riccobono, F., Schobesberger, S., Scott, C. E., Dommen, J., Ortega, I. K., Rondo, L., Almeida, J., Amorim, A., Bianchi, F., Breitenlechner, M., David, A., Downard, A., Dunne, E. M., Duplissy, J., Ehrhart, S., Flagan, R. C., Franchin, A., Hansel, A., Junninen, H., Kajos, M., Keskinen, H., Kupc, A., Kürten, A., Kvashin, A. N., Laaksonen, A., Lehtipalo, K., Makhmutov, V., Mathot, S., Nieminen, T., Onnela, A., Petäjä, T., Praplan, A. P., Santos, F. D., Schallhart, S., Seinfeld, J. H., Sipilä, M., Spracklen, D. V., Stozhkov, Y., Stratmann, F., Tomé, A., Tsagkogeorgas, G., Vaattovaara, P., Viisanen, Y., Vrtala, A., Wagner, P. E., Weingartner, E., Wex, H., Wimmer, D., Carslaw, K. S., Curtius, J., Donahue, N. M., Kirkby, J., Kulmala, M., Worsnop, D. R., and Baltensperger, U.: Oxidation Products of Biogenic Emissions Contribute to Nucleation of Atmospheric Particles, Science, 344, 717–721, https://doi.org/10.1126/science.1243527, 2014.

Riipinen, I., Sihto, S.-L., Kulmala, M., Arnold, F., Dal Maso, M., Birmili, W., Saarnio, K., Teinilä, K., Kerminen, V.-M., Laaksonen, A., and Lehtinen, K. E. J.: Connections between atmospheric sulphuric acid and new particle formation during QUEST III–IV campaigns in Heidelberg and Hyytiälä, Atmos. Chem. Phys., 7, 1899–1914, https://doi.org/10.5194/acp-7-1899-2007, 2007.

Rissler, J., Swietlicki, E., Bengtsson, A., Boman, C., Pagels, J., Sandström, T., Blomberg, A., , and Löndahl, J.: Experimental determination of deposition of diesel exhaust particles in the human respiratory tract, J. Aerosol Sci., 48, 18–33, https://doi.org/10.1016/j.jaerosci.2012.01.005, 2012.

Rönkkö, T., Virtanen, A., Kannosto, J., Keskinen, J., Lappi, M., and Pirjola, L.: Nucleation mode particles with a nonvolatile core in the exhaust of a heavy duty diesel vehicle, Environ. Sci. Technol., 41, 6384–6389, https://doi.org/10.1021/es0705339, 2007.

Rönkkö, T., Lähde, T., Heikkilä, J., Pirjola, L., Bauschke, U., Arnold, F., Schlager, H., Rothe, D., Yli-Ojanperä, J., and Keskinen, J.: Effects of gaseous sulphuric acid on diesel exhaust nanoparticle formation and characteristics, Environ. Sci. Technol., 47, 11 882–11 889, https://doi.org/10.1021/es402354y, 2013.

Rönkkö, T., Pirjola, L., Ntziachristos, L., Heikkilä, J., Karjalainen, P., Hillamo, R., and Keskinen, J.: Vehicle Engines Produce Exhaust Nanoparticles Even When Not Fueled, Environ. Sci. Technol., 48, 2043–2050, https://doi.org/10.1021/es405687m, 2014.

Rönkkö, T., Kuuluvainen, H., Karjalainen, P., Keskinen, J., Hillamo, R., Niemi, J. V., Pirjola, L., Timonen, H. J., Saarikoski, S., Saukko, E., Järvinen, A., Silvennoinen, H., Rostedt, A., Olin, M., Yli-Ojanperä, J., Nousiainen, P., Kousa, A., and Dal Maso, M.: Traffic is a major source of atmospheric nanocluster aerosol, P. Natl. Acad. Sci. USA, 114, 7549–7554, https://doi.org/10.1073/pnas.1700830114, 2017.

Saito, K., Shinozaki, O., Seto, T., Kim, C.-S., Okuyama, K., Kwon, S.-B., and Lee, K. W.: The Origins of Nanoparticle Modes in the Number Distribution of Diesel Particulate Matter, in: SAE Technical Paper, SAE International, https://doi.org/10.4271/2002-01-1008, 2002.

Sakurai, H., Tobias, H., Park, K., Zarling, D., Docherty, K., Kittelson, D., McMurry, P., and Ziemann, P.: On-line measurements of diesel nanoparticle composition and volatility, Atmos. Environ., 37, 1199–1210, https://doi.org/10.1016/S1352-2310(02)01017-8, 2003.

Schneider, J., Hock, N., Weimer, S., Borrmann, S., Kirchner, U., Vogt, R., and Scheer, V.: Nucleation particles in diesel exhaust: Composition inferred from in situ mass spectrometric analysis, Environ. Sci. Technol., 39, 6153–6161, https://doi.org/10.1021/es049427m, 2005.

Sgro, L., Borghese, A., Speranza, L., Barone, A., Minutolo, P., Bruno, A., D'Anna, A., and D'Alessio, A.: Measurements of nanoparticles of organic carbon and soot in flames and vehicle exhausts, Environ. Sci. Technol., 42, 859–863, https://doi.org/10.1021/es070485s, 2008.

Sihto, S.-L., Kulmala, M., Kerminen, V.-M., Dal Maso, M., Petäjä, T., Riipinen, I., Korhonen, H., Arnold, F., Janson, R., Boy, M., Laaksonen, A., and Lehtinen, K. E. J.: Atmospheric sulphuric acid and aerosol formation: implications from atmospheric measurements for nucleation and early growth mechanisms, Atmos. Chem. Phys., 6, 4079–4091, https://doi.org/10.5194/acp-6-4079-2006, 2006.

Sihto, S.-L., Vuollekoski, H., Leppä, J., Riipinen, I., Kerminen, V.-M., Korhonen, H., Lehtinen, K., Boy, M., and Kulmala, M.: Aerosol dynamics simulations on the connection of sulphuric acid and new particle formation, Atmos. Chem. Phys., 9, 2933–2947, https://doi.org/10.5194/acp-9-2933-2009, 2009.

Stevens, R. G. and Pierce, J. R.: The contribution of plume-scale nucleation to global and regional aerosol and CCN concentrations: evaluation and sensitivity to emissions changes, Atmos. Chem. Phys., 14, 13 661–13 679, https://doi.org/10.5194/acp-14-13661-2014, 2014.

Stevens, R. G., Pierce, J. R., Brock, C. A., Reed, M. K., Crawford, J. H., Holloway, J. S., Ryerson, T. B., Huey, L. G., and Nowak, J. B.: Nucleation and growth of sulfate aerosol in coal-fired power plant plumes: sensitivity to background aerosol and meteorology, Atmos. Chem. Phys., 12, 189–206, https://doi.org/10.5194/acp-12-189-2012, 2012.

Sulonen, M. L., Kokko, M. E., Lakaniemi, A.-M., and Puhakka, J. A.: Electricity generation from tetrathionate in microbial fuel cells by acidophiles, J. Hazard. Mater., 284, 182–189, https://doi.org/10.1016/j.jhazmat.2014.10.045, 2015.

Taleb, D.-E., Ponche, J.-L., and Mirabel, P.: Vapor pressures in the ternary system water-nitric acid-sulfuric acid at low temperature: A reexamination, J. Geophys. Res.-Atmos., 101, 25 967–25 977, https://doi.org/10.1029/96JD02330, 1996.

Tobias, H., Beving, D., Ziemann, P., Sakurai, H., Zuk, M., McMurry, P., Zarling, D., Waytulonis, R., and Kittelson, D.: Chemical analysis of diesel engine nanoparticles using a nano-DMA/thermal desorption particle beam mass spectrometer, Environ. Sci. Technol., 35, 2233–2243, https://doi.org/10.1021/es0016654, 2001.

Uhrner, U., von Löwis, S., Vehkamäki, H., Wehner, B., Bräsel, S., Hermann, M., Stratmann, F., Kulmala, M., and Wiedensohler, A.: Dilution and aerosol dynamics within a diesel car exhaust plume-CFD simulations of on-road measurement conditions, Atmos. Environ., 41, 7440–7461, https://doi.org/10.1016/j.atmosenv.2007.05.057, 2007.

Vaaraslahti, K., Virtanen, A., Ristimäki, J., and Keskinen, J.: Nucleation Mode Formation in Heavy-Duty Diesel Exhaust with and without a Particulate Filter, Environ. Sci. Technol., 38, 4884–4890, https://doi.org/10.1021/es0353255, 2004.

Vaaraslahti, K., Keskinen, J., Giechaskiel, B., Solla, A., Murtonen, T., and Vesala, H.: Effect of lubricant on the formation of heavy-duty diesel exhaust nanoparticles, Environ. Sci. Technol., 39, 8497–8504, https://doi.org/10.1021/es0505503, 2005.

Vehkamäki, H. and Riipinen, I.: Thermodynamics and kinetics of atmospheric aerosol particle formation and growth, Chem. Soc. Rev., 41, 5160–5173, https://doi.org/10.1039/C2CS00002D, 2012.

Vehkamäki, H., Kulmala, M., Lehtinen, K., and Noppel, M.: Modelling binary homogeneous nucleation of water-sulfuric acid vapours: Parameterisation for high temperature emissions, Environ. Sci. Technol., 37, 3392–3398, https://doi.org/10.1021/es0263442, 2003.

Virtanen, A., Rönkkö, T., Kannosto, J., Ristimäki, J., Mäkelä, J., Keskinen, J., Pakkanen, T., Hillamo, R., Pirjola, L., and Hämeri, K.: Winter and summer time size distributions and densities of traffic-related aerosol particles at a busy highway in Helsinki, Atmos. Chem. Phys., 6, 2411–2421, https://doi.org/10.5194/acp-6-2411-2006, 2006.

Vogt, R., Scheer, V., Casati, R., and Benter, T.: On-road measurement of particle emission in the exhaust plume of a diesel passenger car, Environ. Sci. Technol., 37, 4070–4076, https://doi.org/10.1021/es0300315, 2003.

Vouitsis, E., Ntziachristos, L., and Samaras, Z.: Modelling of diesel exhaust aerosol during laboratory sampling, Atmos. Environ., 39, 1335 – 1345, https://doi.org/10.1016/j.atmosenv.2004.11.011, 2005.

Wang, Y. and Zhang, K.: Coupled turbulence and aerosol dynamics modeling of vehicle exhaust plumes using the CTAG model, Atmos. Environ., 59, 284–293, https://doi.org/10.1016/j.atmosenv.2012.04.062, 2012.

Weber, R. J., Marti, J. J., McMurry, P. H., Eisele, F. L., Tanner, D. J., and Jefferson, A.: Measured Atmospheric New Particle Formation Rates: Implications for Nucleation Mechanisms, Chem. Eng. Commun., 151, 53–64, https://doi.org/10.1080/00986449608936541, 1996.

Wölk, J. and Strey, R.: Homogeneous Nucleation of H_2O and D_2O in Comparison: The Isotope Effect, J. Phys. Chem. B, 105, 11 683–11 701, https://doi.org/10.1021/jp0115805, 2001.

Wyslouzil, B. E. and Wölk, J.: Overview: Homogeneous nucleation from the vapor phase—The experimental science, J. Chem. Phys., 145, 211 702, https://doi.org/10.1063/1.4962283, 2016.

Zeleznik, F. J.: Thermodynamic Properties of the Aqueous Sulfuric Acid System to 350 K, J. Phys. Chem. Ref. Data, 20, 1157–1200, https://doi.org/10.1063/1.555899, 1991.

Zhang, R., Khalizov, A., Wang, L., Hu, M., and Xu, W.: Nucleation and Growth of Nanoparticles in the Atmosphere, Chem. Rev., 112, 1957–2011, https://doi.org/10.1021/cr2001756, 2012.

~~Comparing simulated sulfuric acid concentrations to the measured concentrations~~

1 Comparing simulated sulfuric acid concentrations to the measured concentrations

In addition to determining sulfuric acid concentrations ($[H_2SO_4]$) through inverse modeling, they were also measured using a nitrate ion (NO_3^-) based chemical ionization Atmospheric Pressure interface Time-Of-Flight mass spectrometer (CI-APi-TOF, Jokinen et al. (2012)) and Ion Chromatography (IC, Sulonen et al. (2015)).

The CI-APi-TOF used NO_3^- ions as reagent ions to detect H_2SO_4 as bisulfate ions (HSO_4^-) and their clusters with nitric acid (HNO_3) in an APi-TOF mass spectrometer (Tofwerk AG, Switzerland and Aerodyne Research Inc., USA). The CI-APi-TOF outputs the concentrations of the measured ions as counts per second (c_{ion}) which need to be converted to absolute H_2SO_4 concentrations with the equation (Tröstl et al., 2016)

$$[H_2SO_4] = C \cdot \ln\left(1 + \frac{c_{HSO_4^-} + c_{HNO_3 \cdot HSO_4^-} + c_{H_2SO_4 \cdot HSO_4^-}}{c_{NO_3^-} + c_{HNO_3 \cdot NO_3^-} + c_{(HNO_3)_2 \cdot NO_3^-}}\right), \tag{S1}$$

where C is an experimentally determined calibration coefficient having the value of $1.3 \times 10^9\,\text{cm}^{-3}$ for the device used. The CI-APi-TOF works well in measuring H_2SO_4 from the atmosphere; however, because the concentrations in this experiment were significantly higher, the raw sample needed to be diluted. The sample flow rate to the CI-APi-TOF was (10.0 ± 0.2) slpm and it was prepared by diluting the raw sample with compressed air heated to 300 °C with the flow rate of almost 10 slpm. The dilution ratio, determined using carbon dioxide (CO_2) measurement, was 133 ± 7. This corresponds to the raw sample flow rate of (0.075 ± 0.004) slpm. The length of the sampling line before the dilution point was 70 mm and between the dilution point and the inlet of the CI-APi-TOF it was 1720 mm. According to the diffusional losses (Gormley and Kennedy, 1948), only the fraction of $(6 \pm 2) \times 10^{-4}$ of H_2SO_4 penetrated to the CI-APi-TOF inlet, of which the major contribution resulted from the sampling line before the dilution point having a very low flow rate.

The IC measurement was performed by sucking the raw sample with the flow rate of (2.76 ± 0.02) slpm through a gas washing bottle with a fritted disc and analyzing SO_4^{2-} ion concentration from the liquid sample with the IC instrument off-line. The length of the sampling line before the washing bottle was 525 mm, for which the calculated penetration due to diffusional losses is $(20.4 \pm 0.4)\,\%$. The effect of the line length on the diffusional losses was examined using also a sampling line having the length of 750 mm, for which the calculated penetration is $(12.9 \pm 0.4)\,\%$. However, according to the measured $[SO_4^{2-}]$, the line length had no effect on the penetrated fraction, implying over-predicted diffusional losses in the first part of the sampling line, probably due to saturating H_2SO_4 liquid onto the sampling lines. The gas washing bottle was filled with 130 ml of deionized Milli-Q water and the gas collecting time was 20 ... 360 min, depending on the expected $[H_2SO_4]$ in the raw sample. The collection efficiency of the gas washing bottle was measured by collecting the sample also with 80 ml of water having approximately half the bubbling height of 130 ml of water. According to the measured $[SO_4^{2-}]$, the amount of water had no effect on the results; thus, the collection efficiency was high, or at least the maximum achievable in the measurement conditions.

H_2SO_4 concentrations in the raw sample with different H_2SO_4 evaporator temperatures measured with the CI-APi-TOF and the IC are presented together with the simulated and theoretical concentrations in Fig. S1. Surprisingly, the CI-APi-TOF data are at a somewhat higher level compared to the lossless level which is probably partially accounted by the calculated diffusional losses between the measurement point and the device, which have a large uncertainty due to a very low sample flow rate. The reason why the data lies near the lossless level is presumably due to the direction of adjusting T_{sa} which was from high to low temperatures during the CI-APi-TOF measurement and the time waited for the CI-APi-TOF signal to stabilize was short with respect to the equilibration time of the sampling line. Performing higher saturator temperatures first can saturate the walls of the sampling lines with H_2SO_4 which could later act as preventing diffusional losses with lower saturator temperatures and thus result into the lossless level. The IC data are at the level of about 5 % of the lossless theoretical level, but there are also significant outliers at higher levels. The level of the IC data can be lowered due to the sample containing CO_2. CO_2 can lower the pH of the liquid sample in the gas washing bottle, which can further decrease the collection efficiency of SO_4^{2-}. The 5 % level of the IC data and the direction of the effect of CO_2 would denote maximum diffusional losses onto the sampling lines between the evaporator and the $[H_2SO_4]_{\text{raw}}$ measurement point of 95 %, which lies in the range of calculated diffusional losses of 0 ... 98 %.

Nevertheless, both the measured data sets agree well with the shape of the theoretical curve, which implies that $[H_2SO_4]_{raw}$ can be estimated using T_{sa}. However, the absolute value for $[H_2SO_4]_{raw}$ cannot be satisfactorily estimated using neither T_{sa} nor the measured concentrations due to the discrepancy of the measured concentrations. Therefore, the simulations of this study did not use the measured concentrations as the boundary conditions; instead, the $[H_2SO_4]_{raw}$ values were obtained through inverse modeling.

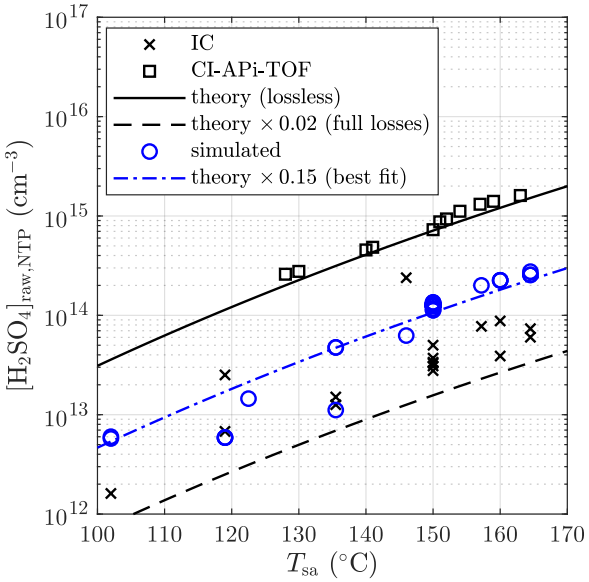

Figure S1. Simulated sulfuric acid concentrations in the raw sample compared to the measured and the theoretical concentrations with different sulfuric acid evaporator temperatures.

2 Error estimation for particle size distribution measurements

The disagreement of sub-6 nm particle size distributions measured by the combination of the PSM and the CPC 3775 and by the Nano-SMPS is examined by estimating the sources and the magnitudes of errors in measured concentrations for these devices.

2.1 Calculating the error bars for the combination of the PSM and the CPC 3775

The particle number size distributions are calculated using the step-wise method according to Lehtipalo et al. (2014) . Backwards-correcting the measured distributions to represent the distributions after the ED requires multiplying the data with the DR of the BD and dividing by the penetration efficiency of particles in the sampling lines between the ED and the measurement devices. Finally, the equation to obtain the distribution at particle size $D_{p,i}$ after the ED from the measured concentrations is

$$\nu(D_{p,i}) = \frac{N_i^{\text{smaller}} - N_i^{\text{larger}}}{\log(D_{p,i}^{\text{larger}}/D_{p,i}^{\text{smaller}}) \cdot p(D_{p,i}, L/Q)} \quad \text{(S2)}$$

where N_i^{smaller} and N_i^{larger} are particle number concentrations measured with the D_{50}-cut-sizes of $D_{\text{p},i}^{\text{smaller}}$ and $D_{\text{p},i}^{\text{larger}}$, respectively. $D_{\text{p},i}$ is the geometric mean diameter of the D_{50}-cut-sizes and $p(D_{\text{p},i}, L/Q)$ is the penetration efficiency of particles with a diameter of $D_{\text{p},i}$ in a sampling line with a length of $L_{\text{lines}} = L$ and flow rate of $Q_{\text{lines}} = Q$, according to diffusional losses calculated with the equations of Gormley and Kennedy (1948) . This penetration efficiency takes also the BD into account because its operation principle is also based on diffusional losses; thus, L denotes the effective length of the combined effect of the sampling lines and the BD.

Systematic errors for the calculated size distributions after the ED include the uncertainty of the cut-diameters and the uncertainty of the value of L/Q. Because the detection efficiency curves of the PSM and CPC 3775 are measured using particles having a different composition than H_2SO_4-H_2O, as in these measurements, and because environmental parameters, such as temperature, can have effects on the detection efficiency curves, the reported cut-diameters may not hold exactly. The uncertainty of 20 % is estimated for the cut-diameters and also for the ratio of the cut-diameters $D_{\text{p},i}^{\text{larger}}/D_{\text{p},i}^{\text{smaller}}$ because it is expected that if one of the cut-diameters is deviated towards smaller or larger particle sizes, another one is deviated towards the same direction. 10 % uncertainty is estimated for the value of L/Q, which includes the measurement uncertainty for both L and Q and the uncertainty in the equations of Gormley and Kennedy (1948) .

The standard deviations of the measured concentrations caused by the instability of the particle generation are in the range of 1 ... 25 %, depending on the concentration level and particle sizes: higher concentrations and larger particle sizes provided more stable particle generation compared to lower concentrations and smaller particle sizes.

The error bars for $\nu(D_{\text{p},i})$ can be calculated with the equation

$$\frac{\Delta\nu}{\nu} = \sqrt{\left(\frac{\partial\nu}{\partial N_i^{\text{smaller}}}\frac{\Delta N_i^{\text{smaller}}}{\nu}\right)^2 + \left(\frac{\partial\nu}{\partial N_i^{\text{larger}}}\frac{\Delta N_i^{\text{larger}}}{\nu}\right)^2 + \left(\frac{\partial\nu}{\partial \log(D_{\text{p},i}^{\text{larger}}/D_{\text{p},i}^{\text{smaller}})}\frac{\Delta \log(D_{\text{p},i}^{\text{larger}}/D_{\text{p},i}^{\text{smaller}})}{\nu}\right)^2 + \left(\frac{\partial\nu}{\partial p}\frac{\Delta p}{\nu}\right)^2}$$

$$= \sqrt{\left(\frac{\Delta N_i^{\text{smaller}}}{N_i^{\text{smaller}} - N_i^{\text{larger}}}\right)^2 + \left(\frac{\Delta N_i^{\text{larger}}}{N_i^{\text{smaller}} - N_i^{\text{larger}}}\right)^2 + \left(\frac{\Delta \log(D_{\text{p},i}^{\text{larger}}/D_{\text{p},i}^{\text{smaller}})}{\log(D_{\text{p},i}^{\text{larger}}/D_{\text{p},i}^{\text{smaller}})}\right)^2 + \left(\frac{\Delta p}{p}\right)^2} \quad \text{(S3)}$$

where $\Delta N_i^{\text{smaller}}$ and $\Delta N_i^{\text{smaller}}$ are the standard deviations of the concentrations, depending on the measurement case, the third term is 0.2^2 because $\Delta(D_{\text{p},i}^{\text{larger}}/D_{\text{p},i}^{\text{smaller}})/(D_{\text{p},i}^{\text{larger}}/D_{\text{p},i}^{\text{smaller}}) = 20\,\%$, and Δp depends on the particle size and is calculated with the equation

$$\frac{\Delta p}{p} = \sqrt{\left(\frac{\partial p}{\partial (L/Q)}\frac{\Delta (L/Q)}{p}\right)^2 + \left(\frac{\partial p}{\partial D_{\text{p},i}}\frac{\Delta D_{\text{p},i}}{p}\right)^2} \quad \text{(S4)}$$

using $\Delta(L/Q)/(L/Q) = 10\,\%$ and $\Delta D_{\text{p},i}/D_{\text{p},i} = 20\,\%$.

2.2 Calculating the error bars for the Nano-SMPS

The particle number size distributions reported by the Nano-SMPS device have already went through the manufacturer's inversion algorithm. Thus, the inverse modeling of this work does not try to predict the concentration measured as a function of time measured by the CPC 3776, acting as a particle counter in the Nano-SMPS system. Instead, the inverse modeling takes only the diffusional losses in the sampling lines and the CPC 3776 detection efficiency curve into account, but not, e.g., the radioactive charger efficiency and the diffusional losses inside the device. It is partly unknown what is included in the manufacturer's inversion algorithm, but at least the charger efficiency and the diffusional losses inside the device are included. The inversion algorithm probably includes also the CPC 3776 detection efficiency curve, f_{CPC}, but it is, however, included in the inverse modeling of this work because it seems that it may differ significantly from the curve reported by the manufacturer, according to Hermann et al. (2007) and Mordas et al. (2008) , as presented in Fig. S2. Unfortunately, the curve for the device used in these measurements is not measured; therefore, the inversion modeling uses the one reported by

Mordas et al. (2008) because it lies between the other two curves, representing an average one. The uncertainty of the detection efficiency at a specific diameter is calculated from the maximum range of variation of the detection efficiencies from these three different sources.

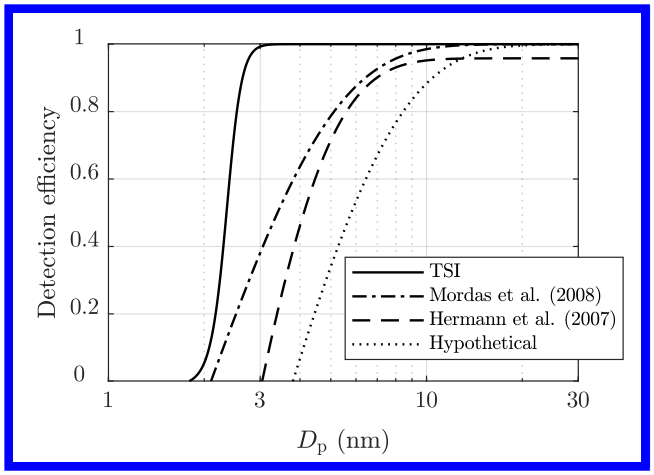

Figure S2. The CPC 3776 detection efficiency curves as a function of particle size reported by the manufacturer, Hermann et al. (2007) , and Mordas et al. (2008) . Additionally, a hypothetical curve correcting the disagreement between sub-6 nm particle size distributions measured by the Nano-SMPS and PSM+CPC system is presented.

The hypothetical detection efficiency curve presented in Fig. S2 is based on the curve reported by Mordas et al. (2008) but with different parameters. If this hypothetical curve is the actual curve of the device used, the size distributions as in Fig. 4 will be corrected to the distributions presented in Fig. S3, from which it can be seen that the size distributions measured by different devices correspond clearly better, at least for the two cases having the lowest T_{sa}. The PSM+CPC distribution for the case having the highest T_{sa} is probably overestimated because, according to Fig. 10 (c), the concentrations measured with different cut-diameters are on the same level, implying that there is not a notable amount of particles in that size range.

Other systematical errors, in addition to the uncertainty involved in the CPC 3776 detection efficiency curve, include the uncertainties of the charger efficiency, the diffusional losses, and the particle sizes interpreted by the manufacturer's inversion algorithm. The charger of the Nano-SMPS used was a TSI 3077 radioactive Kr-85 charger, which is based on charging particles bipolarly to the charge equilibrium state. The inversion algorithm uses the positive charge distribution function, $f_{charger}$, reported by Wiedensohler (1988) . It is a semi-empirical function in which the mobilities and masses of positive and negative ions in the carrier gas are fitted based on the charge distribution measurements
(Hussin et al., 1983; Adachi et al., 1985; Wiedensohler et al., 1986) made for particles larger than 5 nm in diameters.
Alonso et al. (1997) have measured the charge distributions down to particle diameters of 2.5 nm. Unfortunately, the charger distributions from all these measurements differ, especially for the smallest particle sizes, and have thus different ion parameters, due to different particle compositions, carrier gas compositions, and the accuracies of the particle size measurements. Therefore, the charger efficiency function selected in the manufacturer's inversion algorithm is not exact. Based on the differences between the results of these charge distribution measurements, the uncertainties of 30, 20, and 10 % for the charger efficiencies at particle diameters of 6, 10, and 20 nm, respectively, are estimated. Another factor causing uncertainty for the charger efficiency is how satisfactorily the charge distribution is developed to the equilibrium state. If the residence time inside the charger is too short (Alonso et al., 1997) , the activity of the charger is too low (de La Verpilliere et al., 2015) (e.g. if the activity of the charger is depleted due to a long operating life), or if the particle concentration is too high compared to the ion concentration (Wiedensohler et al., 2012) , the equilibrium state may not be reached and the charger efficiency is overestimated. According to the deviations of the charge distributions in the measurements of de La Verpilliere et al. (2015) from the charge distribution function of Wiedensohler (1988) , the uncertainties of 40, 30, and 20 % for the charger efficiencies at particle diameters of

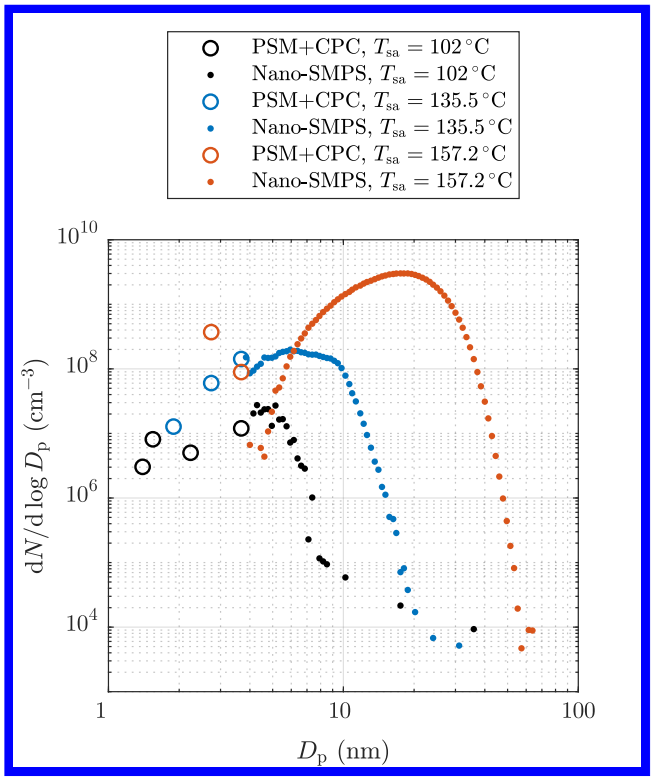

Figure S3. The corrected particle size distributions as in Fig. 4 if the detection efficiency curve of the CPC 3776 would be the hypothetical curve presented in Fig. S2.

2, 6, and 10 nm, respectively, are estimated. Because the particles before the Nano-SMPS are supposedly uncharged in this work, the possible incomplete reaching of the charge equilibrium state causes that the particles are less charged than predicted. Therefore, the concentrations would be underestimated, and thus the error bars related to this are considered only towards the positive direction.

The diffusional losses of the particles in the sampling lines of this work are based on the equations of Gormley and Kennedy (1948) using the L_{lines}/Q_{lines} parameter as in the case of the PSM+CPC system (the uncertainty of 10 % for the L_{lines}/Q_{lines} parameter in this case is again estimated). The correction of the diffusional losses inside the Nano-SMPS device is also based on those equations in the manufacturer's inversion algorithm. The algorithm uses an empirically fitted L_{device}/Q_{device} value which included the whole route of the particles inside the device even though the route is not a perfect laminar circular tube flow, for which the analytical solution by Gormley and Kennedy (1948) is based on. Therefore, the penetration function for particles inside the device, p_{device}, may not be exact and the uncertainty of 10 % for the L_{device}/Q_{device} parameter is estimated.

The correction factor assumed to exist in the inversion algorithm of the Nano-SMPS, to which the penetration in the sampling lines, p_{lines}, is added, is

$$C(D_{p,i}) = \frac{1}{f_{charger}(D_{p,i}) \cdot f_{CPC}(D_{p,i}) \cdot p_{device}(D_{p,i}, L_{device}/Q_{device}) \cdot p_{lines}(D_{p,i}, L_{lines}/Q_{lines})}. \quad \text{(S5)}$$

The concentration measured with a specific DMA (Differential Mobility Analyzer) voltage at a specific time, related to the particle diameter of $D_{p,i}$ (obtained though the inversion algorithm), is multiplied with $C(D_{p,i})$ in order to obtain the size

distribution in a location of L_{lines} before the device, i.e., after the ED in this case. For very small particles, all the four functions in Eq. (S5) have very low value; and thus, the value of $C(D_{\text{p},i})$ is extremely high. This is illustrated in Fig. S4 from which it can be observed that the value for sub-6 nm particles is several orders of magnitude. Very high correction factor denotes very low number of particle counts detected by the CPC at a specific diameter, and very low counts do not provide good accuracy due to statistics: there may be only a few randomly detected single particles or there may be even not a single detection at all during the time dedicated to that particle size, even though multiple scans have been performed for one measurement case. In the case of no or very low detection of single particles, the error bars cannot be calculated. Because the correction factor increases very steeply with decreasing particle size, the uncertainties involved in the functions in Eq. (S5) can deviate it in high extent. Another consequence of the steep behavior of the correction factor is that if there is even a minor error in the interpreted particle diameters, the value of the correction factor can be significantly misestimated. There are several factors that can cause error to the particle diameters measured by the Nano-SMPS (Wiedensohler et al., 2012) ; here, the uncertainty of 5 % is estimated for the diameters.

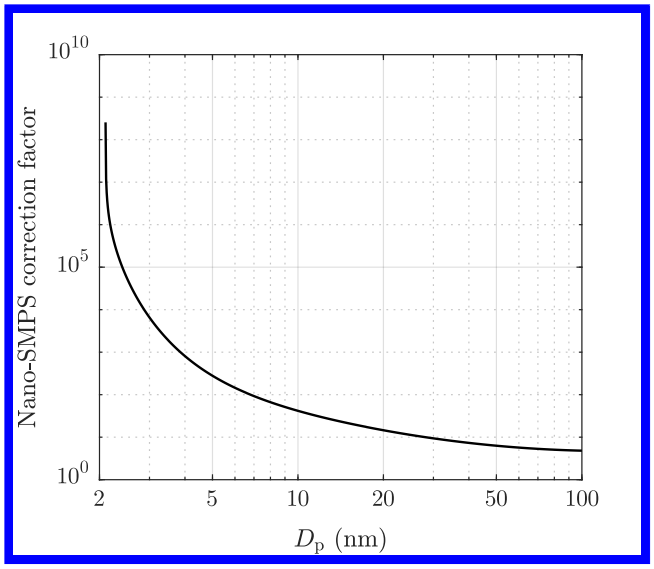

Figure S4. Nano-SMPS correction factor, as in Eq. (S5), used to correct the measured particle concentrations in the data inversion.

The error bars for the size distributions, $\nu(D_{\text{p},i})$, can be calculated with the equation

$$\frac{\Delta\nu}{\nu} = \sqrt{\left(\frac{\Delta\nu'}{\nu'}\right)^2 + \left(\frac{\Delta C}{C}\right)^2} \tag{S6}$$

where $\Delta\nu'$ is the standard deviation of the size distributions at the particle diameter of $D_{\text{p},i}$ output by the device, ν', and ΔC is the uncertainty of the Nano-SMPS correction factor. $\Delta\nu'$ represents the standard deviation caused by the instability in the particle generation, as in the case of the PSM+CPC system, but also by the low counting statistics for the particles sizes having a very low overall detection efficiency and for the particle sizes having low concentration in the measured case. ΔC is

calculated by

$$\frac{\Delta C}{C} = \sqrt{\left(\frac{\partial C}{\partial f_{\text{charger}}}\frac{\Delta f_{\text{charger}}}{C}\right)^2 + \left(\frac{\partial C}{\partial f_{\text{CPC}}}\frac{\Delta f_{\text{CPC}}}{C}\right)^2 + \left(\frac{\partial C}{\partial p_{\text{device}}}\frac{\Delta p_{\text{device}}}{C}\right)^2 + \left(\frac{\partial C}{\partial p_{\text{lines}}}\frac{\Delta p_{\text{lines}}}{C}\right)^2 + \left(\frac{\partial C}{\partial D_{\text{p},i}}\frac{\Delta D_{\text{p},i}}{C}\right)^2}$$

$$= \sqrt{\left(\frac{\Delta f_{\text{charger}}}{f_{\text{charger}}}\right)^2 + \left(\frac{\Delta f_{\text{CPC}}}{f_{\text{CPC}}}\right)^2 + \left(\frac{\Delta p_{\text{device}}}{p_{\text{device}}}\right)^2 + \left(\frac{\Delta p_{\text{lines}}}{p_{\text{lines}}}\right)^2 + \left(\frac{\partial C}{\partial D_{\text{p},i}}\frac{\Delta D_{\text{p},i}}{C}\right)^2} \tag{S7}$$

where $\Delta f_{\text{charger}}/f_{\text{charger}}$ and $\Delta f_{\text{CPC}}/f_{\text{CPC}}$ are the relative uncertainties for f_{charger} and f_{CPC} having the values mentioned before, Δp_{device} and Δp_{lines} are the uncertainties for the penetration efficiencies, p_{device} and p_{lines}, and the last term represents the uncertainty of C caused by the uncertainty of particle diameters. Δp_{device} and Δp_{lines} depend on the particle diameter and are calculated by

$$\Delta p_{\text{device}} = \frac{\partial p_{\text{device}}}{\partial(L_{\text{device}}/Q_{\text{device}})} \cdot \Delta(L_{\text{device}}/Q_{\text{device}})$$

$$\Delta p_{\text{lines}} = \frac{\partial p_{\text{lines}}}{\partial(L_{\text{lines}}/Q_{\text{lines}})} \cdot \Delta(L_{\text{lines}}/Q_{\text{lines}}) \tag{S8}$$

which differ from Eq. (S4) by missing the effect of the particle diameter because that effect is included in the last term of Eq. (S7). The last term represent the total effect of the particle diameter on C because the particle diameter is involved in all other four terms.

2.3 Calculated error bars for the size distributions

The relative uncertainties for the size distributions between 2 and 10 nm after the ED caused by the different uncertainties involved in the size distribution measurements are presented in Tab. S1. For the PSM+CPC system, the most significant systematic errors arise from the uncertainty in the cut-diameters (12 ... 30 %), partly due to correcting the diffusional losses in sampling lines needed in backwards-correcting the measured distributions to represent the distributions after the ED. For the Nano-SMPS, the uncertainty of the charger efficiency plays a major role in the systematic errors (40 ... 66 %), but the uncertainty of the CPC 3776 detection efficiency curve has also a significant role for the smallest particles (55 % for 3.7 nm). The error bars decrease steeply when measuring particles sized 10 nm or larger using the Nano-SMPS. Both devices are, in theory, capable in measuring the size distribution at 3.7 nm, but the error bars for the Nano-SMPS are clearly higher compared to the PSM+CPC system. Therefore, the PSM+CPC system suits better in measuring near that diameter.

Random errors caused by the instability of the particle generation and low counting statistics of the Nano-SMPS also have significant effects for the both devices if there is not a notable amount of concentration in a specific size range. In the case with $D_{\bar{m}} = 3.6\,\text{nm}$, there is a notable amount of concentration in the PSM+CPC size range, and thus, the error bars are relatively low (22 ... 61 %) for the PSM+CPC system. For the Nano-SMPS, the standard deviation for 6 nm particles is 72 %, which is, however, the most accurately measured particle size in that case: larger particles are inexistent and smaller particles are not detected; thus, low counting statistics cause high errors. In the case with $D_{\bar{m}} = 19\,\text{nm}$, the Nano-SMPS suits well in measuring at the particle size of 10 nm (the standard deviation of 10 % originating mainly from the instability in the particle generation) and also relatively well at the particle size of 6 nm (the standard deviation of 24 %), but the errors increase with the particles smaller than 6 nm. Conversely, the PSM+CPC system has high error bars because the concentration in the PSM+CPC size range is so low that the difference between the concentrations measured with different cut-diameters are smaller than the standard deviation of the concentrations (see Fig. 10), which is always a problem with the PSM having a cumulative nature in measuring concentrations, if the cut-diameters of the adjacent saturator flow rates are too near or the measured signal is too instable. This issue can be overcome by skipping the data measured with the adjacent cut-diameters or even by considering only the data measured with the smallest and with the largest cut-diameter. However, while the error bars will be narrower in this alternative method, the information on the shape of the size distribution in that size range will diminish.

Table S1. The percentual uncertainties for the size distributions after the ED, $\Delta\nu/\nu$ (%), for the selected particle diameters. The first seven lines represent the systematical error of the devices and they are independent of the measurement case. The last two lines represent the effect of the standard deviation for two measurement cases having small and large particles.

Device	PSM+CPC		Nano-SMPS		
D_p	2 nm	3.7 nm	3.7 nm	6 nm	10 nm
Diffusional losses in sampling lines $\left(\frac{\Delta(L_\mathrm{lines}/Q_\mathrm{lines})}{L_\mathrm{lines}/Q_\mathrm{lines}} = 10\,\%\right)$	8	3	4	2	1
Diffusional losses in sampling lines $\left(\frac{\Delta D_{\mathrm{p},i}}{D_{\mathrm{p},i}} = 20\,\%\right)$	30	12			
PSM detection efficiency $\left(\frac{\Delta(D_{\mathrm{p},i}^\mathrm{larger}/D_{\mathrm{p},i}^\mathrm{smaller})}{D_{\mathrm{p},i}^\mathrm{larger}/D_{\mathrm{p},i}^\mathrm{smaller}} = 20\,\%\right)$	20	20			
Kr-85 charger efficiency			66	61	40
CPC 3776 detection efficiency			55	8	0.7
Diffusional losses inside the DMA $\left(\frac{\Delta(L_\mathrm{lines}/Q_\mathrm{lines})}{L_\mathrm{lines}/Q_\mathrm{lines}} = 10\,\%\right)$			16	7	3
Nano-SMPS correction factor $\left(\frac{\Delta D_{\mathrm{p},i}}{D_{\mathrm{p},i}} = 5\,\%\right)$			32	17	10
Random error in $D_{\overline{m}} = 3.6\,\mathrm{nm}$ case (102 °C)	61	22	–[a]	72	–[a]
Random error in $D_{\overline{m}} = 19\,\mathrm{nm}$ case (157.2 °C)	∞[b]	250	–[a]	24	10

[a] Cannot be calculated due to insufficient particle counts.
[b] For this point, $\nu(2\,\mathrm{nm}) = 0$ but $\Delta\nu$ is a non-zero number due to standard deviation.

The error bars for the size distributions shown in Fig. 4 are presented in Fig. S5. By considering the error bars, the distributions from the both devices agree for the cases in panes (a) and (c), whereas the case in pane (b) has still some disagreement implying that other error sources than accounted here can be involved in the measurements using these devices. According to the error bars near the particle size of 4 nm connecting the two size distributions, the PSM+CPC system provides more reliable results in the cases in panes (a) and (b). Conversely, in the case in pane (c), the Nano-SMPS provides more reliable results because, although there are two points in the PSM+CPC distribution, the alternative method shows no particles at all. However, the error bars for the alternative method are high; thus, the probability of the existence of particles in the PSM+CPC size range is high. Nevertheless, the fraction of particles in that size range compared to the total particle count is, definitely, some orders of magnitude smaller than in the cases in panes (a) and (b). Figure S6 presents the error bars for the distributions shown in Fig. 11.

In conclusion, the suitability of the Nano-SMPS for the particle sizes smaller than ~10 nm is weak especially due to the uncertainties involved in the radioactive charger efficiency and the CPC 3776 detection efficiency. Wiedensohler et al. (2012) have performed an intercomparison of several mobility particle sizers, in which the different devices provided a good agreement for the particle sizes larger than ~15 nm but had significant disagreements for the smaller particle sizes, without explanation. Due to the incapability of the Nano-SMPS in determining the size distribution reliably in sub-10 nm diameter range, in all of the cases studied here and elsewhere, the PSM+CPC system suits clearly better in determining the size distribution in that particle size range, or at least the total number concentration of particles larger than ~1 nm.

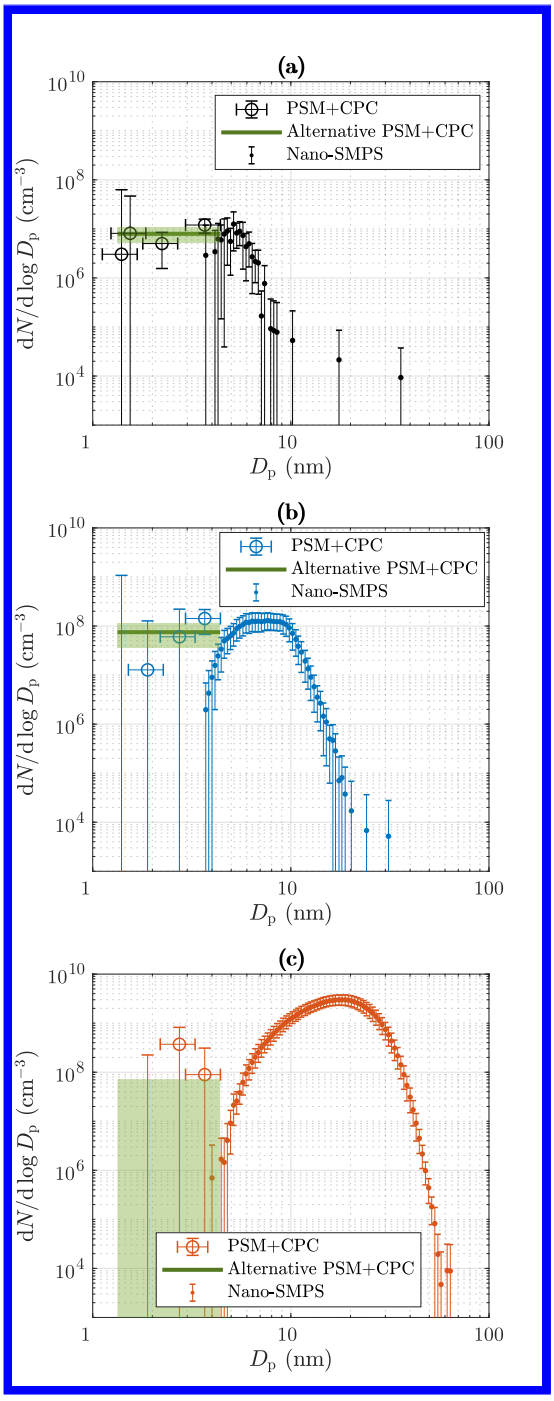

Figure S5. The measured size distributions for the measurement cases having the T_{sa} of (a) 102 °C, (b) 135.5 °C, and (c) 157.2 °C, as shown in Fig. 4, with the error bars. The alternative PSM+CPC distributions represent the distributions using only the concentrations measured with the smallest and the largest cut-diameters, in order to narrow the error bars. The green shaded areas denote the error bars for the distributions from the alternative method. The error bars for the particle sizes from the Nano-SMPS (±5 %) are not shown for clarity.

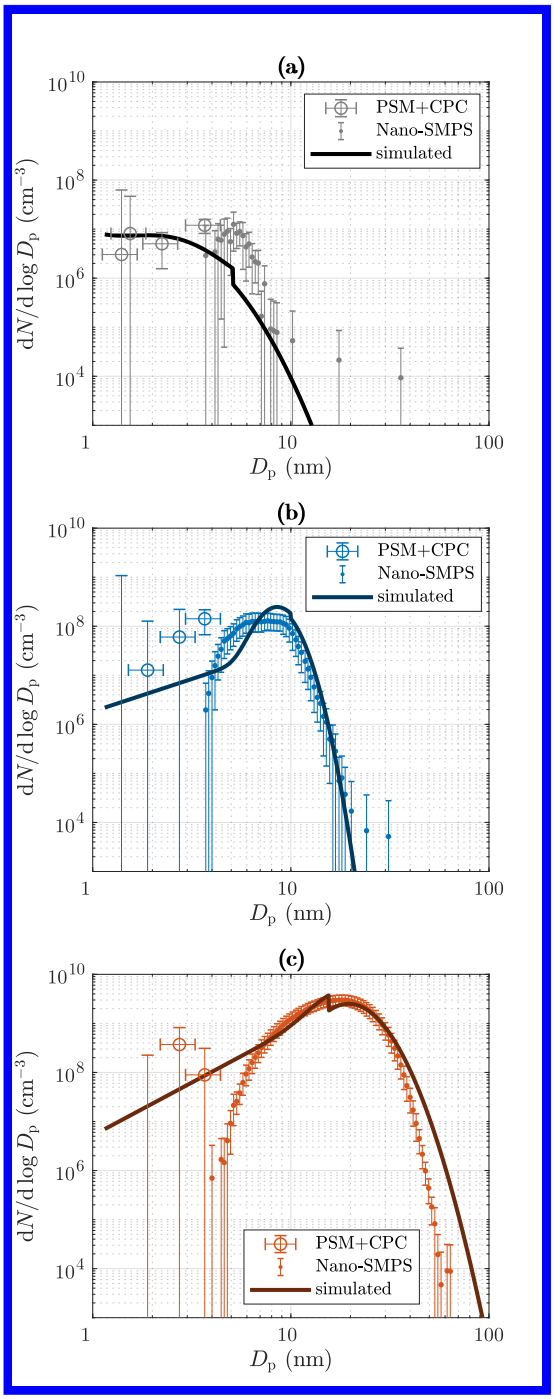

Figure S6. The simulated and measured size distributions for the measurement cases having the T_{sa} of (a) 102 °C, (b) 135.5 °C, and (c) 157.2 °C, as shown in Fig. 11, with the error bars. The error bars for the particle sizes from the Nano-SMPS (±5 %) are not shown for clarity.

2.4 Calculating the error bars for the diameters with the average mass

The diameter with the average mass of a distribution is calculated by

$$D_{\bar{m}} = \left(\frac{M'}{N}\right)^{\frac{1}{3}} = \left(\frac{\sum_i^{\mathrm{PC}} \nu(D_{\mathrm{p},i}) \cdot \mathrm{d}\log D_{\mathrm{p},i} \cdot D_{\mathrm{p},i}^3 + \sum_i^{\mathrm{NS}} \nu(D_{\mathrm{p},i}) \cdot \mathrm{d}\log D_{\mathrm{p},i} \cdot D_{\mathrm{p},i}^3}{\sum_i \nu(D_{\mathrm{p},i}) \cdot \mathrm{d}\log D_{\mathrm{p},i}}\right)^{\frac{1}{3}} = \left(\frac{M'_{\mathrm{PC}} + M'_{\mathrm{NS}}}{N}\right)^{\frac{1}{3}} \tag{S9}$$

where M' is the third moment of the distribution, M'_{PC} and M'_{NS} are the parts of the third moment from the PSM+CPC data and from the Nano-SMPS data, respectively, and N is the total number concentration.

The error bars for $D_{\bar{m}}$ can be calculated with the equation

$$\frac{\Delta D_{\bar{m}}}{D_{\bar{m}}} = \sqrt{\left(\frac{\Delta D_{\bar{m}}}{D_{\bar{m}}}\bigg|_{\Delta D_{\mathrm{p}}}\right)^2 + \left(\frac{\Delta D_{\bar{m}}}{D_{\bar{m}}}\bigg|_{\Delta \nu_{\mathrm{s}}}\right)^2 + \left(\frac{\Delta D_{\bar{m}}}{D_{\bar{m}}}\bigg|_{\Delta \nu_{\mathrm{r}}}\right)^2} \tag{S10}$$

where the first term represents the uncertainty caused by the uncertainty of the interpreted particle diameters, the second term the uncertainty caused by the uncertainty of the number size distribution due to the systematic errors of the devices, and the last term the uncertainty caused by the uncertainty of the number size distribution due to the random error.

The first term in Eq. (S10) is separated to the effects of the PSM+CPC system and of the Nano-SMPS, respectively:

$$\frac{\Delta D_{\bar{m}}}{D_{\bar{m}}}\bigg|_{\Delta D_{\mathrm{p}}} = \sqrt{\left(\frac{\Delta D_{\bar{m}}}{D_{\bar{m}}}\bigg|_{\Delta D_{\mathrm{p,PC_1}}}\right)^2 + \left(\frac{\Delta D_{\bar{m}}}{D_{\bar{m}}}\bigg|_{\Delta D_{\mathrm{p,NS_1}}}\right)^2}. \tag{S11}$$

Because particle diameters are dependent variables for a specific device, i.e., if one diameter is shifted to a direction, other diameters are most probably shifted to the same direction and with almost the same magnitude, the diameters in Eq. (S9) are separated to dependent and independent parts:

$$\begin{aligned} D_{\mathrm{p},i} &= D_{\mathrm{p,PC_1}} \cdot D'_{\mathrm{p},i} \\ D_{\mathrm{p},i} &= D_{\mathrm{p,NS_1}} \cdot D'_{\mathrm{p},i}. \end{aligned} \tag{S12}$$

where $D_{\mathrm{p,PC_1}}$ and $D_{\mathrm{p,NS_1}}$ denote the smallest diameters measured by the PSM+CPC system and by the Nano-SMPS, respectively, and $D'_{\mathrm{p},i}$ is a dimensionless variable denoting the ratios of all other diameters to the smallest diameter. Hence, the third moments can be expressed as

$$\begin{aligned} M'_{\mathrm{PC}} &= \sum_i^{\mathrm{PC}} \nu(D_{\mathrm{p},i}) \cdot \mathrm{d}\log D_{\mathrm{p},i} \cdot D_{\mathrm{p},i}^3 = \sum_i^{\mathrm{PC}} \nu(D_{\mathrm{p},i}) \cdot \mathrm{d}\log D_{\mathrm{p},i} \cdot (D_{\mathrm{p,PC_1}} \cdot D'_{\mathrm{p},i})^3 = D_{\mathrm{p,PC_1}}^3 \cdot \sum_i^{\mathrm{PC}} \nu(D_{\mathrm{p},i}) \cdot \mathrm{d}\log D_{\mathrm{p},i} \cdot D'^3_{\mathrm{p},i} \\ M'_{\mathrm{NS}} &= \sum_i^{\mathrm{NS}} \nu(D_{\mathrm{p},i}) \cdot \mathrm{d}\log D_{\mathrm{p},i} \cdot D_{\mathrm{p},i}^3 = \sum_i^{\mathrm{NS}} \nu(D_{\mathrm{p},i}) \cdot \mathrm{d}\log D_{\mathrm{p},i} \cdot (D_{\mathrm{p,NS_1}} \cdot D'_{\mathrm{p},i})^3 = D_{\mathrm{p,NS_1}}^3 \cdot \sum_i^{\mathrm{NS}} \nu(D_{\mathrm{p},i}) \cdot \mathrm{d}\log D_{\mathrm{p},i} \cdot D'^3_{\mathrm{p},i}. \end{aligned} \tag{S13}$$

The uncertainties in Eq. (S11) can now be calculated by

$$\left.\frac{\Delta D_{\bar{m}}}{D_{\bar{m}}}\right|_{\Delta D_{\mathrm{p,PC_1}}} = \frac{\partial D_{\bar{m}}}{\partial D_{\mathrm{p,PC_1}}} \cdot \frac{\Delta D_{\mathrm{p,PC_1}}}{D_{\bar{m}}} = \frac{1}{3}\frac{D_{\bar{m}}}{M'} \cdot \frac{\partial M'_{\mathrm{PC}}}{\partial D_{\mathrm{p,PC_1}}} \cdot \frac{\Delta D_{\mathrm{p,PC_1}}}{D_{\bar{m}}} = \frac{M'_{\mathrm{PC}}}{M'} \cdot \frac{\Delta D_{\mathrm{p,PC_1}}}{D_{\mathrm{p,PC_1}}}$$

$$\left.\frac{\Delta D_{\bar{m}}}{D_{\bar{m}}}\right|_{\Delta D_{\mathrm{p,NS_1}}} = \frac{\partial D_{\bar{m}}}{\partial D_{\mathrm{p,NS_1}}} \cdot \frac{\Delta D_{\mathrm{p,NS_1}}}{D_{\bar{m}}} = \frac{1}{3}\frac{D_{\bar{m}}}{M'} \cdot \frac{\partial M'_{\mathrm{NS}}}{\partial D_{\mathrm{p,NS_1}}} \cdot \frac{\Delta D_{\mathrm{p,NS_1}}}{D_{\bar{m}}} = \frac{M'_{\mathrm{NS}}}{M'} \cdot \frac{\Delta D_{\mathrm{p,NS_1}}}{D_{\mathrm{p,NS_1}}}. \tag{S14}$$

As 20 and 5 % uncertainties for the diameters for the PSM+CPC system and for the Nano-SMPS, respectively, were estimated, Eq. (S11) becomes

$$\left.\frac{\Delta D_{\bar{m}}}{D_{\bar{m}}}\right|_{\Delta D_{\mathrm{p}}} = \frac{1}{M'}\sqrt{\left(M'_{\mathrm{PC}} \cdot 0.2\right)^2 + \left(M'_{\mathrm{NS}} \cdot 0.05\right)^2}. \tag{S15}$$

The last two terms in Eq. (S10) related to the systematic and random errors separate the errors because the systematic errors for all size bins are presumably to the same direction and in almost the same magnitude and the random errors are randomly directed between different size bins because they are measured at different times. The number size distributions can be separated to the parts involving the sources for the systematic ($\Delta\nu_{\mathrm{s}}$) and for the random ($\Delta\nu_{\mathrm{r}}$) errors, respectively, using $\nu = \nu_{\mathrm{s}} \cdot \nu_{\mathrm{r}}$. The systematic errors for ν_{s} are independent variables for the different devices, but dependent variables for the different size bins of a specific device. Hence, the second term in Eq. (S10) is further separated to the PSM+CPC system and to the Nano-SMPS, respectively, using

$$\begin{aligned}\left.\frac{\Delta D_{\bar{m}}}{D_{\bar{m}}}\right|_{\Delta\nu_{\mathrm{s}}} &= \sqrt{\left(\left.\frac{\Delta D_{\bar{m}}}{D_{\bar{m}}}\right|_{\Delta\nu_{\mathrm{s,PC}}}\right)^2 + \left(\left.\frac{\Delta D_{\bar{m}}}{D_{\bar{m}}}\right|_{\Delta\nu_{\mathrm{s,NS}}}\right)^2} \\ &= \sqrt{\left[\frac{D_{\bar{m}}\left(\nu + \Delta\nu_{\mathrm{s,PC}}\right) - D_{\bar{m}}\left(\nu - \Delta\nu_{\mathrm{s,PC}}\right)}{2D_{\bar{m}}}\right]^2 + \left[\frac{D_{\bar{m}}\left(\nu + \Delta\nu_{\mathrm{s,NS}}\right) - D_{\bar{m}}\left(\nu - \Delta\nu_{\mathrm{s,NS}}\right)}{2D_{\bar{m}}}\right]^2}.\end{aligned} \tag{S16}$$

The last term in Eq. (S10), related to the random error, is calculated by

$$\begin{aligned}\left.\frac{\Delta D_{\bar{m}}}{D_{\bar{m}}}\right|_{\Delta\nu_{\mathrm{r}}} &= \sqrt{\sum_i \left[\frac{\partial D_{\bar{m}}}{\partial\nu_{\mathrm{r}}(D_{\mathrm{p},i})} \cdot \frac{\Delta\nu_{\mathrm{r}}(D_{\mathrm{p},i})}{D_{\bar{m}}}\right]^2} = \sqrt{\sum_i \left[\left(\frac{1}{3M'}\frac{\partial M'}{\partial\nu_{\mathrm{r}}(D_{\mathrm{p},i})} - \frac{1}{3N}\frac{\partial N}{\partial\nu_{\mathrm{r}}(D_{\mathrm{p},i})}\right)\Delta\nu_{\mathrm{r}}(D_{\mathrm{p},i})\right]^2} \\ &= \frac{1}{3}\sqrt{\sum_i \left[\left(\frac{\mathrm{d}\log D_{\mathrm{p},i} \cdot D_{\mathrm{p},i}^3}{M'} - \frac{\mathrm{d}\log D_{\mathrm{p},i}}{N}\right)\Delta\nu_{\mathrm{r}}(D_{\mathrm{p},i})\right]^2}.\end{aligned} \tag{S17}$$

The calculated error bars for the diameters with the average mass are presented in Fig. 13.

References

Adachi, M., Kousaka, Y., and Okuyama, K.: Unipolar and bipolar diffusion charging of ultrafine aerosol particles, J. Aerosol Sci., 16, 109 – 123, https://doi.org/https://doi.org/10.1016/0021-8502(85)90079-5, http://www.sciencedirect.com/science/article/pii/0021850285900795, 1985.

Alonso, M., Kousaka, Y., Nomura, T., Hashimoto, N., and Hashimoto, T.: Bipolar charging and neutralization of nanometer-sized aerosol particles, J. Aerosol Sci., 28, 1479 – 1490, https://doi.org/https://doi.org/10.1016/S0021-8502(97)00036-0, http://www.sciencedirect.com/science/article/pii/S0021850297000360, 1997.

de La Verpilliere, J. L., Swanson, J. J., and Boies, A. M.: Unsteady bipolar diffusion charging in aerosol neutralisers: A non-dimensional approach to predict charge distribution equilibrium behaviour, J. Aerosol Sci., 86, 55 – 68, https://doi.org/https://doi.org/10.1016/j.jaerosci.2015.03.006, http://www.sciencedirect.com/science/article/pii/S0021850215000440, 2015.

Gormley, P. G. and Kennedy, M.: Diffusion from a Stream Flowing through a Cylindrical Tube, P. Roy. Irish Acad. A, 52, 163–169, https://doi.org/10.2307/20488498, 1948.

Hermann, M., Wehner, B., Bischof, O., Han, H.-S., Krinke, T., Liu, W., Zerrath, A., and Wiedensohler, A.: Particle counting efficiencies of new TSI condensation particle counters, J. Aerosol Sci., 38, 674 – 682, https://doi.org/https://doi.org/10.1016/j.jaerosci.2007.05.001, http://www.sciencedirect.com/science/article/pii/S0021850207000705, 2007.

Hussin, A., Scheibel, H., Becker, K., and Porstendörfer, J.: Bipolar diffusion charging of aerosol particles—I: experimental results within the diameter range 4–30 nm, J. Aerosol Sci., 14, 671 – 677, https://doi.org/https://doi.org/10.1016/0021-8502(83)90071-X, http://www.sciencedirect.com/science/article/pii/002185028390071X, 1983.

Jokinen, T., Sipilä, M., Junninen, H., Ehn, M., Lönn, G., Hakala, J., Petäjä, T., Mauldin III, R. L., Kulmala, M., and Worsnop, D. R.: Atmospheric sulphuric acid and neutral cluster measurements using CI-APi-TOF, Atmos. Chem. Phys., 12, 4117–4125, https://doi.org/10.5194/acp-12-4117-2012, 2012.

Lehtipalo, K., Leppä, J., Kontkanen, J., Kangasluoma, J., Franchin, A., Wimmer, D., Schobesberger, S., Junninen, H., Petäjä, T., Sipilä, M., Mikkilä, J., Vanhanen, J., Worsnop, D., and Kulmala, M.: Methods for determining particle size distribution and growth rates between 1 and 3 nm using the Particle Size Magnifier, Bor. Env. Res., 19, 215–236, https://doi.org/10.1029/2001JD001010, 2014.

Mordas, G., Manninen, H., Petäjä, T., Aalto, P., Hämeri, K., and Kulmala, M.: On operation of the ultra-fine water-based CPC TSI 3786 and comparison with other TSI models (TSI 3776, TSI 3772, TSI 3025, TSI 3010, TSI 3007), Aerosol Sci. Tech., 42, 152–158, https://doi.org/10.1080/02786820701846252, 2008.

Sulonen, M. L., Kokko, M. E., Lakaniemi, A.-M., and Puhakka, J. A.: Electricity generation from tetrathionate in microbial fuel cells by acidophiles, J. Hazard. Mater., 284, 182–189, https://doi.org/10.1016/j.jhazmat.2014.10.045, 2015.

Tröstl, J., Chuang, W. K., Gordon, H., Heinritzi, M., Yan, C., Molteni, U., Ahlm, L., Frege, C., Bianchi, F., Wagner, R., Simon, M., Lehtipalo, K., Williamson, C., Craven, J. S., Duplissy, J., Adamov, A., Almeida, J., Bernhammer, A.-K., Breitenlechner, M., Brilke, S., Dias, A., Ehrhart, S., Flagan, R. C., Franchin, A., Fuchs, C., Guida, R., Gysel, M., Hansel, A., Hoyle, C. R., Jokinen, T., Junninen, H., Kangasluoma, J., Keskinen, H., Kim, J., Krapf, M., Kürten, A., Laaksonen, A., Lawler, M., Leiminger, M., Mathot, S., Möhler, O., Nieminen, T., Onnela, A., Petäjä, T., Piel, F. M., Miettinen, P., Rissanen, M. P., Rondo, L., Sarnela, N., Schobesberger, S., Sengupta, K., Sipilä, M., Smith, J. N., Steiner, G., Tomè, A., Virtanen, A., Wagner, A. C., Weingartner, E., Wimmer, D., Winkler, P. M., Ye, P., Carslaw, K. S., Curtius, J., Dommen, J., Kirkby, J., Kulmala, M., Riipinen, I., Worsnop, D. R., Donahue, N. M., and Baltensperger, U.: The role of low-volatility organic compounds in initial particle growth in the atmosphere, Nature, 533, 527–531, https://doi.org/10.1038/nature18271, 2016.

Wiedensohler, A.: An approximation of the bipolar charge distribution for particles in the submicron size range, J. Aerosol Sci., 19, 387 – 389, https://doi.org/https://doi.org/10.1016/0021-8502(88)90278-9, http://www.sciencedirect.com/science/article/pii/0021850288902789, 1988.

Wiedensohler, A., Lütkemeier, E., Feldpausch, M., and Helsper, C.: Investigation of the bipolar charge distribution at various gas conditions, J. Aerosol Sci., 17, 413 – 416, https://doi.org/https://doi.org/10.1016/0021-8502(86)90118-7, http://www.sciencedirect.com/science/article/pii/0021850286901187, 1986.

Wiedensohler, A., Birmili, W., Nowak, A., Sonntag, A., Weinhold, K., Merkel, M., Wehner, B., Tuch, T., Pfeifer, S., Fiebig, M., Fjäraa, A. M., Asmi, E., Sellegri, K., Depuy, R., Venzac, H., Villani, P., Laj, P., Aalto, P., Ogren, J. A., Swietlicki, E., Williams, P., Roldin, P., Quincey, P., Hüglin, C., Fierz-Schmidhauser, R., Gysel, M., Weingartner, E., Riccobono, F., Santos, S., Grüning, C., Faloon, K., Beddows, D., Harrison, R., Monahan, C., Jennings, S. G., O'Dowd, C. D., Marinoni, A., Horn, H.-G., Keck, L., Jiang, J., Scheckman, J., McMurry, P. H., Deng, Z., Zhao, C. S., Moerman, M., Henzing, B., de Leeuw, G., Löschau, G., and Bastian, S.: Mobility particle size spectrometers: harmonization of technical standards and data structure to facilitate high quality long-term observations of atmospheric particle number size distributions, Atmos. Meas. Tech., 5, 657–685, https://doi.org/10.5194/amt-5-657-2012, https://www.atmos-meas-tech.net/5/657/2012/, 2012.

Inversely modeling homogeneous H_2SO_4-H_2O nucleation rate in exhaust-related conditions

Miska Olin[1], Jenni Alanen[1,a], Marja R.T. Palmroth[2], Topi Rönkkö[1], and Miikka Dal Maso[1]

[1]Aerosol Physics Laboratory, Physics Unit, Tampere University, P.O. Box 692, 33014 Tampere, Finland
[2]Bio and Circular Economy, Faculty of Engineering and Natural Sciences, Tampere University, P.O. Box 541, 33014 Tampere, Finland
[a]now at: AGCO Power, Linnavuorentie 8-10, 37240 Linnavuori, Finland

Correspondence: Miska Olin (miska.olin@tuni.fi)

Abstract. Homogeneous sulfuric acid-water nucleation rate in conditions related to vehicle exhaust was measured and modeled. The measurements were performed by evaporating sulfuric acid and water liquids and by diluting and cooling the sample vapor with a sampling system mimicking the dilution process occurring in a real-world driving situation. The nucleation rate inside the measurement system was modeled inversely using CFD (computational fluid dynamics) and the aerosol dynamics code, CFD-TUTMAM (Tampere University of Technology Modal Aerosol Model for CFD). The nucleation exponents for the concentrations of sulfuric acid and water and for the saturation vapor pressure of sulfuric acid were found to be 1.9 ± 0.1, 0.50 ± 0.05, and 0.75 ± 0.05, respectively. These exponents can be used to examine the nucleation mechanisms occurring in exhaust from different combustion sources (internal combustion engines, power plant boilers, etc.) or in the atmosphere. Additionally, nucleation rate can be expressed with the exponents as a function of the concentrations of sulfuric acid and water and of temperature. The obtained function can be used as a starting point for inverse modeling studies of more complex nucleation mechanisms involving extra compounds in addition to sulfuric acid and water. More complex nucleation mechanisms, such as hydrocarbon-involving, are observed with real vehicle exhaust and are also supported by the results obtained in this study. Furthermore, the function can be used to improve air quality models by using it to model the effect of sulfuric acid-emitting traffic and power generation on the particle concentration in urban air.

1 Introduction

Airborne particles are related to adverse health effects (Dockery et al., 1993; Pope et al., 2002; Beelen et al., 2014; Lelieveld et al., 2015) and various effects on climate (Arneth et al., 2009; Boucher et al., 2013). In particular, adverse health effects are caused by the exposure to vehicle emissions which increase ultrafine particle concentration in urban air (Virtanen et al., 2006; Johansson et al., 2007; Pey et al., 2009) in the size range with high probability of lung deposition (Alföldy et al., 2009; Rissler et al., 2012).

Vehicles equipped with internal combustion engines generate nonvolatile particles (Rönkkö et al., 2007; Sgro et al., 2008; Maricq et al., 2012; Rönkkö et al., 2014; Chen et al., 2017); however, volatile particles are also formed after the combustion process during exhaust cooling (Kittelson, 1998; Lähde et al., 2009), i.e., when the exhaust is released from the tailpipe. Thus, volatile particles are formed through nucleation process; hence, they are called here nucleation mode particles.

An important characteristic of fine particles is the particle size distribution, as it determines the behavior of particles in the atmosphere and particle deposition to the respiratory system. Modeling studies provide information on the formation and evolution of exhaust-originated particles in the atmosphere (Jacobson et al., 2005; Stevens et al., 2012). To model the number concentration and the particle size of nucleation mode, the governing nucleation rate needs to be known.

The detailed nucleation mechanism controlling particle formation in cooling and diluting vehicle exhaust is currently unknown (Keskinen and Rönkkö, 2010). The nucleation mode particles contain at least water, sulfuric acid (H_2SO_4), and hydrocarbons (Kittelson, 1998; Tobias et al., 2001; Sakurai et al., 2003; Schneider et al., 2005). Therefore, it is likely that these compounds are involved in the nucleation process, but, on the other hand, some of them can end up in the nucleation mode through the initial growth of the newly-formed clusters. The most promising candidate for the main nucleating component in the particle formation process occurring in diesel exhaust is H_2SO_4, as it has been shown that the H_2SO_4 vapor concentration in vehicle exhaust (Rönkkö et al., 2013; Karjalainen et al., 2014), fuel sulfur content (Maricq et al., 2002; Vogt et al., 2003; Vaaraslahti et al., 2005; Kittelson et al., 2008), lubricating oil sulfur content (Vaaraslahti et al., 2005; Kittelson et al., 2008), and exhaust after-treatment system (Maricq et al., 2002; Vogt et al., 2003) correlate with nucleation mode number concentration, at least in the cases when the test vehicle has been equipped with an oxidative exhaust after-treatment system. The sulfur contents of fuel and lubricating oil are connected to the H_2SO_4 vapor concentration in the exhaust because the combustion of sulfur-containing compounds produces sulfur dioxide (SO_2) that is further oxidized to sulfur trioxide (SO_3) in an oxidative exhaust after-treatment system (Kittelson et al., 2008), and SO_3 finally produces H_2SO_4 when contacting with water (H_2O) vapor (Boulaud et al., 1977).

Particle formation due to H_2SO_4 in real vehicle exhaust plumes and in laboratory sampling systems has been previously simulated by several authors (Uhrner et al., 2007; Lemmetty et al., 2008; Albriet et al., 2010; Liu et al., 2011; Arnold et al., 2012; Li and Huang, 2012; Wang and Zhang, 2012; Huang et al., 2014), but all of them have modeled nucleation as binary homogeneous nucleation (BHN) of H_2SO_4 and water. Other possible nucleation mechanisms include activation-type (Kulmala et al., 2006), barrierless kinetic (McMurry and Friedlander, 1979), hydrocarbon-involving (Vaaraslahti et al., 2004; Paasonen et al., 2010), ternary H_2SO_4-H_2O-ammonia (Meyer and Ristovski, 2007), and ion-induced nucleation (Raes et al., 1986). The choice of binary homogeneous H_2SO_4-H_2O nucleation in studies involving vehicle exhaust is mainly made because it has been the only nucleation mechanism for which an explicitly defined formula for the nucleation rate (J) can be presented (Keskinen and Rönkkö, 2010). An explicit definition is required when the nucleation rate in cooling exhaust is modeled, as the nucleation rate has a steep temperature-dependency according to theory (Hale, 2005) and experiments (Wölk and Strey, 2001). The nucleation rate of BHN is derived from classical thermodynamics; thus, the theory is called the classical nucleation theory (CNT). The nucleation rate according to the CNT is explicitly defined as a function of H_2SO_4 and H_2O vapor concentrations ($[H_2SO_4]$ and $[H_2O]$) and temperature (T). The derivation of the CNT contains, however, a lot of assumptions and it is thus

quite uncertain (Vehkamäki and Riipinen, 2012). The largest uncertainty rises from the capillarity approximation, i.e. the physical properties of small newly-formed critical clusters can be expressed as the properties of bulk liquid (Wyslouzil and Wölk, 2016). Comparing experimental and theoretical nucleation rates, the CNT underestimates the temperature-dependency (Hung et al., 1989) and overestimates the sensitivity of J on $[\mathrm{H_2SO_4}]$ (Weber et al., 1996; Olin et al., 2014). These discrepancies entail that theoretically derived nucleation rates need to be corrected with a factor, ranging in several orders of magnitude, to agree with experimental nucleation rates.

Conversely, the nucleation rates of the other nucleation mechanisms are typically modeled as (Zhang et al., 2012)

$$J = k[\mathrm{H_2SO_4}]^n, \tag{1}$$

where k is an experimentally derived coefficient and n is the nucleation exponent presenting the sensitivity of J on $[\mathrm{H_2SO_4}]$. According to the first nucleation theorem (Kashchiev, 1982), n is also connected to the number of molecules in a critical cluster; however, due to assumptions included in the theorem, n is not exactly the number of molecules in a critical cluster in realistic conditions (Kupiainen-Määttä et al., 2014). The value for k is typically a constant that includes the effect of T and $[\mathrm{H_2O}]$, i.e., relative humidity (RH), (Sihto et al., 2009; Stevens and Pierce, 2014). A constant coefficient can be a satisfactory approximation in atmospheric nucleation experiments, where T and RH remain nearly constants. However, T and RH in a cooling and diluting exhaust are highly variable; thus, a constant coefficient cannot be used. The nucleation exponents, n, for $\mathrm{H_2SO_4}$ obtained from the atmospheric nucleation measurements (Sihto et al., 2006; Riipinen et al., 2007) and from the atmospherically-relevant laboratory experiments (Brus et al., 2011; Riccobono et al., 2014) lie usually between 1 and 2, which are much lower than the theoretical exponents ($n \gtrsim 5$, Vehkamäki et al. (2003)).

The first step in examining nucleation mechanisms, other than the CNT, in vehicle exhaust using experimental data was performed by Vouitsis et al. (2005). They concluded that nucleation mechanisms having $n = 2$, including barrierless kinetic nucleation mechanism, can predict nucleation rates in vehicle exhaust. Later, Olin et al. (2015) and Pirjola et al. (2015) focused on obtaining nucleation rates inversely, i.e. an initial function for J acts as an input to the model and is altered until the simulated particle concentration and distribution correspond to the measured ones. These modeling studies are based on the experiments (Vouitsis et al., 2005; Arnold et al., 2012; Rönkkö et al., 2013) where the exhaust of a diesel engine was sampled using a laboratory setup containing an engine dynamometer and a diluting sampling system (Ntziachristos et al., 2004).

Inverse modeling is a preferable method in obtaining nucleation rates in a diluting domain over the method based on calculating J by dividing the measured number concentration with an estimated volume of a nucleation region, because the volume of a nucleation region depends on n also. In the case of inverse modeling, there is no need to estimate the nucleation region because the model simulates J at every time step, in a model using temporal coordinates, or in every computational cell, in a model using spatial coordinates. Pirjola et al. (2015) modeled the dilution system with an aerosol dynamics model using temporal coordinates and concluded that hydrocarbons could be involved in the nucleation mechanism, and n lies between 1 and 2. However, because particle formation in diluting vehicle exhaust involves strong gradients in temperature and the concentrations of the compounds involved, information in spatial dimensions is also required to fully understand the particle formation process. For this reason, Olin et al. (2015) simulated aerosol dynamics using computational fluid dynamics (CFD) and concluded

that n is 0.25 or 1, depending on whether solid particles acting as an condensation sink for sulfuric acid are emitted or not, respectively. These values are very low compared to other studies and to the first nucleation theorem that restricts n to at least 1. Values below unity imply that there can be other compounds involved in the nucleation mechanism in addition to H_2SO_4.

Ammonia (NH_3) involved in H_2SO_4-H_2O nucleation (ternary H_2SO_4-H_2O-NH_3 nucleation), has a notable effect if the H_2SO_4 concentration is low and the NH_3 concentration is high (Lemmetty et al., 2007; Kirkby et al., 2011). The H_2SO_4 concentration in the atmosphere is low enough for the effect of NH_3 to be relevant (Kirkby et al., 2011), but in vehicle exhaust higher H_2SO_4 concentrations make the effect of NH_3 probably negligible. However, more recent vehicles are equipped with the selective catalytic reduction (SCR) system which decreases nitrogen oxide emissions but, on the other hand, increases NH_3 emissions. Therefore, NH_3 can be involved in the nucleation process occurring in vehicle exhaust of vehicles equipped with the SCR system (Lemmetty et al., 2007). The SCR system was not included in the experiments of Arnold et al. (2012) and Rönkkö et al. (2013) mentioned earlier; thus, other compounds involving in the nucleation process in those experiments are more likely hydrocarbons rather than NH_3.

In this paper, an improved aerosol dynamics model, CFD-TUTMAM (Tampere University of Technology Modal Aerosol Model for CFD), based on our previous model, CFD-TUTEAM (Tampere University of Technology Exhaust Aerosol Model for CFD) described in the reference Olin et al. (2015), is presented. The main improvement in the model is its capability to model the initial growth of the newly-formed clusters modally using our novel representation of the particle size distribution, the PL+LN (combined power law and log-normal distribution) model described in the reference Olin et al. (2016).

Laboratory experiments designed for nucleation rate modeling purposes are presented, in which the examination of the nucleation rate was aimed towards pure H_2SO_4-H_2O nucleation instead of nucleation associated with some unknown compounds existing in real vehicle exhaust. Although the pure binary nucleation seems not to be the principal nucleation mechanism in real exhaust (Saito et al., 2002; Vaaraslahti et al., 2004; Meyer and Ristovski, 2007; Pirjola et al., 2015), neglecting the unknown compounds is reasonable at this stage of nucleation studies because the knowledge of the nucleation mechanism of the pure binary nucleation is still at a very low level, and it should be examined more to better understand the nucleation process in real exhaust. Adding only one additional compound to nucleation experiments would cause one additional dimension to the measurement matrix of all changeable parameters considered and would thus increase the complexity of the experiments. Similarly, adding the concentration of an additional compound to inverse modeling, the complexity and the computational cost of the simulations would increase significantly. Therefore, it is reasonable to begin the inverse modeling studies using only the pure binary nucleation mechanism. Additionally, although there are studies suggesting that other compounds are involved in the nucleation process in real vehicle exhaust, it has not yet been directly shown that nucleation rate would be lower or higher with the absence of those compounds. Comparing the experiments with pure H_2SO_4-H_2O nucleation to the experiments with real exhaust can provide information on that.

The pure H_2SO_4-H_2O nucleation was generated by evaporating H_2SO_4 and H_2O liquids and using the dilution system that mimics a real-world dilution process of a driving vehicle (Ntziachristos et al., 2004). A similar principle of generating H_2SO_4 by evaporating it from a saturator has been used in the study of Neitola et al. (2015), in which the concentrations of H_2SO_4 and H_2O and temperatures were kept in an atmospherically-relevant range. In this study, they were kept in a vehicle

exhaust-relevant range; thus, the output is an explicitly defined formula for the H_2SO_4-H_2O nucleation rate in exhaust-related conditions. The formula is in the form of

$$J([H_2SO_4],[H_2O],T) = k\frac{[H_2SO_4]^{n_{sa}}[H_2O]^{n_w}}{{p_{sa}}^{\circ}(T)^{m_{sa}}}, \quad (2)$$

which is based on the formula hypothesized by Olin et al. (2015) but with an additional exponent m_{sa} for the saturation vapor pressure of sulfuric acid (${p_{sa}}^{\circ}$) to take temperature also into account. In Eq. (2), n_{sa} and n_w represent the nucleation exponents for $[H_2SO_4]$ and $[H_2O]$, respectively. The exponents may also depend on the concentration levels but due to the unknown dependency, only constant values are considered in this study.

The formulation obtained from this study helps in finding the nucleation mechanisms occurring in real vehicle exhaust or in the atmosphere. Similarly, it can be used to examine particle formation in coal-fired power plant exhaust, which is known to contain H_2SO_4 too (Stevens et al., 2012). E.g., the values of the nucleation exponents obtained in this study can provide information on the nucleation mechanisms because the values differ with respect to different nucleation mechanisms. Another use of the formulation is in improving air quality models by using it to model the effect of sulfuric acid-emitting traffic and power generation on the particle concentration in urban air.

2 Laboratory experiments

Laboratory experiments were designed to enable the examination of the effects of three parameters ($[H_2SO_4]$, $[H_2O]$, and T) on the H_2SO_4-H_2O nucleation rate. The experimental setup is presented in Fig. 1.

2.1 Artificial raw exhaust generation

The artificial raw exhaust sample was generated (the top part of Fig. 1) by evaporating 98 % H_2SO_4 liquid and deionized Milli-Q water. H_2SO_4 was held in a PTFE container and water in a glass bottle. The liquids were heated to temperatures T_{sa} and 43 °C, respectively, which determine the concentrations in the gas phase theoretically through the saturation vapor pressure. Dry and filtered compressed air was flown through the evaporators and mixed before heating to 350 °C. 2.7 % of carbon dioxide (CO_2) was also mixed with a sample to act as a tracer to determine the dilution ratio (DR) of the diluters. CO_2 was selected because it has no effect on the particle formation process and because it exists in real exhaust as well.

The computational domain in the CFD simulation shown in the bottom part of Fig. 1 begins before the sample enters to the PTD; thus, the concentrations of H_2SO_4 and H_2O, temperature, pressure (p), and flow rate need to be known at that point due to the requirement of the boundary conditions in the CFD simulation. T and p were measured at that point, $[H_2O]$ was calculated from the measured RH, and the flow rate was calculated from the DR of the porous tube diluter (PTD) with the aid of measured CO_2 concentrations.

The temperature of the raw sample was 243 °C and the mole fraction of H_2O (x_w) was 0.036, in average. Temperature before the PTD was lower than the heater temperature, 350 °C, because the sample cooled in the sampling lines, but the temperature of 243 °C corresponds well with the temperature of real exhaust when released from the tailpipe. In NTP conditions, $x_w = 0.036$

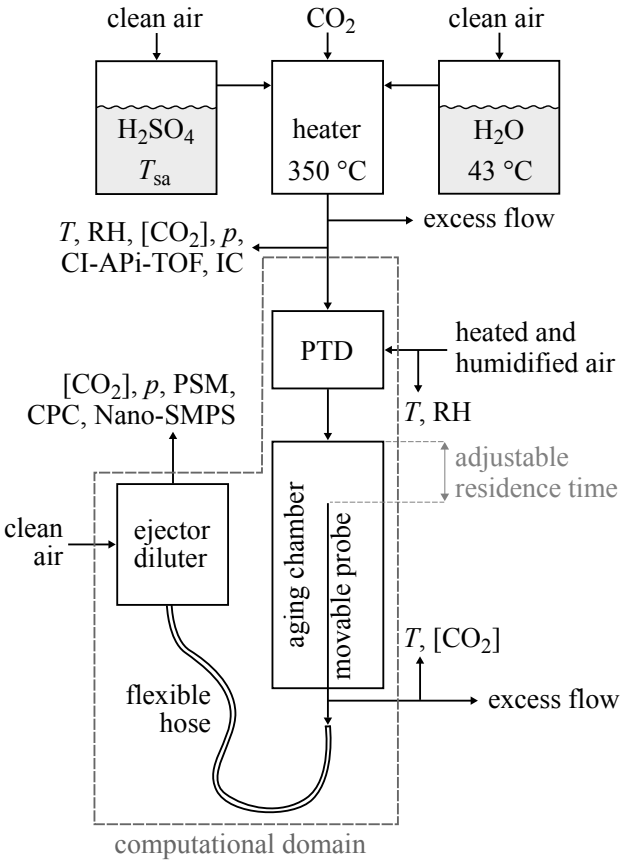

Figure 1. The experimental setup used to generate artificial exhaust and sample it with a diluting sampling system. The top part of the figure represents the artificial raw exhaust generation, which contains mixing and heating H_2SO_4 and H_2O vapors evaporated from liquids. The bottom part of the figure represents the raw exhaust sampling system, which consists of a porous tube diluter (PTD), an aging chamber, and an ejector diluter (ED). The computational domain of the CFD simulation is also shown in the figure.

corresponds to $[H_2O] = 9.0 \times 10^{17}\,\mathrm{cm}^{-3}$. The mole fractions in real diesel or gasoline exhaust range between 0.06 and 0.14, but the values higher than 0.036 with this experimental setup were not used, because a more humid sample caused the water vapor to condense as liquid water in the sampling lines.

The temperature of the H_2SO_4 evaporator, T_{sa}, was varied between $85\,^{\circ}\mathrm{C}$ and $164.5\,^{\circ}\mathrm{C}$ which correspond to the mole fractions (x_{sa}) between 2.2×10^{-7} and 1.1×10^{-5} in the raw sample. In NTP conditions, this range corresponds to the $[H_2SO_4]$ values between $5.7\times10^{12}\,\mathrm{cm}^{-3}$ and $2.8\times10^{14}\,\mathrm{cm}^{-3}$. These concentrations are higher than concentrations in real vehicle exhaust (typically between $10^8\,\mathrm{cm}^{-3}$ and $10^{14}\,\mathrm{cm}^{-3}$), because particle formation was not observed with the concentrations below $5.7\times10^{12}\,\mathrm{cm}^{-3}$. However, with real vehicle exhaust, in the same sampling system used here, particle formation has been observed even with the concentration of $2.5\times10^{9}\,\mathrm{cm}^{-3}$ (Arnold et al., 2012), indicating other compounds involving in the nucleation process.

The determination of $[H_2SO_4]$ in the raw sample in our experiment was not straightforward due to the uncertainties involved in the measurement of $[H_2SO_4]$. The detailed information on measuring it using a nitrate ion (NO_3^-) based chemical ionization Atmospheric Pressure interface Time-Of-Flight mass spectrometer (CI-APi-TOF, Jokinen et al. (2012)) and Ion Chromatography (IC, Sulonen et al. (2015)) is described in the Supplement. Estimating $[H_2SO_4]$ theoretically through the saturation vapor pressure in the temperature of T_{sa} provides some information on the dependency of $[H_2SO_4]$ on T_{sa} in the raw sample. However, the absolute concentrations cannot be satisfactorily estimated, firstly, because diffusional losses of H_2SO_4 onto the sampling lines between the H_2SO_4 evaporator and the PTD are high and uncertain, and secondly, because measuring H_2SO_4 is generally a challenging task due to high diffusional losses onto the walls of the sampling lines between the measurement point and the measurement device. High diffusional losses are caused by high diffusion coefficient of H_2SO_4. Additionally, a low flow rate from the H_2SO_4 evaporator (0.5 slpm) increases the diffusional losses before the measurement point. The diffusional losses before the measurement point, according to the equations reported by Gormley and Kennedy (1948) and to the humidity-dependent diffusion coefficient of H_2SO_4 reported by Hanson and Eisele (2000), are 98 % if the walls of the sampling lines are assumed fully condensing. However, some parts in the sampling lines have high concentrations of H_2SO_4 with high temperature, especially with high T_{sa} values. Therefore, these lines are probably partially saturated with H_2SO_4, which can act as preventing H_2SO_4 condensation onto the walls. Thus, the actual diffusional losses are estimated to be between 0 and 98 % and they can also depend on T_{sa} and on the saturation status of the sampling lines during a previous measurement point. In conclusion, the determination of $[H_2SO_4]$ in the raw sample was done through inverse modeling using measured particle diameter information (see Sec. 4.5). The output of the concentrations from inverse modeling denotes the diffusional losses of 43 ... 95 % depending on T_{sa}.

2.2 Raw exhaust sampling system

The sampling system used to dilute and cool the raw exhaust, presented in the bottom part of Fig. 1, was a modified partial flow sampling system (Ntziachristos et al., 2004) mimicking the dilution process occurring in a real-world driving situation. It consists of a PTD, an aging chamber, and an ejector diluter (ED). The PTD dilutes and cools the sample rapidly, which leads to new particle formation. The aging chamber is used to grow the newly-formed particles to detectable sizes and to continue the nucleation process. The ED is used to stop the particle formation and growth processes and to obtain the conditions of the sample required for measurement devices.

Dilution air used with the PTD and the ED was filtered compressed air. The ED used only dry ($RH \approx 3.6\,\%$) and unheated ($T \approx 20\,^\circ C$) dilution air, but the dilution air for the PTD was humidified ($RH_{PTD} = 2 ... 100\,\%$) and heated ($T_{PTD} = 27.5 ... 70\,^\circ C$). Humidifying the dilution air of the PTD was done by directing the compressed air flow through a container filled with deionized Milli-Q water. RH_{PTD} and T_{PTD} are the variable parameters used in examining the effect of $[H_2O]$ and T on J, which represent the conditions of the outdoor air acting in a dilution process in a real-world driving situation. The range of T_{PTD} represent higher temperatures compared to the temperature of the outdoor air, but lower temperatures were not used because 27.5 °C was the coldest temperature available with the laboratory setup having no cooling device.

In this experiment, the residence time in the aging chamber was made adjustable by a movable sampling probe inside the aging chamber. The sampling probe was connected to the ED with a flexible Tygon hose. The residence time from before the PTD to after the ED was altered within a range of 1.4 ... 2.8 s. Using a movable probe to alter the residence time has only a minor effect on the flow and temperature fields compared to altering the residence time with changing the flow rate in the aging chamber. Maintaining constant flow and temperature fields when studying the effect of the residence time is important, because variable fields would alter the turbulence level and temperatures in the aging chamber, both having effects on the measured particle concentration and thus causing difficulties to separate the effect of the residence time from the effect of turbulence or temperature on measured particle concentrations.

The DR of the PTD (DR_{PTD}) was controlled by the excess flow rate after the aging chamber and calculated by the measured $[CO_2]$ before the PTD and after the aging chamber. The DR_{PTD} was kept around 20 in all measurements. The DR of the ED (DR_{ED}) was controlled by the pressure of the dilution air used with the ED and calculated also using CO_2 measurements. The calculated DR_{ED} was around 10. Because the dilution ratios varied between different measurement points, all the aerosol results are multiplied with the total DR thus making the results comparable.

2.3 Particle measurement

Particle number concentration and size distribution was measured after the ED using Airmodus PSM A11 (Particle Size Magnifier A10 using Airmodus Condensation Particle Counter A20 as the particle counter), TSI CPC 3775 (Ultrafine Condensation Particle Counter), and TSI Nano-SMPS (Nano Scanning Mobility Particle Sizer using TSI CPC 3776 as the particle counter). The PSM and the CPC 3775 measure the particle number concentration (N_{PSM} and N_{CPC}) by counting particles with diameters larger than $\sim$ 1.15 nm (PSM) or $\sim$ 2.15 nm (CPC 3775). The D_{50}-cut-size (the particle diameter having the detection efficiency of 50 %) of the PSM can be altered, by adjusting its saturator flow rate, within the diameter range of 1.3 ... 3.1 nm. Additionally, the CPC 3775 has the D_{50}-cut-size of 4.0 nm and the CPC 3776 of 3.4 nm. The detection efficiency curves of the particle counters used are presented in Fig. 2. The Nano-SMPS measured, with the settings used in this experiment, the particle size distribution within the diameter range of 2 ... 65 nm; however, the detection of particles having diameters smaller than $\sim$ 6 nm are weakly detectable due to very low charging efficiency of the radioactive charger, low detection efficiency of the particle counter, and high diffusional losses inside the device, for very small particles. Nevertheless, using the data from the different saturator flow rates of the PSM together with the data from the CPC 3775, information on the particle size distribution around the range of 1.15 ... 6 nm is also obtained.

Due to too high particle number concentration for the PSM, aerosol measured with the PSM and the CPC 3775 was diluted with a bridge diluter (BD). It dilutes the concentration of larger particles ($D_p > 10\,\mathrm{nm}$) with the ratio of 250, but the DR increases with decreasing particle size due to diffusional losses, finally to the ratio of 1200 ($D_p = 1.15\,\mathrm{nm}$). The DR was measured with aerosol samples having the count median diameters (CMDs) of 2 ... 25 nm. The ratio of the sampling line length and the flow rate of the BD, a partially unknown variable, used in the diffusional losses function reported by Gormley and Kennedy (1948) was fitted to correspond with the DR measurement results; the obtained DRs are presented in Fig. 3.

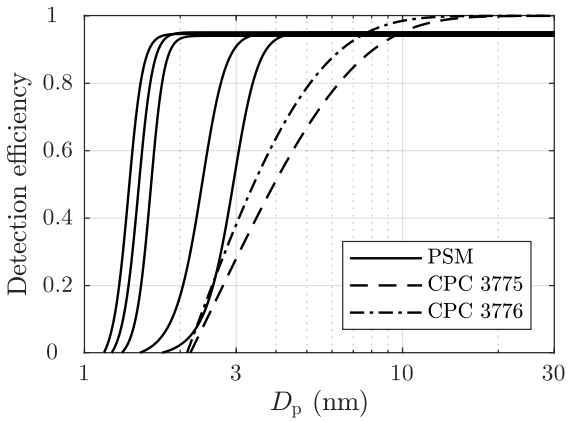

Figure 2. The detection efficiencies of the PSM, with five different saturator flow rates used in this experiment, and of the CPCs. The curves are exponential fittings based on the detection efficiencies reported by the manufacturers of the devices, excluding the CPC 3776 curve which is based on the efficiency measured by Mordas et al. (2008).

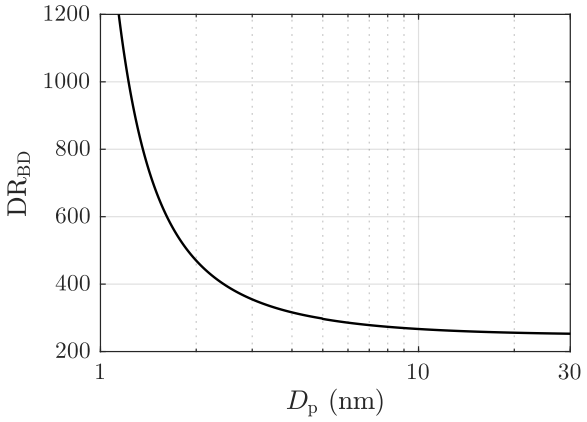

Figure 3. The dilution ratio of the bridge diluter with different particle diameters.

2.4 Measurement sets

By varying $[H_2SO_4]$ of the artificial raw exhaust sample and $[H_2O]$ and T of the dilution air separately and measuring the aerosol formed in the sampling system, the effects of the parameters on J can be examined. The effects of the parameters are included in Eq. (2) simply with the exponents n_{sa}, n_w, and m_{sa}. To obtain these three yet unknown values, at least three parameters were required to be varied in the experiments. Nevertheless, a fourth parameter, the residence time, was also varied to provide some validation for the obtained exponents. $[H_2O]$ and T of the dilution air were varied simply by humidifying and heating the dilution air flowing to the PTD and measuring RH and T from the dilution air. Varying $[H_2SO_4]$ of the raw sample was done by varying T_{sa}, and the values for $[H_2SO_4]$ in the raw sample were obtained through inverse modeling.

The varied conditions of the measurements are presented in Tab. 1, in which all the measurement points are divided according to the main outputs (n_{sa}, n_w, m_{sa}, and $\partial J/\partial t$) that measurement sets were designed to provide. Examining the effect of temperature (m_{sa}) was performed with the measurements of two types: varying T_{PTD} while keeping RH_{PTD} as a constant (Set 3a) and varying T_{PTD} while keeping the mole fraction of H_2O in the dilution air of the PTD ($x_{w,PTD}$) as a constant (Set 3b). The time-dependence of the nucleation rate ($\partial J/\partial t$) or, in the other words, the diminishment rate of J in a diluting sampling system is mainly the product of the exponents n_{sa} and m_{sa} in the following way: $[H_2SO_4]$ decreases steeply due to dilution, losses to walls, and condensation to particles resulting in diminishing J with the power of n_{sa}; simultaneously T decreases due to dilution and cooling of the sampling lines resulting in strengthening J with the power of m_{sa}. Examining the diminishment rate provides validation for the relation of n_{sa} and m_{sa} obtained from the simulations. We waited 2 ... 40 min for the particle size distributions to stabilize after the conditions was changed between the measurement points. When the particle formation process was satisfactorily stabilized, measurement data for each measurement point were recorded for 5 ... 40 min, depending on the stability of the particle generation.

Table 1. The varied conditions of the measurement points.

Set	Main output	T_{sa} (°C)	T_{PTD} (°C)	$x_{w,PTD}$ (10^{-3})	RH_{PTD} (%)	Residence time (s)
1	n_{sa}	85 ... 164.5	27.5	7.7	22	2.8
2	n_w	150	30	0.7 ... 42	2 ... 100	2.8
3a	m_{sa}	150	30 ... 70	9 ... 65	22	2.8
3b	m_{sa}	150	30 ... 70	44	22 ... 100	2.8
4	$\partial J/\partial t$	135.5 ... 164.5	27.5	7.7	22	1.4 ... 2.8

3 Experimental results

Figure 4 represents examples of particle size distributions measured with different H_2SO_4 evaporator temperatures, T_{sa}. The PSM+CPC data are calculated using the number concentrations measured with different saturator flow rates of the PSM and

with the CPC 3775, i.e. with different D_{50}-cut-sizes. To properly compare the data measured with different dilution ratios and sampling line lengths, the comparison requires backwards-corrected data, i.e., all data in the figure are corrected with the DR of the BD and with the diffusional losses caused by the sampling lines between the ED and the measurement devices. However, correcting the distributions backwards from the measured data to the distributions after the ED is not simple because that requires the shapes of the distributions within the whole diameter range to be known. The data of the PSM and the CPC 3775 cannot always provide real size distributions because the cumulative nature of the method using particle counters as the size distribution measurement can suffer from noise in measured concentration. For example, the PSM+CPC data with $T_{\mathrm{sa}} = 157.2\,^{\circ}\mathrm{C}$ shown in Fig. 4 implies that the concentration could increase with decreasing particle size, but the placing of the data points can be caused by the noise in the measured concentrations. On the other hand, the data implies that there are no particles smaller than $\sim$ 2.5 nm in diameter, but the data of the smaller particles can be invisible due to the noise in the measured concentrations (see the Supplement for the detailed error estimation of the size distributions). Hence, the unknown concentration of the particles smaller than $\sim$ 2.5 nm in diameter can have a significant effect on the total number concentration after the ED calculated from the measured data because these particles play the major role in the effect of the diffusional losses in the sampling lines and in the BD. Due to these uncertainties, the backwards-corrected data (denoting the distributions right after the ED) are not used when comparing the measured results with the simulated results later in this article. Nevertheless, the backwards-corrected data are used when presenting the distributions from all the aerosol devices together because the distributions cannot be presented without correcting them backwards due to different particle losses in the sampling lines of the different devices.

It can be observed that though the Nano-SMPS data are in a nearly log-normal form, there are also size distributions in the PSM+CPC diameter range. Particles generated with lower T_{sa} are lower in concentration and smaller than ones with higher T_{sa}; and higher fraction of particles are in the PSM+CPC diameter range. The smaller diameter edges of the log-normal size distributions measured by the Nano-SMPS do not connect with the distributions measured by the PSM and the CPC 3775 due to the weak detection efficiency of very small particles by the Nano-SMPS. Thus, the smaller diameter edges of the measured log-normal size distributions are not accurate. Similar disagreements of the data from these devices have been observed elsewhere also both in exhaust-related (Alanen et al., 2015; Rönkkö et al., 2017) and in atmospherically-related studies (Kulmala et al., 2013). By examining the combination of the size distributions measured by the PSM and the CPC 3775 and the size distributions measured by the Nano-SMPS, the real size distributions are not in a log-normal form. The detailed error estimation of the measured distributions and discussion on this disagreement can be found in the Supplement.

The particle number concentrations measured with the highest saturator flow rate of the PSM (N_{PSM}), i.e. the particles with diameters larger than $\sim$ 1.3 nm, and the diameters with the average mass ($D_{\bar{m}}$) of the measurement set 1 are presented in Fig. 5. $D_{\bar{m}}$ are calculated using the size distributions measured with the combination of the PSM, the CPC 3775, and the Nano-SMPS which are corrected with the diffusional losses in the sampling lines. The figure consists of data measured at two different days. It can be observed that N_{PSM} increases steeply with increasing $[\mathrm{H_2SO_4}]_{\mathrm{raw}}$ with lower $[\mathrm{H_2SO_4}]_{\mathrm{raw}}$ values, but the steepness decreases with increasing $[\mathrm{H_2SO_4}]_{\mathrm{raw}}$ due to increasing self-coagulation rate. With lower $[\mathrm{H_2SO_4}]_{\mathrm{raw}}$ values the slope of N_{PSM}

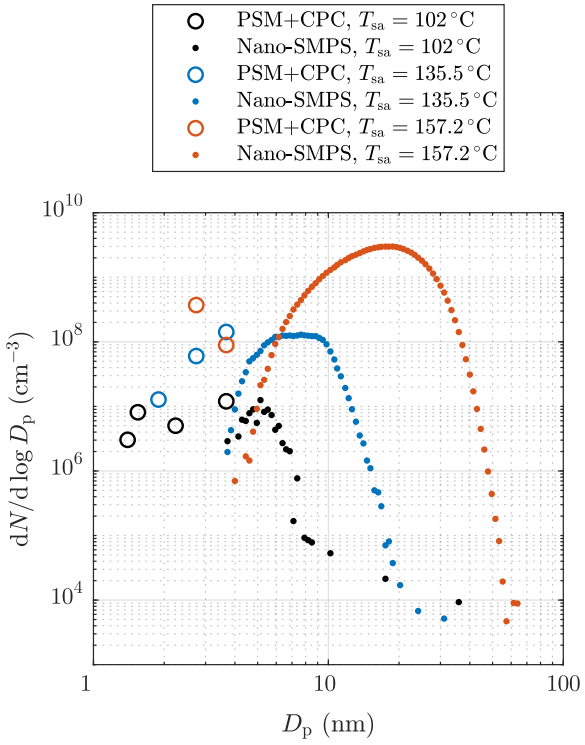

Figure 4. Examples of particle size distributions after the ED measured with different H_2SO_4 evaporator temperatures in the measurement set 1. The data are corrected with the DR of the BD and with the diffusional losses in the sampling lines after the ED. The concentrations are multiplied with the total DR of the sampling system. See the Supplement for error bars.

versus $[H_2SO_4]_{raw}$ in a log-log scale,

$$n_{N_{PSM}\text{ vs. }[H_2SO_4]_{raw}} = \frac{\partial \ln N_{PSM}}{\partial \ln [H_2SO_4]_{raw}}, \tag{3}$$

is approximately 10, but decreases to approximately 0.4 with decreasing $[H_2SO_4]_{raw}$. The slope of J versus $[H_2SO_4]$ is, by the definition of J (Eq. (2)),

$$n_{J\text{ vs. }[H_2SO_4]} = \frac{\partial \ln J}{\partial \ln [H_2SO_4]} = n_{sa}, \tag{4}$$

which is also the nucleation exponent for $[H_2SO_4]$. The slope $n_{N_{PSM}\text{ vs. }[H_2SO_4]_{raw}}$ can provide a rough estimate of the slope n_{sa} but due to the other aerosol processes, especially coagulation, having effects on the particle concentrations, the estimated slope can differ a lot from the real n_{sa} in the nucleation rate function. The slope at higher $[H_2SO_4]_{raw}$ values is usually decreased due to coagulation and the slope at lower $[H_2SO_4]_{raw}$ values can be increased due to decreased particle detection efficiency of smaller particles. Therefore, n_{sa} is expected to be within the range of 0.4 ... 10. Additionally, the estimated slope can also differ from n_{sa} because $n_{N_{PSM}\text{ vs. }[H_2SO_4]_{raw}}$ is based on $[H_2SO_4]$ in the raw sample rather than the value of $[H_2SO_4]$ in a specific location: $[H_2SO_4]$ decreases from the concentration in the raw sample several orders of magnitude during the dilution process.

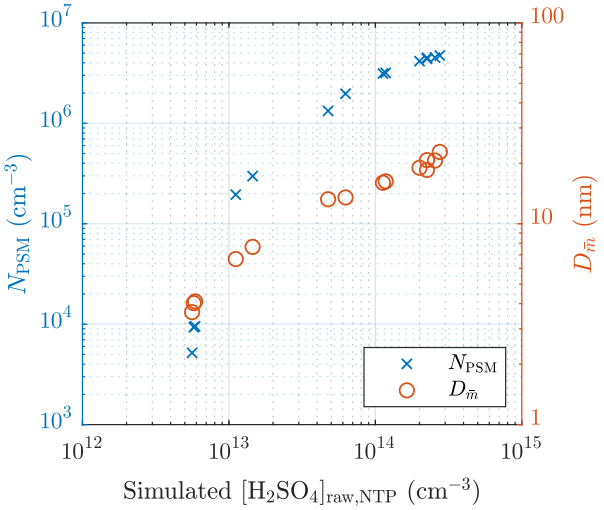

Figure 5. The measured number concentrations of the particles larger than $\sim$ 1.3 nm and the diameters with the average mass of the measurement set 1 as a function of the simulated H_2SO_4 concentration in the raw sample. The concentrations are multiplied with the total DR of the sampling system. The error bars for these values are shown later in Fig. 13.

The effect of humidity on the particle concentration (Set 2) is shown in Fig. 6. The slope of N_{PSM} versus $\mathrm{RH_{PTD}}$ in a log-log scale,

$$n_{N_{\mathrm{PSM}}\,\mathrm{vs.}\,\mathrm{RH_{PTD}}} = \frac{\partial \ln N_{\mathrm{PSM}}}{\partial \ln \mathrm{RH_{PTD}}}, \tag{5}$$

is roughly between 0.1 and 0.2. The slope $n_{N_{\mathrm{PSM}}\,\mathrm{vs.}\,\mathrm{RH_{PTD}}}$ nearly equals the slope of N_{PSM} versus $[\mathrm{H_2O}]_{\mathrm{PTD}}$ ($n_{N_{\mathrm{PSM}}\,\mathrm{vs.}\,[\mathrm{H_2O}]_{\mathrm{PTD}}}$) because T_{PTD} is nearly a constant. The slope $n_{N_{\mathrm{PSM}}\,\mathrm{vs.}\,[\mathrm{H_2O}]_{\mathrm{PTD}}}$ corresponds to the slope n_{w} with the same uncertainties as involved with the slopes $n_{N_{\mathrm{PSM}}\,\mathrm{vs.}\,[\mathrm{H_2SO_4}]_{\mathrm{raw}}}$ and n_{sa}. Nevertheless, the effect of decreased particle detection is not involved because, in this case, particle size has only a weak dependency of $\mathrm{RH_{PTD}}$. Additional uncertainty in estimating n_{w} arises from the origin of H_2O vapor in the system, which is both the dilution air and the raw sample. Because $[\mathrm{H_2O}]$ in the raw sample was kept constant, it has a higher effect on the total $[\mathrm{H_2O}]$ with lower values of $\mathrm{RH_{PTD}}$; thus, the estimated n_{w} is lower than the real n_{w} in the nucleation rate function.

The effect of T_{PTD} can be observed in Figs. 6 and 7. Lower temperatures result in higher concentrations of N_{PSM}. However, the examination is problematic because keeping $\mathrm{RH_{PTD}}$ as a constant while increasing T_{PTD} (Set 3a) increases $[\mathrm{H_2O}]$, which results in lower N_{PSM} with lower temperatures. Therefore, keeping $x_{\mathrm{w,PTD}}$ as a constant (Set 3b) is better in examining m_{sa}. One of the measurements with $T_{\mathrm{PTD}} = 50\,^{\circ}\mathrm{C}$ is, however, a significant outlier in Set 3b. Estimating the exponent m_{sa} from the slope in Fig. 7 is not straightforward because temperature is included also in the concentrations having yet unknown exponents.

The effect of the residence time on the particle concentrations is presented in Tab. 2. With $T_{\mathrm{sa}} = 135.5\,^{\circ}\mathrm{C}$ the ratio of N with the residence times of 1.4 s and with the residence time of 2.8 s is below unity, but above unity with higher temperatures. The

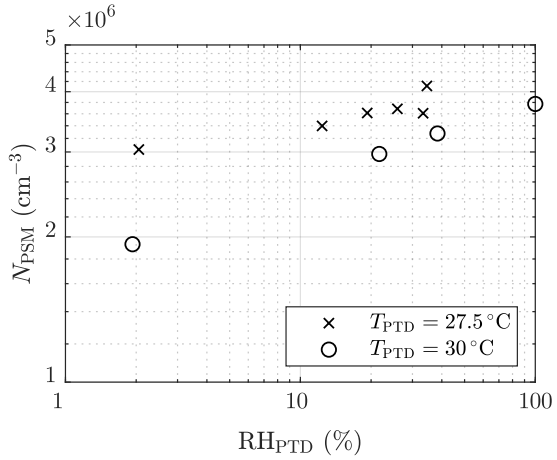

Figure 6. The measured number concentrations of the particles larger than $\sim$ 1.3 nm of the measurement set 2 as a function of the RH of the PTD dilution air. The concentrations are multiplied with the total DR of the sampling system. The error bars are within the marker sizes.

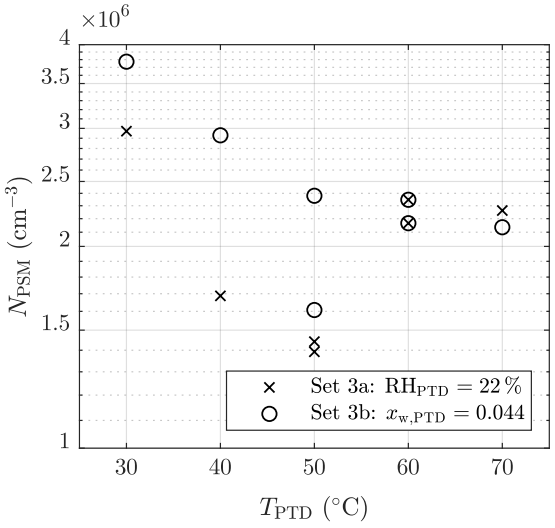

Figure 7. The measured number concentrations of the particles larger than $\sim$ 1.3 nm of the measurement set 3 as a function of the T of the PTD dilution air. The concentrations are multiplied with the total DR of the sampling system. The error bars are within the marker sizes.

ratio below unity denotes that the nucleation process is not diminished yet at the time of 1.4 s, e.g., the ratio of 0.74 denoting 74% of particles are formed within the time range of 0 ... 1.4 s and the remaining 26% within the time range of 1.4 ... 2.8 s. With higher temperatures the ratio is above unity because self-coagulation begins to decrease the number concentration, especially at the later times where the number concentration is the highest. The nucleation process may continue after 1.4 s but it cannot be easily seen with higher temperatures. Because coagulation has no effect on the mass concentrations (M), the ratios of M measured with the combination of the PSM, the CPC 3775, and the Nano-SMPS with the residence time of 1.4 s and with the residence time of 2.8 s are near unity with higher temperatures. The effect of particle growth and wall losses, however, have effects on the ratios too. The temperature with which the coagulation process would eliminate the effect of the nucleation process, resulting in the number concentration ratio of unity, is near 142 °C.

Table 2. The ratios of the measured number concentrations and mass concentrations with the residence times of 1.4 s and 2.8 s, in the measurement set 4. The values are corrected with the DR of the BD and with the diffusional losses in the sampling lines after the ED; thus, the values correspond with the distributions existing after the ED.

T_{sa} (°C)	$\frac{N(1.4\mathrm{s})}{N(2.8\mathrm{s})}$	$\frac{M(1.4\mathrm{s})}{M(2.8\mathrm{s})}$
135.5	0.74	0.28
150	1.29	0.92
160	1.72	0.96
164.5	1.74	1.10

4 Simulations

Every measurement point presented in Tab. 1 was simulated with the model consisting of four phases: (1) the CFD simulations to solve the flow and the temperature field of the sampling system, (2) the CFD-TUTMAM simulations to solve the aerosol processes in the sampling system, (3) correcting the particle sizes decreasing rapidly in the dry ED, and (4) calculating the penetration of the particles due to diffusional losses in the sampling lines after the sampling system and the detection efficiencies of the particle counting devices.

4.1 CFD model

The CFD simulations to solve the flow and the temperature fields for every simulation case were performed with a commercially available software ANSYS FLUENT 17.2. It is based on a finite volume method in which the computational domain is divided into a finite amount of cells. Governing equations of the flow are solved in every computational cell iteratively until sufficient convergence is reached. In this study, the governing equations in the first phase are continuity, momentum, energy, radiation, and turbulence transport equations.

The computational domain in the CFD simulations is an axial symmetric geometry consisting of the PTD, the aging chamber, and the ED (Fig. 1). An axial symmetric geometry was selected over a three-dimensional geometry due to high computational demand of the model and a nearly axial symmetric profile of the real measurement setup. The domain was divided into $\sim 8 \times 10^5$ computational cells, of which the major part was located inside the PTD where the smallest cells are needed due to the highest gradients. The smallest cells were 20 μm in side lengths and were located in the beginning of the porous section, where the hot exhaust and the cold dilution air meet.

In contrast to our previous study (Olin et al., 2015), the ED was also included in the computational domain though the ED has only a minor effect on nucleation (Lyyränen et al., 2004; Giechaskiel et al., 2009). Because the ED has a high speed nozzle that cools the flow locally to near -30 °C, including it in the domain provides partial validation for m_{sa} in the following way: if too high value for m_{sa} were used, nucleation would be observed in the ED, being in contradiction with the former studies. The internal fluid inside the sampling lines is modeled as a mixture of air, H_2O vapor, and H_2SO_4 vapor. The sampling lines are modeled as solid zones of steel or Tygon. 10 cm of the external fluid, modeled as air, is also included in the domain to simulate natural cooling of the sampling lines.

Flow rate and temperature boundary conditions for the simulated sampling system were set for the each simulation case to the measured values. Due to steady-state conditions and high computational demand, all governing equations were time-averaged; thus, the simulations were performed with a steady-state type. Turbulence was modeled using the SST-k-ω model, which is one of the turbulence models used with a steady-state simulation. It produced the most reliable results of the available steady-state turbulence models based on the pressure drop in the porous section. Turbulence, however, can have a significant role in the wall losses of the vapors and the particles in the regions where the turbulence level is high. In this sampling system, the turbulence level is high in the upstream part of the aging chamber where the diameter of the sampling line increases steeply. Validating the suitability of the turbulence model for this geometry would require a measurement of, e.g., solid seed particle concentrations after and before the sampling system without any aerosol processes, such as nucleation, condensation, and coagulation. However, that kind of measurement has not been performed yet.

4.2 CFD-TUTMAM

The main functionality of the CFD-TUTMAM based on the previous aerosol model, CFD-TUTEAM, is described by Olin et al. (2015). However, because the measured distributions are not in a log-normal form, the inclusion of the PL+LN model (Olin et al., 2016) was beneficial. The PL+LN model simulates the initial growth of newly-formed very small particles by modeling the particle size distribution with the combination of a power law (PL) and a log-normal (LN) distribution. Newly-formed particles are first put to the PL distribution, after which they are transferred to the LN distribution by particle growth.

The CFD-TUTMAM adds three governing equations per a distribution (denoted by j) to the CFD model using a modal representation of the particle size distribution, i.e. the distributions are modeled by three variables: number ($M_{j,0} = N_j$), surface area-related ($M_{j,2/3}$), and mass ($M_{j,1}$) moment concentrations. $M_{j,1}$ are further divided into different components in a multi-component system. Due to small particle size and low particle loading, the aerosol phase has only a minor effect on the gas phase properties. Therefore, continuity, momentum, energy, radiation, and turbulence transport equations can be excluded

from the computation after the flow and temperature fields are solved, and only gas species equations and the aerosol model equations are solved. The governing equation of the aerosol model for the concentration of a kth moment of a distribution j is

$$\frac{\partial M_{j,k}}{\partial t} = -\nabla\cdot(M_{j,k}\boldsymbol{u}) + \nabla\cdot\left(\rho_{\mathrm{f}}\overline{D}_{j,k,\mathrm{eff}}\nabla\frac{M_{j,k}}{\rho_{\mathrm{f}}}\right) + \mathrm{nucl}_{j,k} + \mathrm{cond}_{j,k} + \mathrm{coag}_{j,k} + \mathrm{transfer}_{j,k}, \tag{6}$$

where $\boldsymbol{u}$, ρ_{f}, and $\overline{D}_{j,k,\mathrm{eff}}$ are the fluid velocity vector, the fluid density, and the kth moment-weighted average of the particle effective diffusion coefficient, respectively. The last terms in Eq. (6) represent source terms for nucleation, condensation, coagulation, and intermodal particle transfer. In this study, aerosol is modeled with two distributions: a PL distribution ($j = \mathrm{PL}$) and a LN distribution ($j = \mathrm{LN}$). In this study, two gas species equations, which model the internal fluid mixture as the mass fractions of H_2O and H_2SO_4, are built in the CFD model, but the opposite numbers of the source terms of nucleation and condensation are added to them to maintain the mass closure of the species.

After each iteration step of the CFD-TUTMAM simulation, the parameters of the distributions are calculated for every computational cell by using the three moment concentrations. The parameters for the PL distribution are the number concentration (N_{PL}), the slope parameter (α), and the largest diameter (D_2). The smallest diameter (D_1) has a fixed value of 1.15 nm which is the smallest detectable particle diameter with the devices used. The density function for the PL distribution is

$$\left.\frac{\mathrm{d}N}{\mathrm{d}\ln D_{\mathrm{p}}}\right|_{\mathrm{PL}} = \begin{cases} N_{\mathrm{PL}}\left(\frac{D_{\mathrm{p}}}{D_2}\right)^{\alpha}\beta_0, & D_1 \le D_{\mathrm{p}} \le D_2 \\ 0, & \text{otherwise} \end{cases}, \tag{7}$$

where β_0 is a function

$$\beta_l\left(\alpha, \frac{D_1}{D_2}\right) = \begin{cases} \frac{\alpha+l}{1-\left(\frac{D_1}{D_2}\right)^{\alpha+l}}, & \alpha \neq -l \\ \frac{1}{-\ln\left(\frac{D_1}{D_2}\right)}, & \alpha = -l \end{cases}. \tag{8}$$

The parameters for the LN distribution are the number concentration (N_{LN}), the geometric standard deviation (σ), and the geometric mean diameter (D_{g}). An analytical solution exists for the reconstruction of the parameters from the moment concentrations for the LN distribution but not for the PL distribution; thus, it is solved numerically. A numerical solution is obtained by using the Levenberg-Marquardt iteration algorithm, in contrast to a slower method using a pre-calculated interpolation table described by Olin et al. (2016).

The nucleation source terms in Eq. (6) for different moments are

$$\begin{aligned} \mathrm{nucl}_{\mathrm{PL},0} &= J \\ \mathrm{nucl}_{\mathrm{PL},2/3} &= J\left(m^*_{\mathrm{sa}} + m^*_{\mathrm{w}}\right)^{2/3} \\ \mathrm{nucl}_{\mathrm{PL},1,\mathrm{sa}} &= J m^*_{\mathrm{sa}} \\ \mathrm{nucl}_{\mathrm{PL},1,\mathrm{w}} &= J m^*_{\mathrm{w}} \\ \mathrm{nucl}_{\mathrm{LN},k} &= 0, \end{aligned} \tag{9}$$

where J is the nucleation rate as in Eq. (2) and m_{sa}^* and m_{w}^* are the masses of H_2SO_4 and H_2O in a newly-formed particle. The value of $D_1 = 1.15\,\mathrm{nm}$ was chosen for the diameter of the newly-formed particles. A particle of this diameter is in equilibrium with water uptake in the temperature of 300 K and in the relative humidity of 22 % if the mass fraction of H_2SO_4 in the particle is 0.71. This constant value is used with nucleation though the mass fraction would vary between 0.5 and 1 if the whole temperature and humidity range were considered, but the major part of nucleation occurs in the conditions having the equilibrium mass fraction of near 0.71. This mass fraction and particle diameter corresponds to a cluster containing 5.7 H_2SO_4 molecules and 12.4 H_2O molecules.

Diffusion, condensation, and coagulation are modeled as described in the reference Olin et al. (2015) and intermodal particle transfer as described in the reference Olin et al. (2016). Condensation is modeled with the growth by H_2SO_4 from which immediately follows the water uptake until the water equilibrium is achieved. The water equilibrium procedure is also described in the reference Olin et al. (2015). The coagulation modeling includes intramodal coagulation within the both distribution and intermodal coagulation between the distributions.

Intermodal particle transfer includes condensational transfer and coagulational transfer from the PL distribution to the LN distribution. In contrast to a constant condensational transfer factor γ of the PL+LN model described in the reference Olin et al. (2016), a function of α, D_1/D_2, and k is used in the CFD-TUTMAM due to a more complex particle growth modeling. The function used here is

$$\gamma\left(\alpha, \frac{D_1}{D_2}, k\right) = \begin{cases} 0.1\alpha + 0.5, & \alpha \geq 0 \\ 0, & \alpha < 0 \end{cases} \times \begin{cases} \frac{3}{\beta_0}, & k = 0 \\ \frac{2}{\beta_1} + \frac{1}{\beta_2}, & k = \frac{2}{3} \\ \frac{3}{\beta_2}, & k = 1 \end{cases} . \tag{10}$$

The functional form of γ is derived so that the condensational transfer eliminates the effect of increasing α by the condensation process and also tries to keep α positive because a PL distribution with a negative α in combination with a LN distribution represents a distribution having a nonphysical local minimum between the distributions. The form of γ also restricts α increasing too high, which would cause numerical difficulties. Particles are not lost or altered during the intermodal particle transfer, it is only controlling the ratio of particles represented in the PL distribution and in the LN distribution. Higher values of γ result in lower N_{PL}/N ratio.

Deposition of particles and condensation of vapors onto the inner walls of the sampling lines have direct effect on the aerosol concentrations at the measurement devices. The particle deposition was modeled by setting the boundary conditions for the aerosol concentrations at the walls to zero, which represents deposition driven by diffusion and turbulence. Condensation of H_2O and H_2SO_4 vapors onto the walls was modeled by setting the boundary conditions for the mass fractions of H_2O and H_2SO_4 at the walls to saturation mass fractions in an aqueous solution of H_2SO_4, in contrast to the simpler method in the previous study (Olin et al., 2015). The simpler method caused H_2SO_4 to be completely non-condensing onto the walls

because the saturation ratio of the pure vapor never exceeded unity. Instead, the method using the saturation mass fractions in the solution induces some condensation because the vapor pressure of a hygroscopic liquid over an aqueous solution is lower than over a pure liquid. This method provides also smoother behavior of the boundary conditions on the walls. The method is, however, strongly dependent of the chosen activity coefficient functions of the vapors, which have large differences between each other due to their exponential nature. Activity coefficients used here are based on the values reported by Zeleznik (1991). However, due to exponential and non-monotonic nature of activity coefficients, they cause numerical difficulties in CFD modeling; thus, a monotonic van Laar type equation fitted by Taleb et al. (1996) from the data of Zeleznik (1991) was used.

4.3 Dry particle model

The main trend of the RH inside the sampling system is increasing due to decreasing temperature. This results in increasing water uptake rate during the particle growth process, which can be modeled by the condensation rate of H_2O that is simply the condensation rate of H_2SO_4 multiplied with a suitable factor (the water equilibrium procedure described by Olin et al. (2015)). However, when the sample enters to the ED, the RH decreases rapidly due to a dry dilution air, but the growth process by the condensation of H_2SO_4 still continues. This results in increasing H_2SO_4 amount in the particles but rapidly decreasing H_2O amount, which cannot be modeled with the water uptake model. Hence, the particles after the ED simulated by the CFD-TUTMAM contain incorrectly too much water.

All the simulated particle size distributions output by the CFD-TUTMAM were corrected to correspond the water amount that would be in the conditions after the ED ($T \approx 23\,^{\circ}\mathrm{C}$ and RH $\approx 3.6\,\%$). These conditions are mainly caused by the conditions of compressed air directed to the ED. Additionally, the particle size measurement device (Nano-SMPS) used room air, having nearly equal conditions as compressed air, as the sheath flow air. Dry sheath flow air also dries particles rapidly inside the device. The theory behind the dry particle model equals the theory behind the water uptake model in the CFD-TUTMAM, but the drying process is significantly faster and in opposite direction, in contrast to the water uptake connected to the condensation rate of H_2SO_4 in the CFD-TUTMAM. Figure 8 represents examples of particle diameters in different humidities, e.g., a particle with the diameter of 40 nm in the RH of 60 % shrinks to the diameter of 30 nm when sampled with the ED.

4.4 Penetration and detection efficiency model

Particle size distributions output by the CFD-TUTMAM and corrected with the dry particle model were also corrected according to the penetration and detection efficiency model. Particle penetration in the sampling lines between the ED and the measurement devices were calculated with the equations of Gormley and Kennedy (1948). All the internal diameters of the used sampling lines were sufficiently large to keep the flows laminar to minimize the diffusional losses. The penetration-corrected size distributions were multiplied with the detection efficiency curves presented in Fig. 2 to simulate the measured number concentrations by the PSM and the CPC 3775 and the measured size distribution by the Nano-SMPS.

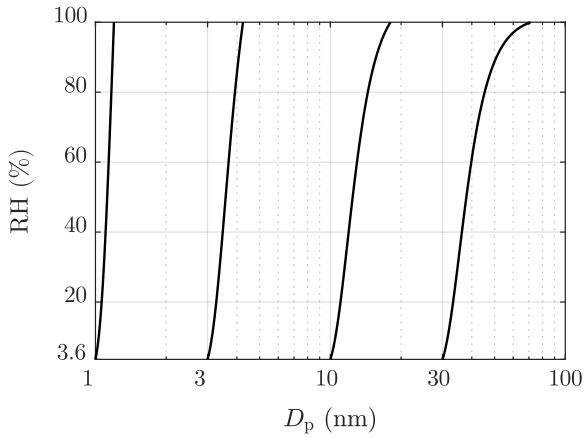

Figure 8. Examples of particle diameters in different humidities in the temperature of 23 °C. The lowest RH value represents the RH of the dilution air of the ED.

4.5 Inverse modeling

The simulated number concentrations measurable by the PSM with different saturator flow rates and by the CPC 3775 and the simulated size distributions measurable by the Nano-SMPS were compared with the measured ones during inverse modeling. The exponents n_{sa}, n_{w}, and m_{sa} were altered until the simulated and the measured variables corresponded satisfactorily in all simulated cases. The proportionality coefficient k in Eq. (2) is unknown and depends on the exponents. Because the value of k affects directly on the nucleation rate magnitude, it was obtained by fitting until the simulated and the measured number concentrations corresponded.

Due to the uncertainties involved in the measurement of $[\mathrm{H_2SO_4}]_{\mathrm{raw}}$ (see the Supplement), the boundary conditions for $[\mathrm{H_2SO_4}]$ in the CFD-TUTMAM simulations could not be set initially. Hence, $[\mathrm{H_2SO_4}]_{\mathrm{raw}}$ was considered a fitting parameter also. It was estimated by comparing the aerosol mass concentrations because it has a direct effect on the particle sizes, but affects also on J. Inverse modeling of the vapor concentrations is possible due to the condensational growth of particles. In conclusion, the inverse modeling requires fitting all the five parameters (n_{sa}, n_{w}, m_{sa}, k, and $[\mathrm{H_2SO_4}]_{\mathrm{raw}}$) to obtain the function for J. The first four parameters were fitted in a way they have the same value for every simulation case, but the last parameter, $[\mathrm{H_2SO_4}]_{\mathrm{raw}}$, was fitted in every simulation case separately. In the simulations related to the measurement sets 2 ... 4, T_{sa} was not altered between the measurement points; therefore, the value of $[\mathrm{H_2SO_4}]_{\mathrm{raw}}$ in the simulations was constant. Because only one parameter was fitted separately, only one of the outputs, the aerosol number or mass concentration, could correspond with the measured value exactly. In this study, the number concentration was chosen as the main output of which correspondence is preferred over the correspondence of the mass concentration because nucleation process is connected more straightly to the number concentration.

The uncertainties involved in modeling turbulence and the condensation of the vapors onto the walls affect the number and mass concentrations in the measurement devices. Nevertheless, these uncertainties become partially insignificant because k and $[\mathrm{H_2SO_4}]_{\mathrm{raw}}$ are considered fitting parameters, which partially neglect uncertainly modeled losses of particles and vapors.

5 Simulation results

In this section, the outputs of the simulations performed using the nucleation rate function with the best correspondence between the measured and the simulated data are described firstly. Finally, the used nucleation rate function is presented.

5.1 Sulfuric acid concentrations

Figure 9 represents the comparison of the inversely modeled $[\mathrm{H_2SO_4}]_{\mathrm{raw}}$ with the theoretical concentrations. The simulated concentrations vary between 0.05 and 0.57 times the theoretical concentrations where the lowest values are observed with lower T_{sa} values probably due to the effect of increasingly saturating $\mathrm{H_2SO_4}$ liquid onto the sampling lines with higher temperatures that can decrease the diffusional losses onto the sampling lines. All values lie between the theoretical level assuming full diffusional losses and the lossless theoretical level. A weak agreement of the simulated concentrations with 0.15 times the theoretical curve can be seen, which implies the diffusional losses of 85 % onto the sampling lines between the $\mathrm{H_2SO_4}$ evaporator and the PTD. Results and involved challenges of the additional $[\mathrm{H_2SO_4}]_{\mathrm{raw}}$ measurements are presented in the Supplement.

5.2 Particle size distributions

Examples of measured and simulated particle concentrations and size distributions of the measurement set 1 are presented in Fig. 10. The panes (a) and (c) in the figure represent the concentrations measured/measurable with the PSM and the CPC 3775. Because the concentrations decrease with increasing cut diameter in the case with $T_{\mathrm{sa}} = 102\,^{\circ}\mathrm{C}$ (a), particle size distribution exists within this diameter range, which is also seen in the simulated data. However, the concentration measured with the cut diameter of 3.1 nm is two-fold compared to the simulated one, implying that the real distribution is not a pure PL+LN distribution or the shape of the distribution is modeled incorrectly near the diameter of 3.1 nm. Conversely, in the case with $T_{\mathrm{sa}} = 157.2\,^{\circ}\mathrm{C}$ (c), the concentrations are in the same level, which implies no size distribution within that diameter range.

The panes (b) and (d) in Fig. 10 represent examples of measured and simulated Nano-SMPS data. The case with $T_{\mathrm{sa}} = 102\,^{\circ}\mathrm{C}$, (b) represent an example of one of the worst agreements of measured and simulated size distributions. While the simulated total number concentration agrees with the measured one in that case, the particle diameter is underestimated with the factor of ~ 1.6. The disagreement is discussed later in this section. Conversely, in the case with $T_{\mathrm{sa}} = 157.2\,^{\circ}\mathrm{C}$ (d), the distributions agree well, except that the model predicts higher particle concentration in the diameter range of 2.5 ... 7 nm. This disagreement can be due to lower particle detection efficiency of the Nano-SMPS than is included in the inversion algorithm of the device (see the Supplement). This is not included in the penetration and detection efficiency model and is thus not seen in the simulated distributions. Because the detection efficiency curve of the CPC 3776 is included in the model, the simulated size

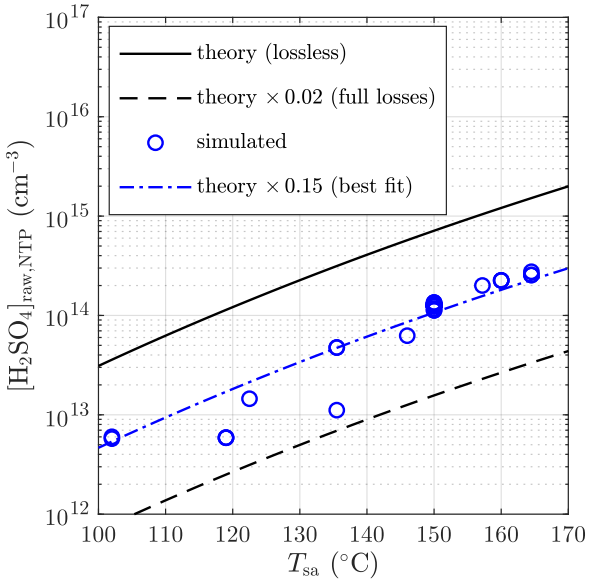

Figure 9. Simulated sulfuric acid concentrations in the raw sample compared to the theoretical concentrations with different sulfuric acid evaporator temperatures. The concentrations are presented as the concentrations in NTP conditions rather than in a hot raw sample.

distributions measurable with the Nano-SMPS decrease steeply with decreasing particle diameter near the particle diameter of $D_{50} = 3.4\,\mathrm{nm}$. The sharp peak at the diameter of $\sim$ 20 nm in the simulated distribution in (d) is caused by the nature of the PL+LN model where the PL distribution ends at the diameter of $D_2 \approx 20\,\mathrm{nm}$. While Fig. 10 represents the data at the measurement devices, Fig. 11 represents the example distributions after the ED. From the latter figure the PL distribution is seen as a whole, starting from the diameter of $D_1 = 1.15\,\mathrm{nm}$.

The requirement of the PL+LN model can be observed from Fig. 12, in which the particle number concentrations and sizes of a single simulation case with different values of $[H_2SO_4]_{raw}$ are presented. With low values of $[H_2SO_4]_{raw}$, both N and $D_{\bar{m}}$ behave discontinuously if only the LN distribution is simulated: particles are first small and in low concentration when $[H_2SO_4]_{raw}$ increases, and then suddenly rise to higher levels. This is, however, not seen with the PL+LN model, which has a smoother behavior. Therefore, by simulating with the LN distribution only, it is impossible to produce, e.g., a size distribution with $N = 10^4\,\mathrm{cm}^{-3}$ or $D_{\bar{m}} = 3\,\mathrm{nm}$ with this simulation setup, whereas with the PL+LN model it is possible.

5.3 Particle concentrations and sizes

Figure 13 represents the comparison of the simulated and the measured N_{PSM} and $D_{\bar{m}}$ values after the ED. The black dots in the pane (a) correspond well with the measured concentrations because they represent the cases for which N_{PSM} was obtained by fitting the value of $[H_2SO_4]_{raw}$. The red dots deviate more from the 1:1 line because they represent all the other cases, the N_{PSM}

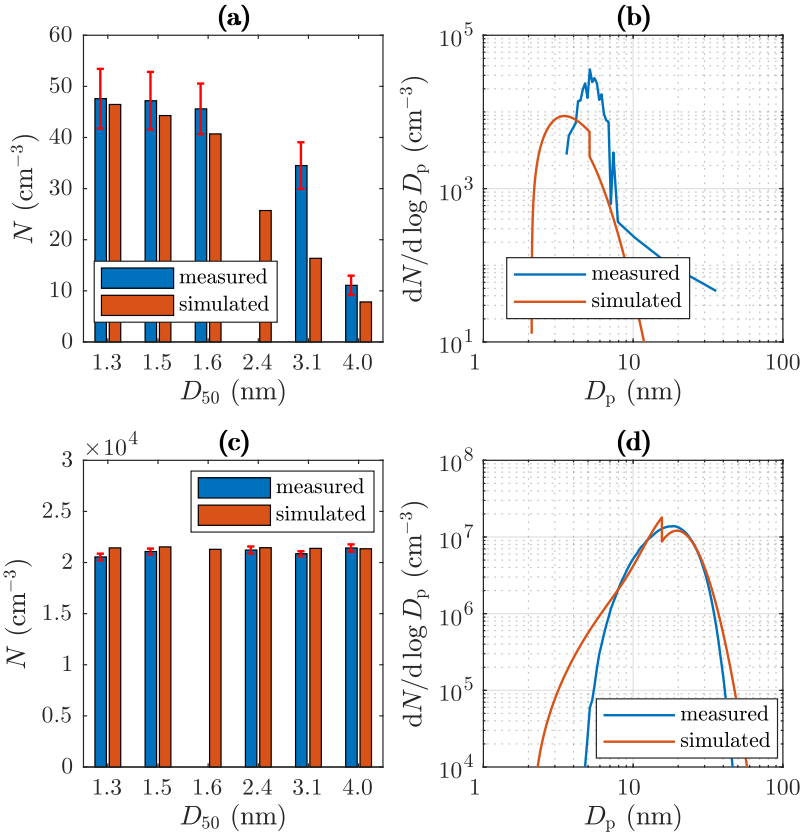

Figure 10. Examples of measured and simulated (a) number concentrations from the PSM and the CPC 3775 with $T_\mathrm{sa} = 102\,^\circ$C, (b) size distributions from the Nano-SMPS with $T_\mathrm{sa} = 102\,^\circ$C, (c) number concentrations from the PSM and the CPC 3775 with $T_\mathrm{sa} = 157.2\,^\circ$C, and (d) size distributions from the Nano-SMPS with $T_\mathrm{sa} = 157.2\,^\circ$C. The D_{50} values in the range of $1.3 \ldots 3.1$ nm represent the cut-sizes of the PSM with different saturator flow rates and the D_{50} value of 4.0 nm represents the cut-size of the CPC 3775. The error bars in the measured concentrations represent the standard deviations and are caused by instability in the particle generation.

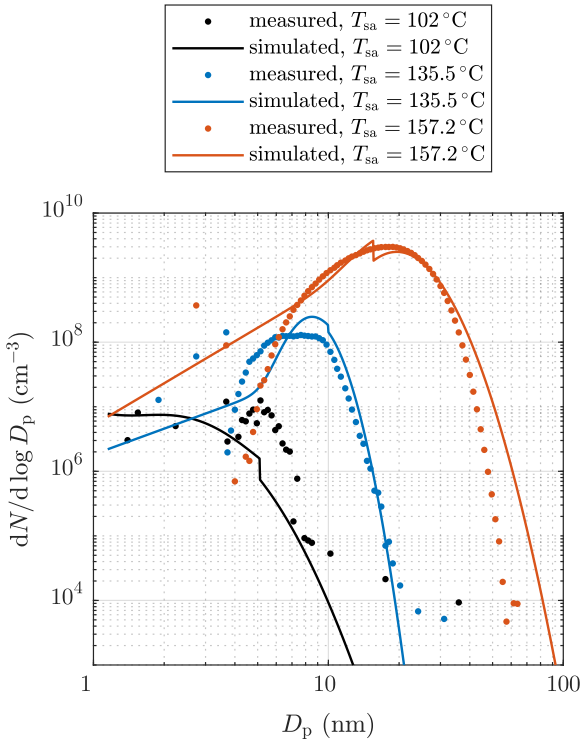

Figure 11. Examples of measured and simulated particle size distributions after the ED. The measured data are corrected with the DR of the BD and with the diffusional losses in the sampling lines after the ED. Additionally, all concentrations are multiplied with the total DR of the diluting sampling system. See the Supplement for error bars.

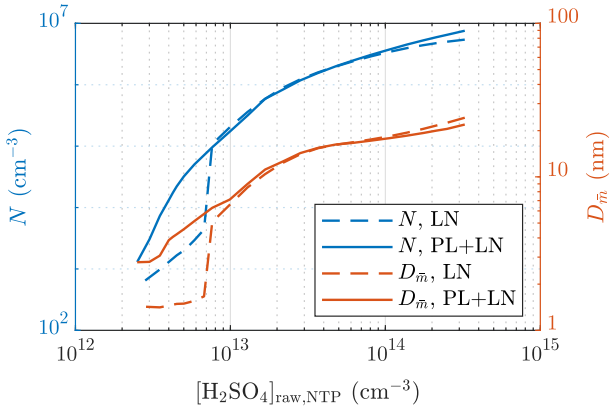

Figure 12. Comparison of the particle number concentrations and the diameters with the average mass after the ED simulated using the LN distribution only and using both the PL and the LN distributions.

values of which originate from the simulations, e.g., simulated with different RH_{PTD}, T_{PTD}, or residence times. Nevertheless, all the simulated N_{PSM} values correspond with the measured values relatively well. The optimal scenario would be that all the N_{PSM} values would correspond exactly with the measured values, but that would imply the exponents n_w and m_{sa} in the nucleation rate function can be modeled exactly with constant values within the concentration and temperature ranges of this study. However, it is not expected that the constant exponents would represent exactly the nucleation rate function in all concentration and temperature ranges.

The black dots in the pane (b) of Fig. 13 correspond moderately with the measured $D_{\bar{m}}$ values. It can be observed that the points do not lie on a straight 1:1 line perfectly, instead they form a slightly curved line, on which simulated particle sizes are overestimated near 10 nm but underestimated in small particle sizes. There are several issues which can cause this discrepancy: (1) the exponent n_{sa} varies with $[H_2SO_4]$, (2) a problem in calculating $D_{\bar{m}}$ from the measurement data, (3) a problem in estimating a proper N_{PL}/N ratio in the PL+LN model, and (4) an uncertainty in simulating the condensation process. The most possible explanation is (1) because according to the CNT, n_{sa} decreases with increasing $[H_2SO_4]$. This can be seen as overestimated particle sizes in mid-ranged particle sizes because smaller particle sizes would require lower $[H_2SO_4]_{raw}$ but that would cause underestimated N_{PSM}. To overcome the underestimated N_{PSM} in mid-ranged $[H_2SO_4]$ values, k should be increased in mid-ranged $[H_2SO_4]$ values, which indicates decreasing n_{sa} with increasing $[H_2SO_4]$. The point (2) can explain at least the discrepancy of the lower values of $D_{\bar{m}}$ because calculating $D_{\bar{m}}$ from the measured PSM, CPC 3775, and Nano-SMPS data is not straightforward, especially with the lower values of $D_{\bar{m}}$ in which the distributions measured by the Nano-SMPS are cut from the smaller diameter edge due to very low detection efficiency. Therefore, $D_{\bar{m}}$ calculated from the measurement data may be overestimated with the lower values of $D_{\bar{m}}$. This is also seen as long error bars towards left, especially for $D_{\bar{m}}$ values smaller than 10 nm (see the Supplement for details). However, by comparing the measured and the simulated size distributions with $T_{sa} = 102\,°C$ in Fig. 11 (measured $D_{\bar{m}} = 3.6\,nm$, simulated $D_{\bar{m}} = 2.8\,nm$), it can be seen that the larger diameter edges of the distribution do not correspond satisfactorily either, which implies (1) being the most possible explanation. Conversely, the discrepancy of the higher values of $D_{\bar{m}}$ can be partially explained by (3) because simulating those cases with the LN distribution only, even higher values of $D_{\bar{m}}$ are output. That implies the PL+LN model underestimates the N_{PL}/N ratio. The N_{PL}/N ratio is controlled by the value of γ, the proper functional form of which is still under development in the PL+LN model. The last point (4) can also explain the discrepancies but the direction of a discrepancy could be in one way or another. The red dots follow mainly the same curve as the black dots with the exception of four cases in which the values of $D_{\bar{m}}$ are clearly overestimated. These cases belong to the measurement set 3 and have high T_{PTD}. This discrepancy raises the point (4) because there are clearly some uncertainties involved in the condensation process modeling when T_{PTD} is high. It can be related, e.g., to the activity coefficient function of H_2SO_4 because too low activity coefficient would cause too low vapor pressure of H_2SO_4 at the surface of a particle, which would cause too large particles.

Table 3 represents the ratios of the simulated N and M with the residence times of 1.4 s and 2.8 s. The simulated ratios follow the same behavior as the measured ratios: with a low T_{sa} value the ratios are below unity and with higher T_{sa} values the ratio of N increases but the ratio of M stays near unity. The ratios with a low T_{sa} value correspond well with the measured values, but according to the simulations, the ratio of N does not increase with increasing T_{sa} equally with the measured ratios.

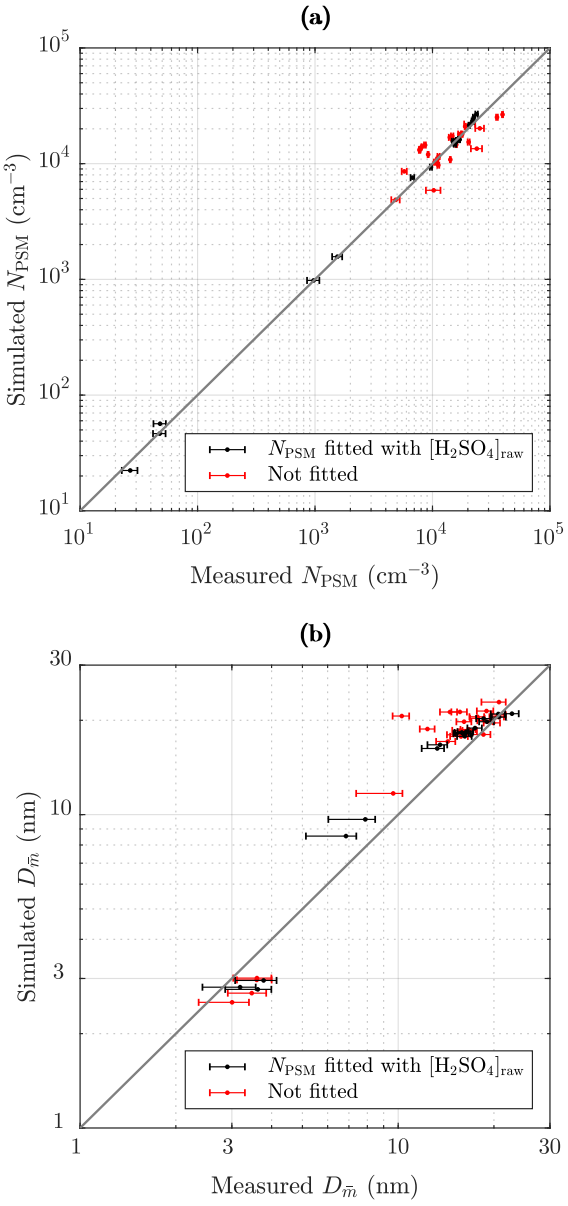

Figure 13. Comparison of the simulated and the measured (a) number concentrations of the particles larger than $\sim$ 1.3 nm and (b) the diameters with the average mass after the ED. The black dots represent the cases for which N_{PSM} and $D_{\bar{m}}$ were obtained by fitting the value of $[\mathrm{H_2SO_4}]_{\mathrm{raw}}$. The red dots represent the cases of the measurement sets 2 ... 4 in which the values of $[\mathrm{H_2SO_4}]_{\mathrm{raw}}$ originated from an another case of the measurement set having the same T_{sa} value. The error bars in the pane (a) represent the standard deviations in concentration measurements, and the calculation of the error bars in the pane (b) is described in the Supplement.

This implies the coagulation rate is underestimated in the model but the reason for that is unknown. The temperature with which the coagulation process would eliminate the effect of the nucleation process, resulting in the number concentration ratio of unity, is near 148 °C (near 142 °C according to the measurements).

Table 3. The ratios of the simulated number concentrations and mass concentrations after the ED with the residence times of 1.4 s and 2.8 s, in the measurement set 4. The values in parentheses denote the measured values as presented in Tab. 2.

T_{sa} (°C)	$\frac{N(1.4\,\mathrm{s})}{N(2.8\,\mathrm{s})}$	$\frac{M(1.4\,\mathrm{s})}{M(2.8\,\mathrm{s})}$
135.5	0.66 (0.74)	0.25 (0.28)
150	1.04 (1.29)	0.88 (0.92)
160	1.07 (1.72)	0.99 (0.96)
164.5	1.06 (1.74)	0.96 (1.10)

5.4 Nucleation rate function

The nucleation rate function with the best correspondence between the measured and the simulated data having a type of Eq. (2) used in the simulations has the parameters presented in Tab. 4 and is thus

$$J\left([\mathrm{H_2SO_4}],[\mathrm{H_2O}],T\right) = 5.8\times10^{-26}\,\frac{[\mathrm{H_2SO_4}]^{1.9}[\mathrm{H_2O}]^{0.5}}{{p_{\mathrm{sa}}}^{\circ}(T)^{0.75}}, \tag{11}$$

where the concentrations are given in cm^{-3}, the saturation vapor pressure in Pa, and the nucleation rate is output in cm^{-3}. This function was applied within the environmental parameter ranges presented in Tab. 5. The ranges can be considered the ranges within which Eq. (11) is defined. However, because the major part of the nucleation occurs when $[\mathrm{H_2SO_4}]$ is high (nearer to the upper boundary than to the lower boundary), a wrong formulation of J in the $[\mathrm{H_2SO_4}]$ values lower than $2\times10^{11}\ \mathrm{cm}^{-3}$ would have only a minor effect on the model outputs. Therefore, an alternative range having $2\times10^{11}\ \mathrm{cm}^{-3}$ as a minimum boundary for $[\mathrm{H_2SO_4}]$ is a more credible range within which the obtained function for J produces reliable results.

Table 4. The parameters of the nucleation rate function with the best correspondence between the measured and the simulated data. The ranges of variation represent the resolution with which the exponents were altered during inverse modeling.

Parameter	Value
k	5.8×10^{-26}
n_{sa}	$1.9\,(\pm0.1)$
n_{w}	$0.50\,(\pm0.05)$
m_{sa}	$0.75\,(\pm0.05)$

Table 5. The environmental parameter ranges within which the nucleation rate function was applied.

Parameter	Unit	Lower boundary	Upper boundary
T	°C	-30	250
$[H_2SO_4]$	cm^{-3}	0 (2×10^{11})[a]	2×10^{14}
x_{sa}		0 (10^{-8})[a]	1.1×10^{-5}
$[H_2O]$	cm^{-3}	2×10^{16}	10^{18}
x_w		8×10^{-4}	0.04
RH	%	0.1	100

[a] Alternative range

Because $p_{sa}{}^{\circ}(T)$ has nearly equal exponential form with the saturation vapor pressure of H_2O ($p_w{}^{\circ}(T)$), $p_{sa}{}^{\circ}(T)$ can be expressed approximately using $p_w{}^{\circ}(T)$ with

$$p_{sa}{}^{\circ}(T) \approx 2.6 \times 10^{-10} p_w{}^{\circ}(T)^2. \tag{12}$$

Hence, the magnitude of J remains as in Eq. (11) if it is expressed with $p_w{}^{\circ}(T)$ using the form

$$J([H_2SO_4],[H_2O],T) = 8.9 \times 10^{-19} \frac{[H_2SO_4]^{1.9}[H_2O]^{0.5}}{p_w{}^{\circ}(T)^{1.5}} \tag{13}$$

or with both $p_{sa}{}^{\circ}(T)$ and $p_w{}^{\circ}(T)$ using, e.g., the form

$$J([H_2SO_4],[H_2O],T) = 1.4 \times 10^{-23} \frac{[H_2SO_4]^{1.9}[H_2O]^{0.5}}{p_{sa}{}^{\circ}(T)^{0.5}\, p_w{}^{\circ}(T)^{0.5}} \tag{14}$$

or a different form

$$J([H_2SO_4],[H_2O],T) = 4.0 \times 10^{-25} \left(\frac{[H_2SO_4]}{p_{sa}{}^{\circ}(T)^{0.35}}\right)^{1.9} \left(\frac{[H_2O]}{p_w{}^{\circ}(T)^{0.35}}\right)^{0.5}. \tag{15}$$

The exponent $n_{sa} = 1.9$ is in agreement with the former nucleation studies related to vehicle exhaust (Vouitsis et al., 2005) or to the atmosphere (Sihto et al., 2006; Riipinen et al., 2007; Brus et al., 2011; Riccobono et al., 2014) where n_{sa} lies usually between 1 and 2. The exponent $n_{sa} = 1.9$ corresponds best with the kinetic nucleation theory (McMurry and Friedlander, 1979) where $n_{sa} = 2$. Estimating n_{sa} from the measured particle number concentration provided the slope $n_{N_{PSM} \text{ vs. } [H_2SO_4]} = 0.4 \ldots 10$. The exponent n_w estimated from the measurement data is $n_{N_{PSM} \text{ vs. } RH_{PTD}} = 0.1 \ldots 0.2$, which is remarkably lower than the inversely modeled exponent $n_w = 0.5$. The slope of N_{PSM} versus T_{PTD} of the measurement set 3b in Fig. 7 is

$$n_{N_{PSM} \text{ vs. } T_{PTD}} = \frac{\partial \ln N_{PSM}}{\partial \ln T_{PTD}} = -6 \ldots -4 \tag{16}$$

but the inversely modeled exponent $m_{sa} = 0.75$ corresponds to the slope of -27, which is remarkably more negative than $n_{N_{PSM} \text{ vs. } T_{PTD}}$ due to the same uncertainties as involved with the slopes $n_{N_{PSM} \text{ vs. } [H_2SO_4]}$ and $n_{N_{PSM} \text{ vs. } RH_{PTD}}$. In conclusion, inverse modeling provides significantly more accurately the exponents over the method based on the measurement data only.

Nucleation rate was the highest in the PTD where the hot sample and the cold dilution air met. The major part of nucleation occurred in the beginning part of the aging chamber. No noticeable nucleation occurred in the ED though temperature reaches $-30\,^{\circ}\mathrm{C}$ locally, which is in agreement with the former studies. It provides partial validation for the obtained m_{sa} value.

6 Conclusions

Homogeneous $\mathrm{H_2SO_4}$-$\mathrm{H_2O}$ nucleation rate measurements using the modified partial flow sampling system mimicking the dilution process occurring in a real-world driving situation were performed. The aerosol formed in the diluting and cooling sampling system was measured using the PSM, the CPC 3775, and the Nano-SMPS. The particle size distribution near the detection limit of the Nano-SMPS showed clear disagreement with the PSM and the CPC3775 data, with major underestimation of the smaller particles and distortion of the size distribution shape due to the limitations involved in detecting small particles with simultaneous nucleation and particle growth using the Nano-SMPS. Thus, the data without the PSM and the CPC 3775 would unrealistically suggest log-normal shape for the size distributions.

The measurements were simulated with the aerosol dynamics code CFD-TUTMAM using nucleation rate which is explicitly defined as a function of temperature and the concentrations of $\mathrm{H_2SO_4}$ and $\mathrm{H_2O}$. Equation (2) was used as the functional form of nucleation rate. The parameters for Eq. (2) which resulted in the best prediction for particle number concentrations and size distributions were $n_{\mathrm{sa}} = 1.9$, $n_{\mathrm{w}} = 0.5$, and $m_{\mathrm{sa}} = 0.75$, thus providing the nucleation rate function Eq. (11) (or any of Eqs. (13) – (15)). As discussed in Sec. 5.3, the obtained exponent $n_{\mathrm{sa}} = 1.9$ may be slightly overestimated in high concentrations and slightly underestimated in low concentrations. Estimating these exponents using only the measured particle concentrations resulted in markedly higher uncertainties when compared to modeling them inversely using the CFD-TUTMAM code.

The raw sample was generated by evaporating $\mathrm{H_2SO_4}$ and $\mathrm{H_2O}$ liquids. The concentration of $\mathrm{H_2SO_4}$ was controlled by adjusting the temperature of the liquid, T_{sa}. The boundary condition for $\mathrm{H_2SO_4}$ concentration, $[\mathrm{H_2SO_4}]_{\mathrm{raw}}$, was handled as a fitting parameter to correspond the simulated size distributions with the measured ones. Particle sizes were small with low T_{sa} and the size distributions were not in a log-normal form. Therefore, using the PL+LN model to represent the size distributions in the CFD-TUTMAM was necessary.

In these measurements, particle formation was not observed with the $\mathrm{H_2SO_4}$ concentrations below $5.7\times10^{12}\,\mathrm{cm^{-3}}$ at exhaust condition temperatures. However, with real vehicle exhaust, in the same sampling system used here, particle formation has been observed even with the concentration of $2.5\times10^{9}\,\mathrm{cm^{-3}}$ (Arnold et al., 2012). This indicates that the nucleation rate of the binary $\mathrm{H_2SO_4}$-$\mathrm{H_2O}$ nucleation mechanism is lower than the nucleation rate in real exhaust. Therefore, the binary $\mathrm{H_2SO_4}$-$\mathrm{H_2O}$ nucleation cannot be fully controlling the particle formation process; instead, other compounds, such as hydrocarbons, existing in real exhaust are likely to be involved in the process as well, which is in agreement with the former exhaust-related nucleation studies (Saito et al., 2002; Vaaraslahti et al., 2004; Meyer and Ristovski, 2007; Pirjola et al., 2015; Olin et al., 2015).

The obtained exponent $n_{\mathrm{sa}} = 1.9$ is in agreement with the former nucleation studies related to the atmosphere or vehicle exhaust ($n_{\mathrm{sa}} = 1 \ldots 2$) and corresponds best with the kinetic nucleation theory. However, the effects of $[\mathrm{H_2O}]$ and T obtained here may differ from the former studies because the effects are not extensively studied in them. The functional form and

especially the values of the nucleation exponents for the homogeneous H_2SO_4-H_2O nucleation rate obtained in this study helps in finding the currently unknown nucleation mechanism occurring in real vehicle or power plant boiler exhaust or in the atmosphere. It provides also the starting point for inverse modeling studies purposed to examine hydrocarbon-involved H_2SO_4-H_2O nucleation mechanism, which is likely occurred in real vehicle exhaust. It can also be used to improve air quality models by using it to model the effect of H_2SO_4-emitting traffic and power generation on the particle concentration in urban air.

Author contributions. M.O., J.A., T.R., and M.D.M. designed the experiments and M.O. and J.A. carried them out. M.O. analyzed the measurement data, developed the model code, and performed the simulations. M.R.T.P. designed the IC analysis. M.O. prepared the manuscript with contributions from all co-authors.

Competing interests. The authors declare that they have no conflict of interest.

Acknowledgements. This work was funded by Tampere University of Technology Graduate School and by the Maj and Tor Nessling Foundation (project number 2014452). The authors thank CSC and TCSC for the computational time. We also thank prof. Mikko Sipilä from University of Helsinki for lending the CI-inlet for the APi-TOF, the tofTools team for providing tools for mass spectrometry analysis, and M.Sc. Kalle Koivuniemi for Ion Chromatography measurements.

References

Alanen, J., Saukko, E., Lehtoranta, K., Murtonen, T., Timonen, H., Hillamo, R., Karjalainen, P., Kuuluvainen, H., Harra, J., Keskinen, J., and Rönkkö, T.: The formation and physical properties of the particle emissions from a natural gas engine, Fuel, 162, 155–161, https://doi.org/10.1016/j.fuel.2015.09.003, 2015.

Albriet, B., Sartelet, K., Lacour, S., Carissimo, B., and Seigneur, C.: Modelling aerosol number distributions from a vehicle exhaust with an aerosol CFD model, Atmos. Environ., 44, 1126–1137, https://doi.org/10.1016/j.atmosenv.2009.11.025, 2010.

Alföldy, B., Giechaskiel, B., Hofmann, W., and Drossinos, Y.: Size-distribution dependent lung deposition of diesel exhaust particles, J. Aerosol Sci., 40, 652–663, https://doi.org/10.1016/j.jaerosci.2009.04.009, 2009.

Arneth, A., Unger, N., Kulmala, M., and Andreae, M.: Clean the air, heat the planet?, Science, 326, 672–673, https://doi.org/10.1126/science.1181568, 2009.

Arnold, F., Pirjola, L., Rönkkö, T., Reichl, U., Schlager, H., Lähde, T., Heikkilä, J., and Keskinen, J.: First online measurements of sulfuric acid gas in modern heavy-duty diesel engine exhaust: Implications for nanoparticle formation, Environ. Sci. Technol., 46, 11 227–11 234, https://doi.org/10.1021/es302432s, 2012.

Beelen, R., Raaschou-Nielsen, O., Stafoggia, M., Andersen, Z., Weinmayr, G., Hoffmann, B., Wolf, K., Samoli, E., Fischer, P., Nieuwenhuijsen, M., Vineis, P., Xun, W., Katsouyanni, K., Dimakopoulou, K., Oudin, A., Forsberg, B., Modig, L., Havulinna, A., Lanki, T., Turunen, A., Oftedal, B., Nystad, W., Nafstad, P., De Faire, U., Pedersen, N., Östenson, C.-G., Fratiglioni, L., Penell, J., Korek, M., Pershagen, G., Eriksen, K., Overvad, K., Ellermann, T., Eeftens, M., Peeters, P., Meliefste, K., Wang, M., Bueno-De-Mesquita, B., Sugiri, D., Krämer, U., Heinrich, J., De Hoogh, K., Key, T., Peters, A., Hampel, R., Concin, H., Nagel, G., Ineichen, A., Schaffner, E., Probst-Hensch, N., Künzli, N., Schindler, C., Schikowski, T., Adam, M., Phuleria, H., Vilier, A., Clavel-Chapelon, F., Declercq, C., Grioni, S., Krogh, V., Tsai, M.-Y., Ricceri, F., Sacerdote, C., Galassi, C., Migliore, E., Ranzi, A., Cesaroni, G., Badaloni, C., Forastiere, F., Tamayo, I., Amiano, P., Dorronsoro, M., Katsoulis, M., Trichopoulou, A., Brunekreef, B., and Hoek, G.: Effects of long-term exposure to air pollution on natural-cause mortality: An analysis of 22 European cohorts within the multicentre ESCAPE project, Lancet, 383, 785–795, https://doi.org/10.1016/S0140-6736(13)62158-3, 2014.

Boucher, O., Randall, D., Artaxo, P., Bretherton, C., Feingold, G., Forster, P., Kerminen, V.-M., Kondo, Y., Liao, H., Lohmann, U., Rasch, P., Satheesh, S., Sherwood, S., Stevens, B., and Zhang, X.: Clouds and Aerosols, book section 7, p. 571–658, Cambridge University Press, Cambridge, United Kingdom and New York, NY, USA, https://doi.org/10.1017/CBO9781107415324.016, 2013.

Boulaud, D., Madelaine, G., Vigla, D., and Bricard, J.: Experimental study on the nucleation of water vapor sulfuric acid binary system, J. Chem. Phys., 66, 4854–4860, https://doi.org/10.1063/1.433823, 1977.

Brus, D., Neitola, K., Hyvärinen, A.-P., Petäjä, T., Vanhanen, J., Sipilä, M., Paasonen, P., Kulmala, M., and Lihavainen, H.: Homogenous nucleation of sulfuric acid and water at close to atmospherically relevant conditions, Atmos. Chem. Phys., 11, 5277–5287, https://doi.org/10.5194/acp-11-5277-2011, 2011.

Chen, L., Liang, Z., Zhang, X., and Shuai, S.: Characterizing particulate matter emissions from GDI and PFI vehicles under transient and cold start conditions, Fuel, 189, 131 – 140, https://doi.org/10.1016/j.fuel.2016.10.055, 2017.

Dockery, D., Pope III, C., Xu, X., Spengler, J., Ware, J., Fay, M., Ferris Jr., B., and Speizer, F.: An association between air pollution and mortality in six U.S. cities, New Engl. J. Med., 329, 1753–1759, https://doi.org/10.1056/NEJM199312093292401, 1993.

Giechaskiel, B., Ntziachristos, L., and Samaras, Z.: Effect of ejector dilutors on measurements of automotive exhaust gas aerosol size distributions, Meas. Sci. Technol., 20, 045 703, https://doi.org/10.1088/0957-0233/20/4/045703, 2009.

Gormley, P. G. and Kennedy, M.: Diffusion from a Stream Flowing through a Cylindrical Tube, P. Roy. Irish Acad. A, 52, 163–169, https://doi.org/10.2307/20488498, 1948.

Hale, B. N.: Temperature dependence of homogeneous nucleation rates for water: Near equivalence of the empirical fit of Wölk and Strey, and the scaled nucleation model, J. Chem. Phys., 122, 204 509, https://doi.org/10.1063/1.1906213, 2005.

Hanson, D. R. and Eisele, F.: Diffusion of H_2SO_4 in Humidified Nitrogen: Hydrated H_2SO_4, J. Phys. Chem. A, 104, 1715–1719, https://doi.org/10.1021/jp993622j, 2000.

Huang, L., Gong, S. L., Gordon, M., Liggio, J., Staebler, R. M., Stroud, C. A., Lu, G., Mihele, C., Brook, J. R., and Jia, C. Q.: Aerosol-computational fluid dynamics modeling of ultrafine and black carbon particle emission, dilution, and growth near roadways, Atmos. Chem. Phys., 14, 12 631–12 648, https://doi.org/10.5194/acp-14-12631-2014, 2014.

Hung, C., Krasnopoler, M. J., and Katz, J. L.: Condensation of a supersaturated vapor. VIII. The homogeneous nucleation of n-nonane, J. Chem. Phys., 90, 1856–1865, https://doi.org/10.1063/1.456027, 1989.

Jacobson, M. Z., Kittelson, D. B., and Watts, W. F.: Enhanced Coagulation Due to Evaporation and Its Effect on Nanoparticle Evolution, Environ. Sci. Technol., 39, 9486–9492, https://doi.org/10.1021/es0500299, 2005.

Johansson, C., Norman, M., and Gidhagen, L.: Spatial & temporal variations of PM10 and particle number concentrations in urban air, Environ. Monit. Assess., 127, 477–487, https://doi.org/10.1007/s10661-006-9296-4, 2007.

Jokinen, T., Sipilä, M., Junninen, H., Ehn, M., Lönn, G., Hakala, J., Petäjä, T., Mauldin III, R. L., Kulmala, M., and Worsnop, D. R.: Atmospheric sulphuric acid and neutral cluster measurements using CI-APi-TOF, Atmos. Chem. Phys., 12, 4117–4125, https://doi.org/10.5194/acp-12-4117-2012, 2012.

Karjalainen, P., Rönkkö, T., Pirjola, L., Heikkilä, J., Happonen, M., Arnold, F., Rothe, D., Bielaczyc, P., and Keskinen, J. .: Sulfur driven nucleation mode formation in diesel exhaust under transient driving conditions, Environ. Sci. Technol., 48, 2336–2343, https://doi.org/10.1021/es405009g, 2014.

Kashchiev, D.: On the relation between nucleation work, nucleus size, and nucleation rate, J. Chem. Phys., 76, 5098–5102, https://doi.org/10.1063/1.442808, 1982.

Keskinen, J. and Rönkkö, T.: Can real-world diesel exhaust particle size distribution be reproduced in the laboratory? A critical review, J. Air Waste Manage., 60, 1245–1255, https://doi.org/10.3155/1047-3289.60.10.1245, 2010.

Kirkby, J., Curtius, J., Almeida, J. a., Dunne, E., Duplissy, J., Ehrhart, S., Franchin, A., Gagné, S., Ickes, L., Kürten, A., Kupc, A., Metzger, A., Riccobono, F., Rondo, L., Schobesberger, S., Tsagkogeorgas, G., Wimmer, D., Amorim, A., Bianchi, F., Breitenlechner, M., David, A., Dommen, J., Downard, A., Ehn, M., Flagan, R. C., Haider, S., Hansel, A., Hauser, D., Jud, W., Junninen, H., Kreissl, F., Kvashin, A., Laaksonen, A., Lehtipalo, K., Lima, J., Lovejoy, E. R., Makhmutov, V., Mathot, S., Mikkilä, J., Minginette, P., Mogo, S., Nieminen, T., Onnela, A., Pereira, P., Petäjä, T., Schnitzhofer, R., Seinfeld, J. H., Sipilä, M., Stozhkov, Y., Stratmann, F., Tomé, A., Vanhanen, J., Viisanen, Y., Vrtala, A., Wagner, P. E., Walther, H., Weingartner, E., Wex, H., Winkler, P. M., Carslaw, K. S., Worsnop, D. R., Baltensperger, U., and Kulmala, M.: Role of sulphuric acid, ammonia and galactic cosmic rays in atmospheric aerosol nucleation, Nature, 476, 429–433, https://doi.org/10.1038/nature10343, 2011.

Kittelson, D.: Engines and nanoparticles: A review, J. Aerosol Sci., 29, 575–588, https://doi.org/10.1016/S0021-8502(97)10037-4, 1998.

Kittelson, D., Watts, W., Johnson, J., Thorne, C., Higham, C., Payne, M., Goodier, S., Warrens, C., Preston, H., Zink, U., Pickles, D., Goersmann, C., Twigg, M., Walker, A., and Boddy, R.: Effect of fuel and lube oil sulfur on the performance of a diesel exhaust gas continuously regenerating trap, Environ. Sci. Technol., 42, 9276–9282, https://doi.org/10.1021/es703270j, 2008.

Kulmala, M., Lehtinen, K., and Laaksonen, A.: Cluster activation theory as an explanation of the linear dependence between formation rate of 3 nm particles and sulphuric acid concentration, Atmos. Chem. Phys., 6, 787–793, https://doi.org/10.5194/acp-6-787-2006, 2006.

Kulmala, M., Kontkanen, J., Junninen, H., Lehtipalo, K., Manninen, H., Nieminen, T., Petäjä, T., Sipilä, M., Schobesberger, S., Rantala, P., Franchin, A., Jokinen, T., Järvinen, E., Äijälä, M., Kangasluoma, J., Hakala, J., Aalto, P., Paasonen, P., Mikkilä, J., Vanhanen, J., Aalto, J., Hakola, H., Makkonen, U., Ruuskanen, T., Mauldin III, R., Duplissy, J., Vehkamäki, H., Bäck, J., Kortelainen, A., Riipinen, I., Kurtén, T., Johnston, M., Smith, J., Ehn, M., Mentel, T., Lehtinen, K., Laaksonen, A., Kerminen, V.-M., and Worsnop, D.: Direct observations of atmospheric aerosol nucleation, Science, 339, 943–946, https://doi.org/10.1126/science.1227385, 2013.

Kupiainen-Määttä, O., Olenius, T., Korhonen, H., Malila, J., Dal Maso, M., Lehtinen, K., and Vehkamäki, H.: Critical cluster size cannot in practice be determined by slope analysis in atmospherically relevant applications, J. Aerosol Sci., 77, 127–144, https://doi.org/10.1016/j.jaerosci.2014.07.005, 2014.

Lähde, T., Rönkkö, T., Virtanen, A., Schuck, T. J., Pirjola, L., Hämeri, K., Kulmala, M., Arnold, F., Rothe, D., and Keskinen, J.: Heavy Duty Diesel Engine Exhaust Aerosol Particle and Ion Measurements, Environ. Sci. Technol., 43, 163–168, https://doi.org/10.1021/es801690h, 2009.

Lelieveld, J., Evans, J. S., Fnais, M., Giannadaki, D., and Pozzer, A.: The contribution of outdoor air pollution sources to premature mortality on a global scale, Nature, 525, 367–371, https://doi.org/10.1038/nature15371, 2015.

Lemmetty, M., Vehkamäki, H., Virtanen, A., Kulmala, M., and Keskinen, J.: Homogeneous Ternary H2SO4-NH3-H2O Nucleation and Diesel Exhaust: a Classical Approach, Aerosol Air Qual. Res., 7, 489–499, https://doi.org/10.4209/aaqr.2007.02.0008, 2007.

Lemmetty, M., Rönkkö, T., Virtanen, A., Keskinen, J., and Pirjola, L.: The effect of sulphur in diesel exhaust aerosol: Models compared with measurements, Aerosol Sci. Tech., 42, 916–929, https://doi.org/10.1080/02786820802360682, 2008.

Li, X. and Huang, Z.: Formation and transformation of volatile nanoparticles from a diesel engine during exhaust dilution, Chinese Sci. Bull., 57, https://doi.org/10.1007/s11434-011-4927-8, 2012.

Liu, Y. H., He, Z., and Chan, T. L.: Three-dimensional simulation of exhaust particle dispersion and concentration fields in the near-wake region of the studied ground vehicle, Aerosol Sci. Tech., 45, 1019–1030, https://doi.org/10.1080/02786826.2011.580021, 2011.

Lyyränen, J., Jokiniemi, J., Kauppinen, E. I., Backman, U., and Vesala, H.: Comparison of Different Dilution Methods for Measuring Diesel Particle Emissions, Aerosol Sci. Tech., 38, 12–23, https://doi.org/10.1080/02786820490247579, 2004.

Maricq, M., Chase, R., Xu, N., and Laing, P.: The effects of the catalytic converter and fuel sulfur level on motor vehicle particulate matter emissions: Light duty diesel vehicles, Environ. Sci. Technol., 36, 283–289, https://doi.org/10.1021/es010962l, 2002.

Maricq, M. M., Szente, J. J., and Jahr, K.: The Impact of Ethanol Fuel Blends on PM Emissions from a Light-Duty GDI Vehicle, Aerosol Sci. Tech., 46, 576–583, https://doi.org/10.1080/02786826.2011.648780, 2012.

McMurry, P. and Friedlander, S.: New particle formation in the presence of an aerosol, Atmos. Environ., 13, 1635–1651, https://doi.org/10.1016/0004-6981(79)90322-6, 1979.

Meyer, N. and Ristovski, Z.: Ternary Nucleation as a Mechanism for the Production of Diesel Nanoparticles: Experimental Analysis of the Volatile and Hygroscopic Properties of Diesel Exhaust Using the Volatilization and Humidification Tandem Differential Mobility Analyzer, Environ. Sci. Technol., 41, 7309–7314, https://doi.org/10.1021/es062574v, 2007.

Mordas, G., Manninen, H., Petäjä, T., Aalto, P., Hämeri, K., and Kulmala, M.: On operation of the ultra-fine water-based CPC TSI 3786 and comparison with other TSI models (TSI 3776, TSI 3772, TSI 3025, TSI 3010, TSI 3007), Aerosol Sci. Tech., 42, 152–158, https://doi.org/10.1080/02786820701846252, 2008.

Neitola, K., Brus, D., Makkonen, U., Sipilä, M., Mauldin III, R. L., Sarnela, N., Jokinen, T., Lihavainen, H., and Kulmala, M.: Total sulfate vs. sulfuric acid monomer concenterations in nucleation studies, Atmos. Chem. Phys., 15, 3429–3443, https://doi.org/10.5194/acp-15-3429-2015, 2015.

Ntziachristos, L., Giechaskiel, B., Pistikopoulos, P., Samaras, Z., Mathis, U., Mohr, M., Ristimäki, J., Keskinen, J., Mikkanen, P., Casati, R., Scheer, V., and Vogt, R.: Performance evaluation of a novel sampling and measurement system for exhaust particle characterization, SAE J.-Automot. Eng., pp. 2004–01–1439, https://doi.org/10.4271/2004-01-1439, 2004.

Olin, M., Dal Maso, M., and Rönkkö, T.: Sulfur driven nucleation in diesel exhaust: Simulations of a laboratory sampling system, in: Proceedings of the 18$^{\mathrm{th}}$ ETH-Conference on Combustion Generated Nanoparticles, Zürich, Switzerland, 22-25 June 2014, 2014.

Olin, M., Rönkkö, T., and Dal Maso, M.: CFD modeling of a vehicle exhaust laboratory sampling system: sulfur-driven nucleation and growth in diluting diesel exhaust, Atmos. Chem. Phys., 15, 5305–5323, https://doi.org/10.5194/acp-15-5305-2015, 2015.

Olin, M., Anttila, T., and Dal Maso, M.: Using a combined power law and log-normal distribution model to simulate particle formation and growth in a mobile aerosol chamber, Atmos. Chem. Phys., 16, 7067–7090, https://doi.org/10.5194/acp-16-7067-2016, 2016.

Paasonen, P., Nieminen, T., Asmi, E., Manninen, H., Petäjä, T., Plass-Dülmer, C., Flentje, H., Birmili, W., Wiedensohler, A., Horrak, U., Metzger, A., Hamed, A., Laaksonen, A., Facchini, M., Kerminen, V.-M., and Kulmala, M.: On the roles of sulphuric acid and low-volatility organic vapours in the initial steps of atmospheric new particle formation, Atmos. Chem. Phys., 10, 11 223–11 242, https://doi.org/10.5194/acp-10-11223-2010, 2010.

Pey, J., Querol, X., Alastuey, A., Rodriguez, S., Putaud, J., and Van Dingenen, R.: Source apportionment of urban fine and ultra-fine particle number concentration in a Western Mediterranean city, Atmos. Environ., 43, 4407–4415, https://doi.org/10.1016/j.atmosenv.2009.05.024, 2009.

Pirjola, L., Karl, M., Rönkkö, T., and Arnold, F.: Model studies of volatile diesel exhaust particle formation: are organic vapours involved in nucleation and growth?, Atmos. Chem. Phys., 15, 10 435–10 452, https://doi.org/10.5194/acp-15-10435-2015, 2015.

Pope, C., Burnett, R., Thun, M., Calle, E., Krewski, D., Ito, K., and Thurston, G.: Lung cancer, cardiopulmonary mortality, and long-term exposure to fine particulate air pollution, J. Amer. Med. Assoc., 287, 1132–1141, https://doi.org/10.1001/jama.287.9.1132, 2002.

Raes, F., Janssens, A., and Dingenen, R. V.: The role of ion-induced aerosol formation in the lower atmosphere, J. Aerosol Sci., 17, 466–470, https://doi.org/10.1016/0021-8502(86)90135-7, 1986.

Riccobono, F., Schobesberger, S., Scott, C. E., Dommen, J., Ortega, I. K., Rondo, L., Almeida, J., Amorim, A., Bianchi, F., Breitenlechner, M., David, A., Downard, A., Dunne, E. M., Duplissy, J., Ehrhart, S., Flagan, R. C., Franchin, A., Hansel, A., Junninen, H., Kajos, M., Keskinen, H., Kupc, A., Kürten, A., Kvashin, A. N., Laaksonen, A., Lehtipalo, K., Makhmutov, V., Mathot, S., Nieminen, T., Onnela, A., Petäjä, T., Praplan, A. P., Santos, F. D., Schallhart, S., Seinfeld, J. H., Sipilä, M., Spracklen, D. V., Stozhkov, Y., Stratmann, F., Tomé, A., Tsagkogeorgas, G., Vaattovaara, P., Viisanen, Y., Vrtala, A., Wagner, P. E., Weingartner, E., Wex, H., Wimmer, D., Carslaw, K. S., Curtius, J., Donahue, N. M., Kirkby, J., Kulmala, M., Worsnop, D. R., and Baltensperger, U.: Oxidation Products of Biogenic Emissions Contribute to Nucleation of Atmospheric Particles, Science, 344, 717–721, https://doi.org/10.1126/science.1243527, 2014.

Riipinen, I., Sihto, S.-L., Kulmala, M., Arnold, F., Dal Maso, M., Birmili, W., Saarnio, K., Teinilä, K., Kerminen, V.-M., Laaksonen, A., and Lehtinen, K. E. J.: Connections between atmospheric sulphuric acid and new particle formation during QUEST III–IV campaigns in Heidelberg and Hyytiälä, Atmos. Chem. Phys., 7, 1899–1914, https://doi.org/10.5194/acp-7-1899-2007, 2007.

Rissler, J., Swietlicki, E., Bengtsson, A., Boman, C., Pagels, J., Sandström, T., Blomberg, A., , and Löndahl, J.: Experimental determination of deposition of diesel exhaust particles in the human respiratory tract, J. Aerosol Sci., 48, 18–33, https://doi.org/10.1016/j.jaerosci.2012.01.005, 2012.

Rönkkö, T., Virtanen, A., Kannosto, J., Keskinen, J., Lappi, M., and Pirjola, L.: Nucleation mode particles with a nonvolatile core in the exhaust of a heavy duty diesel vehicle, Environ. Sci. Technol., 41, 6384–6389, https://doi.org/10.1021/es0705339, 2007.

Rönkkö, T., Lähde, T., Heikkilä, J., Pirjola, L., Bauschke, U., Arnold, F., Schlager, H., Rothe, D., Yli-Ojanperä, J., and Keskinen, J.: Effects of gaseous sulphuric acid on diesel exhaust nanoparticle formation and characteristics, Environ. Sci. Technol., 47, 11 882–11 889, https://doi.org/10.1021/es402354y, 2013.

Rönkkö, T., Pirjola, L., Ntziachristos, L., Heikkilä, J., Karjalainen, P., Hillamo, R., and Keskinen, J.: Vehicle Engines Produce Exhaust Nanoparticles Even When Not Fueled, Environ. Sci. Technol., 48, 2043–2050, https://doi.org/10.1021/es405687m, 2014.

Rönkkö, T., Kuuluvainen, H., Karjalainen, P., Keskinen, J., Hillamo, R., Niemi, J. V., Pirjola, L., Timonen, H. J., Saarikoski, S., Saukko, E., Järvinen, A., Silvennoinen, H., Rostedt, A., Olin, M., Yli-Ojanperä, J., Nousiainen, P., Kousa, A., and Dal Maso, M.: Traffic is a major source of atmospheric nanocluster aerosol, P. Natl. Acad. Sci. USA, 114, 7549–7554, https://doi.org/10.1073/pnas.1700830114, 2017.

Saito, K., Shinozaki, O., Seto, T., Kim, C.-S., Okuyama, K., Kwon, S.-B., and Lee, K. W.: The Origins of Nanoparticle Modes in the Number Distribution of Diesel Particulate Matter, in: SAE Technical Paper, SAE International, https://doi.org/10.4271/2002-01-1008, 2002.

Sakurai, H., Tobias, H., Park, K., Zarling, D., Docherty, K., Kittelson, D., McMurry, P., and Ziemann, P.: On-line measurements of diesel nanoparticle composition and volatility, Atmos. Environ., 37, 1199–1210, https://doi.org/10.1016/S1352-2310(02)01017-8, 2003.

Schneider, J., Hock, N., Weimer, S., Borrmann, S., Kirchner, U., Vogt, R., and Scheer, V.: Nucleation particles in diesel exhaust: Composition inferred from in situ mass spectrometric analysis, Environ. Sci. Technol., 39, 6153–6161, https://doi.org/10.1021/es049427m, 2005.

Sgro, L., Borghese, A., Speranza, L., Barone, A., Minutolo, P., Bruno, A., D'Anna, A., and D'Alessio, A.: Measurements of nanoparticles of organic carbon and soot in flames and vehicle exhausts, Environ. Sci. Technol., 42, 859–863, https://doi.org/10.1021/es070485s, 2008.

Sihto, S.-L., Kulmala, M., Kerminen, V.-M., Dal Maso, M., Petäjä, T., Riipinen, I., Korhonen, H., Arnold, F., Janson, R., Boy, M., Laaksonen, A., and Lehtinen, K. E. J.: Atmospheric sulphuric acid and aerosol formation: implications from atmospheric measurements for nucleation and early growth mechanisms, Atmos. Chem. Phys., 6, 4079–4091, https://doi.org/10.5194/acp-6-4079-2006, 2006.

Sihto, S.-L., Vuollekoski, H., Leppä, J., Riipinen, I., Kerminen, V.-M., Korhonen, H., Lehtinen, K., Boy, M., and Kulmala, M.: Aerosol dynamics simulations on the connection of sulphuric acid and new particle formation, Atmos. Chem. Phys., 9, 2933–2947, https://doi.org/10.5194/acp-9-2933-2009, 2009.

Stevens, R. G. and Pierce, J. R.: The contribution of plume-scale nucleation to global and regional aerosol and CCN concentrations: evaluation and sensitivity to emissions changes, Atmos. Chem. Phys., 14, 13 661–13 679, https://doi.org/10.5194/acp-14-13661-2014, 2014.

Stevens, R. G., Pierce, J. R., Brock, C. A., Reed, M. K., Crawford, J. H., Holloway, J. S., Ryerson, T. B., Huey, L. G., and Nowak, J. B.: Nucleation and growth of sulfate aerosol in coal-fired power plant plumes: sensitivity to background aerosol and meteorology, Atmos. Chem. Phys., 12, 189–206, https://doi.org/10.5194/acp-12-189-2012, 2012.

Sulonen, M. L., Kokko, M. E., Lakaniemi, A.-M., and Puhakka, J. A.: Electricity generation from tetrathionate in microbial fuel cells by acidophiles, J. Hazard. Mater., 284, 182–189, https://doi.org/10.1016/j.jhazmat.2014.10.045, 2015.

Taleb, D.-E., Ponche, J.-L., and Mirabel, P.: Vapor pressures in the ternary system water-nitric acid-sulfuric acid at low temperature: A reexamination, J. Geophys. Res.-Atmos., 101, 25 967–25 977, https://doi.org/10.1029/96JD02330, 1996.

Tobias, H., Beving, D., Ziemann, P., Sakurai, H., Zuk, M., McMurry, P., Zarling, D., Waytulonis, R., and Kittelson, D.: Chemical analysis of diesel engine nanoparticles using a nano-DMA/thermal desorption particle beam mass spectrometer, Environ. Sci. Technol., 35, 2233–2243, https://doi.org/10.1021/es0016654, 2001.

Uhrner, U., von Löwis, S., Vehkamäki, H., Wehner, B., Bräsel, S., Hermann, M., Stratmann, F., Kulmala, M., and Wiedensohler, A.: Dilution and aerosol dynamics within a diesel car exhaust plume-CFD simulations of on-road measurement conditions, Atmos. Environ., 41, 7440–7461, https://doi.org/10.1016/j.atmosenv.2007.05.057, 2007.

Vaaraslahti, K., Virtanen, A., Ristimäki, J., and Keskinen, J.: Nucleation Mode Formation in Heavy-Duty Diesel Exhaust with and without a Particulate Filter, Environ. Sci. Technol., 38, 4884–4890, https://doi.org/10.1021/es0353255, 2004.

Vaaraslahti, K., Keskinen, J., Giechaskiel, B., Solla, A., Murtonen, T., and Vesala, H.: Effect of lubricant on the formation of heavy-duty diesel exhaust nanoparticles, Environ. Sci. Technol., 39, 8497–8504, https://doi.org/10.1021/es0505503, 2005.

Vehkamäki, H. and Riipinen, I.: Thermodynamics and kinetics of atmospheric aerosol particle formation and growth, Chem. Soc. Rev., 41, 5160–5173, https://doi.org/10.1039/C2CS00002D, 2012.

Vehkamäki, H., Kulmala, M., Lehtinen, K., and Noppel, M.: Modelling binary homogeneous nucleation of water-sulfuric acid vapours: Parameterisation for high temperature emissions, Environ. Sci. Technol., 37, 3392–3398, https://doi.org/10.1021/es0263442, 2003.

Virtanen, A., Rönkkö, T., Kannosto, J., Ristimäki, J., Mäkelä, J., Keskinen, J., Pakkanen, T., Hillamo, R., Pirjola, L., and Hämeri, K.: Winter and summer time size distributions and densities of traffic-related aerosol particles at a busy highway in Helsinki, Atmos. Chem. Phys., 6, 2411–2421, https://doi.org/10.5194/acp-6-2411-2006, 2006.

Vogt, R., Scheer, V., Casati, R., and Benter, T.: On-road measurement of particle emission in the exhaust plume of a diesel passenger car, Environ. Sci. Technol., 37, 4070–4076, https://doi.org/10.1021/es0300315, 2003.

Vouitsis, E., Ntziachristos, L., and Samaras, Z.: Modelling of diesel exhaust aerosol during laboratory sampling, Atmos. Environ., 39, 1335 – 1345, https://doi.org/10.1016/j.atmosenv.2004.11.011, 2005.

Wang, Y. and Zhang, K.: Coupled turbulence and aerosol dynamics modeling of vehicle exhaust plumes using the CTAG model, Atmos. Environ., 59, 284–293, https://doi.org/10.1016/j.atmosenv.2012.04.062, 2012.

Weber, R. J., Marti, J. J., McMurry, P. H., Eisele, F. L., Tanner, D. J., and Jefferson, A.: Measured Atmospheric New Particle Formation Rates: Implications for Nucleation Mechanisms, Chem. Eng. Commun., 151, 53–64, https://doi.org/10.1080/00986449608936541, 1996.

Wölk, J. and Strey, R.: Homogeneous Nucleation of H_2O and D_2O in Comparison: The Isotope Effect, J. Phys. Chem. B, 105, 11 683–11 701, https://doi.org/10.1021/jp0115805, 2001.

Wyslouzil, B. E. and Wölk, J.: Overview: Homogeneous nucleation from the vapor phase—The experimental science, J. Chem. Phys., 145, 211 702, https://doi.org/10.1063/1.4962283, 2016.

Zeleznik, F. J.: Thermodynamic Properties of the Aqueous Sulfuric Acid System to 350 K, J. Phys. Chem. Ref. Data, 20, 1157–1200, https://doi.org/10.1063/1.555899, 1991.

Zhang, R., Khalizov, A., Wang, L., Hu, M., and Xu, W.: Nucleation and Growth of Nanoparticles in the Atmosphere, Chem. Rev., 112, 1957–2011, https://doi.org/10.1021/cr2001756, 2012.

1 Comparing simulated sulfuric acid concentrations to the measured concentrations

In addition to determining sulfuric acid concentrations ($[H_2SO_4]$) through inverse modeling, they were also measured using a nitrate ion (NO_3^-) based chemical ionization Atmospheric Pressure interface Time-Of-Flight mass spectrometer (CI-APi-TOF, Jokinen et al. (2012)) and Ion Chromatography (IC, Sulonen et al. (2015)).

The CI-APi-TOF used NO_3^- ions as reagent ions to detect H_2SO_4 as bisulfate ions (HSO_4^-) and their clusters with nitric acid (HNO_3) in an APi-TOF mass spectrometer (Tofwerk AG, Switzerland and Aerodyne Research Inc., USA). The CI-APi-TOF outputs the concentrations of the measured ions as counts per second (c_{ion}) which need to be converted to absolute H_2SO_4 concentrations with the equation (Tröstl et al., 2016)

$$[H_2SO_4] = C \cdot \ln\left(1 + \frac{c_{HSO_4^-} + c_{HNO_3 \cdot HSO_4^-} + c_{H_2SO_4 \cdot HSO_4^-}}{c_{NO_3^-} + c_{HNO_3 \cdot NO_3^-} + c_{(HNO_3)_2 \cdot NO_3^-}}\right), \tag{S1}$$

where C is an experimentally determined calibration coefficient having the value of $1.3 \times 10^9\,\mathrm{cm}^{-3}$ for the device used. The CI-APi-TOF works well in measuring H_2SO_4 from the atmosphere; however, because the concentrations in this experiment were significantly higher, the raw sample needed to be diluted. The sample flow rate to the CI-APi-TOF was (10.0 ± 0.2) slpm and it was prepared by diluting the raw sample with compressed air heated to 300 °C with the flow rate of almost 10 slpm. The dilution ratio, determined using carbon dioxide (CO_2) measurement, was 133 ± 7. This corresponds to the raw sample flow rate of (0.075 ± 0.004) slpm. The length of the sampling line before the dilution point was 70 mm and between the dilution point and the inlet of the CI-APi-TOF it was 1720 mm. According to the diffusional losses (Gormley and Kennedy, 1948), only the fraction of $(6 \pm 2) \times 10^{-4}$ of H_2SO_4 penetrated to the CI-APi-TOF inlet, of which the major contribution resulted from the sampling line before the dilution point having a very low flow rate.

The IC measurement was performed by sucking the raw sample with the flow rate of (2.76 ± 0.02) slpm through a gas washing bottle with a fritted disc and analyzing SO_4^{2-} ion concentration from the liquid sample with the IC instrument off-line. The length of the sampling line before the washing bottle was 525 mm, for which the calculated penetration due to diffusional losses is $(20.4 \pm 0.4)\,\%$. The effect of the line length on the diffusional losses was examined using also a sampling line having the length of 750 mm, for which the calculated penetration is $(12.9 \pm 0.4)\,\%$. However, according to the measured $[SO_4^{2-}]$, the line length had no effect on the penetrated fraction, implying over-predicted diffusional losses in the first part of the sampling line, probably due to saturating H_2SO_4 liquid onto the sampling lines. The gas washing bottle was filled with 130 ml of deionized Milli-Q water and the gas collecting time was 20 ... 360 min, depending on the expected $[H_2SO_4]$ in the raw sample. The collection efficiency of the gas washing bottle was measured by collecting the sample also with 80 ml of water having approximately half the bubbling height of 130 ml of water. According to the measured $[SO_4^{2-}]$, the amount of water had no effect on the results; thus, the collection efficiency was high, or at least the maximum achievable in the measurement conditions.

H_2SO_4 concentrations in the raw sample with different H_2SO_4 evaporator temperatures measured with the CI-APi-TOF and the IC are presented together with the simulated and theoretical concentrations in Fig. S1. Surprisingly, the CI-APi-TOF data are at a somewhat higher level compared to the lossless level which is probably partially accounted by the calculated diffusional losses between the measurement point and the device, which have a large uncertainty due to a very low sample flow rate. The reason why the data lies near the lossless level is presumably due to the direction of adjusting T_{sa} which was from high to low temperatures during the CI-APi-TOF measurement and the time waited for the CI-APi-TOF signal to stabilize was short with respect to the equilibration time of the sampling line. Performing higher saturator temperatures first can saturate the walls of the sampling lines with H_2SO_4 which could later act as preventing diffusional losses with lower saturator temperatures and thus result into the lossless level. The IC data are at the level of about 5 % of the lossless theoretical level, but there are also significant outliers at higher levels. The level of the IC data can be lowered due to the sample containing CO_2. CO_2 can lower the pH of the liquid sample in the gas washing bottle, which can further decrease the collection efficiency of SO_4^{2-}. The 5 % level of the IC data and the direction of the effect of CO_2 would denote maximum diffusional losses onto the sampling lines between the evaporator and the $[H_2SO_4]_{\text{raw}}$ measurement point of 95 %, which lies in the range of calculated diffusional losses of 0 ... 98 %.

Nevertheless, both the measured data sets agree well with the shape of the theoretical curve, which implies that $[H_2SO_4]_{raw}$ can be estimated using T_{sa}. However, the absolute value for $[H_2SO_4]_{raw}$ cannot be satisfactorily estimated using neither T_{sa} nor the measured concentrations due to the discrepancy of the measured concentrations. Therefore, the simulations of this study did not use the measured concentrations as the boundary conditions; instead, the $[H_2SO_4]_{raw}$ values were obtained through inverse modeling.

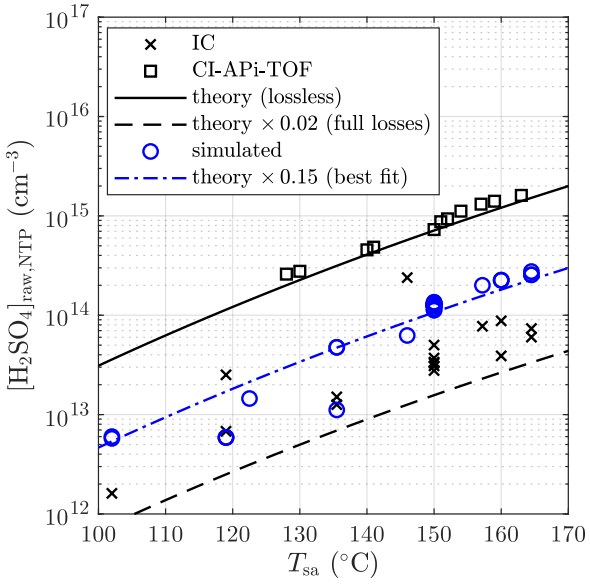

Figure S1. Simulated sulfuric acid concentrations in the raw sample compared to the measured and the theoretical concentrations with different sulfuric acid evaporator temperatures.

2 Error estimation for particle size distribution measurements

The disagreement of sub-6 nm particle size distributions measured by the combination of the PSM and the CPC 3775 and by the Nano-SMPS is examined by estimating the sources and the magnitudes of errors in measured concentrations for these devices.

2.1 Calculating the error bars for the combination of the PSM and the CPC 3775

The particle number size distributions are calculated using the step-wise method according to Lehtipalo et al. (2014). Backwards-correcting the measured distributions to represent the distributions after the ED requires multiplying the data with the DR of the BD and dividing by the penetration efficiency of particles in the sampling lines between the ED and the measurement devices. Finally, the equation to obtain the distribution at particle size $D_{p,i}$ after the ED from the measured concentrations is

$$\nu(D_{p,i}) = \frac{N_i^{\text{smaller}} - N_i^{\text{larger}}}{\log(D_{p,i}^{\text{larger}}/D_{p,i}^{\text{smaller}}) \cdot p(D_{p,i}, L/Q)} \tag{S2}$$

where N_i^{smaller} and N_i^{larger} are particle number concentrations measured with the D_{50}-cut-sizes of $D_{p,i}^{\text{smaller}}$ and $D_{p,i}^{\text{larger}}$, respectively. $D_{p,i}$ is the geometric mean diameter of the D_{50}-cut-sizes and $p(D_{p,i}, L/Q)$ is the penetration efficiency of particles with

a diameter of $D_{\mathrm{p},i}$ in a sampling line with a length of $L_{\mathrm{lines}} = L$ and flow rate of $Q_{\mathrm{lines}} = Q$, according to diffusional losses calculated with the equations of Gormley and Kennedy (1948). This penetration efficiency takes also the BD into account because its operation principle is also based on diffusional losses; thus, L denotes the effective length of the combined effect of the sampling lines and the BD.

Systematic errors for the calculated size distributions after the ED include the uncertainty of the cut-diameters and the uncertainty of the value of L/Q. Because the detection efficiency curves of the PSM and CPC 3775 are measured using particles having a different composition than H_2SO_4-H_2O, as in these measurements, and because environmental parameters, such as temperature, can have effects on the detection efficiency curves, the reported cut-diameters may not hold exactly. The uncertainty of 20 % is estimated for the cut-diameters and also for the ratio of the cut-diameters $D_{\mathrm{p},i}^{\mathrm{larger}}/D_{\mathrm{p},i}^{\mathrm{smaller}}$ because it is expected that if one of the cut-diameters is deviated towards smaller or larger particle sizes, another one is deviated towards the same direction. 10 % uncertainty is estimated for the value of L/Q, which includes the measurement uncertainty for both L and Q and the uncertainty in the equations of Gormley and Kennedy (1948).

The standard deviations of the measured concentrations caused by the instability of the particle generation are in the range of 1 ... 25 %, depending on the concentration level and particle sizes: higher concentrations and larger particle sizes provided more stable particle generation compared to lower concentrations and smaller particle sizes.

The error bars for $\nu(D_{\mathrm{p},i})$ can be calculated with the equation

$$\frac{\Delta\nu}{\nu} = \sqrt{\left(\frac{\partial\nu}{\partial N_i^{\mathrm{smaller}}}\frac{\Delta N_i^{\mathrm{smaller}}}{\nu}\right)^2 + \left(\frac{\partial\nu}{\partial N_i^{\mathrm{larger}}}\frac{\Delta N_i^{\mathrm{larger}}}{\nu}\right)^2 + \left(\frac{\partial\nu}{\partial\log(D_{\mathrm{p},i}^{\mathrm{larger}}/D_{\mathrm{p},i}^{\mathrm{smaller}})}\frac{\Delta\log(D_{\mathrm{p},i}^{\mathrm{larger}}/D_{\mathrm{p},i}^{\mathrm{smaller}})}{\nu}\right)^2 + \left(\frac{\partial\nu}{\partial p}\frac{\Delta p}{\nu}\right)^2}$$

$$= \sqrt{\left(\frac{\Delta N_i^{\mathrm{smaller}}}{N_i^{\mathrm{smaller}} - N_i^{\mathrm{larger}}}\right)^2 + \left(\frac{\Delta N_i^{\mathrm{larger}}}{N_i^{\mathrm{smaller}} - N_i^{\mathrm{larger}}}\right)^2 + \left(\frac{\Delta\log(D_{\mathrm{p},i}^{\mathrm{larger}}/D_{\mathrm{p},i}^{\mathrm{smaller}})}{\log(D_{\mathrm{p},i}^{\mathrm{larger}}/D_{\mathrm{p},i}^{\mathrm{smaller}})}\right)^2 + \left(\frac{\Delta p}{p}\right)^2} \tag{S3}$$

where $\Delta N_i^{\mathrm{smaller}}$ and $\Delta N_i^{\mathrm{smaller}}$ are the standard deviations of the concentrations, depending on the measurement case, the third term is 0.2^2 because $\Delta(D_{\mathrm{p},i}^{\mathrm{larger}}/D_{\mathrm{p},i}^{\mathrm{smaller}})/(D_{\mathrm{p},i}^{\mathrm{larger}}/D_{\mathrm{p},i}^{\mathrm{smaller}}) = 20\,\%$, and Δp depends on the particle size and is calculated with the equation

$$\frac{\Delta p}{p} = \sqrt{\left(\frac{\partial p}{\partial(L/Q)}\frac{\Delta(L/Q)}{p}\right)^2 + \left(\frac{\partial p}{\partial D_{\mathrm{p},i}}\frac{\Delta D_{\mathrm{p},i}}{p}\right)^2} \tag{S4}$$

using $\Delta(L/Q)/(L/Q) = 10\,\%$ and $\Delta D_{\mathrm{p},i}/D_{\mathrm{p},i} = 20\,\%$.

2.2 Calculating the error bars for the Nano-SMPS

The particle number size distributions reported by the Nano-SMPS device have already went through the manufacturer's inversion algorithm. Thus, the inverse modeling of this work does not try to predict the concentration measured as a function of time measured by the CPC 3776, acting as a particle counter in the Nano-SMPS system. Instead, the inverse modeling takes only the diffusional losses in the sampling lines and the CPC 3776 detection efficiency curve into account, but not, e.g., the radioactive charger efficiency and the diffusional losses inside the device. It is partly unknown what is included in the manufacturer's inversion algorithm, but at least the charger efficiency and the diffusional losses inside the device are included. The inversion algorithm probably includes also the CPC 3776 detection efficiency curve, f_{CPC}, but it is, however, included in the inverse modeling of this work because it seems that it may differ significantly from the curve reported by the manufacturer, according to Hermann et al. (2007) and Mordas et al. (2008), as presented in Fig. S2. Unfortunately, the curve for the device used in these measurements is not measured; therefore, the inversion modeling uses the one reported by Mordas et al. (2008) because it lies between the other two curves, representing an average one. The uncertainty of the detection efficiency at a specific diameter is calculated from the maximum range of variation of the detection efficiencies from these three different sources.

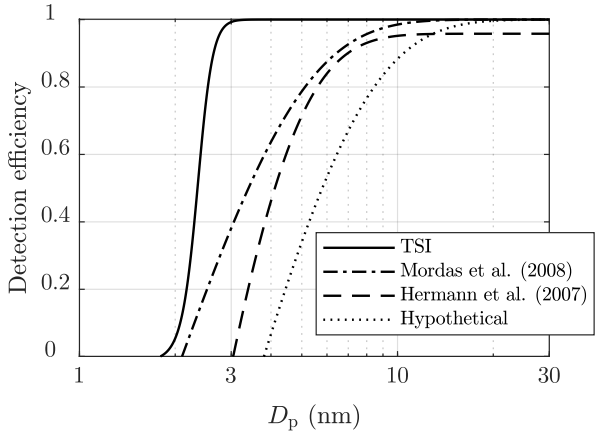

Figure S2. The CPC 3776 detection efficiency curves as a function of particle size reported by the manufacturer, Hermann et al. (2007), and Mordas et al. (2008). Additionally, a hypothetical curve correcting the disagreement between sub-6 nm particle size distributions measured by the Nano-SMPS and PSM+CPC system is presented.

The hypothetical detection efficiency curve presented in Fig. S2 is based on the curve reported by Mordas et al. (2008) but with different parameters. If this hypothetical curve is the actual curve of the device used, the size distributions as in Fig. 4 will be corrected to the distributions presented in Fig. S3, from which it can be seen that the size distributions measured by different devices correspond clearly better, at least for the two cases having the lowest T_sa. The PSM+CPC distribution for the case having the highest T_sa is probably overestimated because, according to Fig. 10 (c), the concentrations measured with different cut-diameters are on the same level, implying that there is not a notable amount of particles in that size range.

Other systematical errors, in addition to the uncertainty involved in the CPC 3776 detection efficiency curve, include the uncertainties of the charger efficiency, the diffusional losses, and the particle sizes interpreted by the manufacturer's inversion algorithm. The charger of the Nano-SMPS used was a TSI 3077 radioactive Kr-85 charger, which is based on charging particles bipolarly to the charge equilibrium state. The inversion algorithm uses the positive charge distribution function, f_charger, reported by Wiedensohler (1988). It is a semi-empirical function in which the mobilities and masses of positive and negative ions in the carrier gas are fitted based on the charge distribution measurements (Hussin et al., 1983; Adachi et al., 1985; Wiedensohler et al., 1986) made for particles larger than 5 nm in diameters. Alonso et al. (1997) have measured the charge distributions down to particle diameters of 2.5 nm. Unfortunately, the charger distributions from all these measurements differ, especially for the smallest particle sizes, and have thus different ion parameters, due to different particle compositions, carrier gas compositions, and the accuracies of the particle size measurements. Therefore, the charger efficiency function selected in the manufacturer's inversion algorithm is not exact. Based on the differences between the results of these charge distribution measurements, the uncertainties of 30, 20, and 10 % for the charger efficiencies at particle diameters of 6, 10, and 20 nm, respectively, are estimated. Another factor causing uncertainty for the charger efficiency is how satisfactorily the charge distribution is developed to the equilibrium state. If the residence time inside the charger is too short (Alonso et al., 1997), the activity of the charger is too low (de La Verpilliere et al., 2015) (e.g, if the activity of the charger is depleted due to a long operating life), or if the particle concentration is too high compared to the ion concentration (Wiedensohler et al., 2012), the equilibrium state may not be reached and the charger efficiency is overestimated. According to the deviations of the charge distributions in the measurements of de La Verpilliere et al. (2015) from the charge distribution function of Wiedensohler (1988), the uncertainties of 40, 30, and 20 % for the charger efficiencies at particle diameters of 2, 6, and 10 nm, respectively, are estimated. Because the particles before the Nano-SMPS are supposedly uncharged in this work, the possible incomplete reaching of the charge equilibrium state causes that the particles are less charged than predicted. Therefore, the concentrations would be underestimated, and thus the error bars related to this are considered only towards the positive direction.

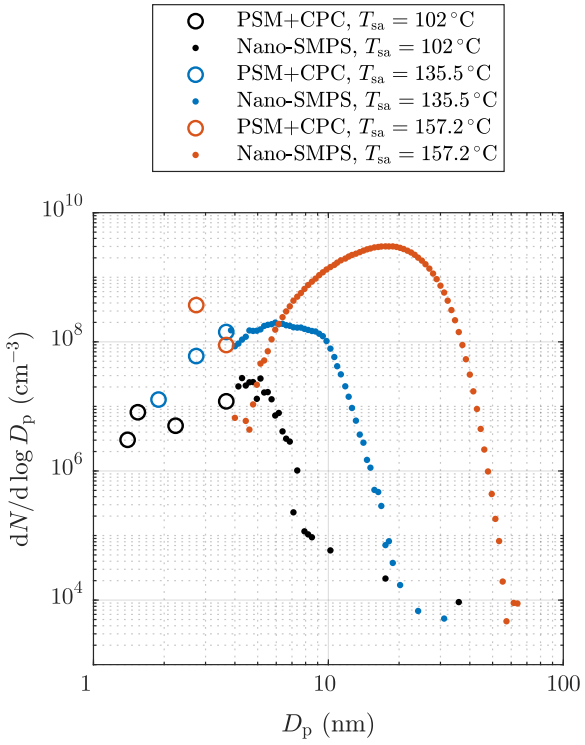

Figure S3. The corrected particle size distributions as in Fig. 4 if the detection efficiency curve of the CPC 3776 would be the hypothetical curve presented in Fig. S2.

The diffusional losses of the particles in the sampling lines of this work are based on the equations of Gormley and Kennedy (1948) using the $L_{\text{lines}}/Q_{\text{lines}}$ parameter as in the case of the PSM+CPC system (the uncertainty of 10 % for the $L_{\text{lines}}/Q_{\text{lines}}$ parameter in this case is again estimated). The correction of the diffusional losses inside the Nano-SMPS device is also based on those equations in the manufacturer's inversion algorithm. The algorithm uses an empirically fitted $L_{\text{device}}/Q_{\text{device}}$ value which included the whole route of the particles inside the device even though the route is not a perfect laminar circular tube flow, for which the analytical solution by Gormley and Kennedy (1948) is based on. Therefore, the penetration function for particles inside the device, p_{device}, may not be exact and the uncertainty of 10 % for the $L_{\text{device}}/Q_{\text{device}}$ parameter is estimated.

The correction factor assumed to exist in the inversion algorithm of the Nano-SMPS, to which the penetration in the sampling lines, p_{lines}, is added, is

$$C(D_{\mathrm{p},i}) = \frac{1}{f_{\text{charger}}(D_{\mathrm{p},i}) \cdot f_{\text{CPC}}(D_{\mathrm{p},i}) \cdot p_{\text{device}}(D_{\mathrm{p},i}, L_{\text{device}}/Q_{\text{device}}) \cdot p_{\text{lines}}(D_{\mathrm{p},i}, L_{\text{lines}}/Q_{\text{lines}})}. \tag{S5}$$

The concentration measured with a specific DMA (Differential Mobility Analyzer) voltage at a specific time, related to the particle diameter of $D_{\mathrm{p},i}$ (obtained though the inversion algorithm), is multiplied with $C(D_{\mathrm{p},i})$ in order to obtain the size distribution in a location of L_{lines} before the device, i.e., after the ED in this case. For very small particles, all the four functions in Eq. (S5) have very low value; and thus, the value of $C(D_{\mathrm{p},i})$ is extremely high. This is illustrated in Fig. S4 from which it can be observed that the value for sub-6 nm particles is several orders of magnitude. Very high correction factor denotes very low number of particle counts detected by the CPC at a specific diameter, and very low counts do not provide good accuracy due to statistics: there may be only a few randomly detected single particles or there may be even not a single detection at all during the time dedicated to that particle size, even though multiple scans have been performed for one measurement case.

In the case of no or very low detection of single particles, the error bars cannot be calculated. Because the correction factor increases very steeply with decreasing particle size, the uncertainties involved in the functions in Eq. (S5) can deviate it in high extent. Another consequence of the steep behavior of the correction factor is that if there is even a minor error in the interpreted particle diameters, the value of the correction factor can be significantly misestimated. There are several factors that can cause error to the particle diameters measured by the Nano-SMPS (Wiedensohler et al., 2012); here, the uncertainty of 5 % is estimated for the diameters.

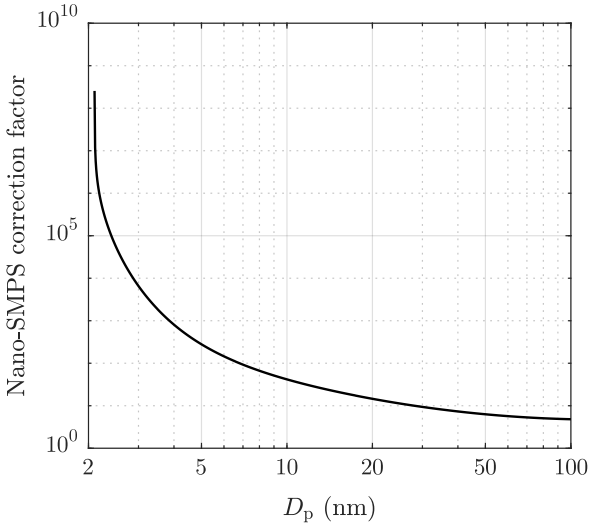

Figure S4. Nano-SMPS correction factor, as in Eq. (S5), used to correct the measured particle concentrations in the data inversion.

The error bars for the size distributions, $\nu(D_{\mathrm{p},i})$, can be calculated with the equation

$$\frac{\Delta\nu}{\nu} = \sqrt{\left(\frac{\Delta\nu'}{\nu'}\right)^2 + \left(\frac{\Delta C}{C}\right)^2} \tag{S6}$$

where $\Delta\nu'$ is the standard deviation of the size distributions at the particle diameter of $D_{\mathrm{p},i}$ output by the device, ν', and ΔC is the uncertainty of the Nano-SMPS correction factor. $\Delta\nu'$ represents the standard deviation caused by the instability in the particle generation, as in the case of the PSM+CPC system, but also by the low counting statistics for the particles sizes having a very low overall detection efficiency and for the particle sizes having low concentration in the measured case. ΔC is calculated by

$$\begin{aligned}\frac{\Delta C}{C} &= \sqrt{\left(\frac{\partial C}{\partial f_{\text{charger}}}\frac{\Delta f_{\text{charger}}}{C}\right)^2 + \left(\frac{\partial C}{\partial f_{\text{CPC}}}\frac{\Delta f_{\text{CPC}}}{C}\right)^2 + \left(\frac{\partial C}{\partial p_{\text{device}}}\frac{\Delta p_{\text{device}}}{C}\right)^2 + \left(\frac{\partial C}{\partial p_{\text{lines}}}\frac{\Delta p_{\text{lines}}}{C}\right)^2 + \left(\frac{\partial C}{\partial D_{\mathrm{p},i}}\frac{\Delta D_{\mathrm{p},i}}{C}\right)^2} \\ &= \sqrt{\left(\frac{\Delta f_{\text{charger}}}{f_{\text{charger}}}\right)^2 + \left(\frac{\Delta f_{\text{CPC}}}{f_{\text{CPC}}}\right)^2 + \left(\frac{\Delta p_{\text{device}}}{p_{\text{device}}}\right)^2 + \left(\frac{\Delta p_{\text{lines}}}{p_{\text{lines}}}\right)^2 + \left(\frac{\partial C}{\partial D_{\mathrm{p},i}}\frac{\Delta D_{\mathrm{p},i}}{C}\right)^2}\end{aligned} \tag{S7}$$

where $\Delta f_{\text{charger}}/f_{\text{charger}}$ and $\Delta f_{\text{CPC}}/f_{\text{CPC}}$ are the relative uncertainties for f_{charger} and f_{CPC} having the values mentioned before, Δp_{device} and Δp_{lines} are the uncertainties for the penetration efficiencies, p_{device} and p_{lines}, and the last term represents the uncertainty of C caused by the uncertainty of particle diameters. Δp_{device} and Δp_{lines} depend on the particle diameter and are

calculated by

$$\Delta p_{\text{device}} = \frac{\partial p_{\text{device}}}{\partial(L_{\text{device}}/Q_{\text{device}})} \cdot \Delta(L_{\text{device}}/Q_{\text{device}})$$
$$\Delta p_{\text{lines}} = \frac{\partial p_{\text{lines}}}{\partial(L_{\text{lines}}/Q_{\text{lines}})} \cdot \Delta(L_{\text{lines}}/Q_{\text{lines}}) \tag{S8}$$

which differ from Eg. (S4) by missing the effect of the particle diameter because that effect is included in the last term of Eq. (S7). The last term represent the total effect of the particle diameter on C because the particle diameter is involved in all other four terms.

2.3 Calculated error bars for the size distributions

The relative uncertainties for the size distributions between 2 and 10 nm after the ED caused by the different uncertainties involved in the size distribution measurements are presented in Tab. S1. For the PSM+CPC system, the most significant systematic errors arise from the uncertainty in the cut-diameters (12 ... 30 %), partly due to correcting the diffusional losses in sampling lines needed in backwards-correcting the measured distributions to represent the distributions after the ED. For the Nano-SMPS, the uncertainty of the charger efficiency plays a major role in the systematic errors (40 ... 66 %), but the uncertainty of the CPC 3776 detection efficiency curve has also a significant role for the smallest particles (55 % for 3.7 nm). The error bars decrease steeply when measuring particles sized 10 nm or larger using the Nano-SMPS. Both devices are, in theory, capable in measuring the size distribution at 3.7 nm, but the error bars for the Nano-SMPS are clearly higher compared to the PSM+CPC system. Therefore, the PSM+CPC system suits better in measuring near that diameter.

Table S1. The percentual uncertainties for the size distributions after the ED, $\Delta\nu/\nu$ (%), for the selected particle diameters. The first seven lines represent the systematical error of the devices and they are independent of the measurement case. The last two lines represent the effect of the standard deviation for two measurement cases having small and large particles.

Device	PSM+CPC		Nano-SMPS		
D_{p}	2 nm	3.7 nm	3.7 nm	6 nm	10 nm
Diffusional losses in sampling lines $\left(\frac{\Delta(L_{\text{lines}}/Q_{\text{lines}})}{L_{\text{lines}}/Q_{\text{lines}}} = 10\,\%\right)$	8	3	4	2	1
Diffusional losses in sampling lines $\left(\frac{\Delta D_{\text{p},i}}{D_{\text{p},i}} = 20\,\%\right)$	30	12			
PSM detection efficiency $\left(\frac{\Delta(D_{\text{p},i}^{\text{larger}}/D_{\text{p},i}^{\text{smaller}})}{D_{\text{p},i}^{\text{larger}}/D_{\text{p},i}^{\text{smaller}}} = 20\,\%\right)$	20	20			
Kr-85 charger efficiency			66	61	40
CPC 3776 detection efficiency			55	8	0.7
Diffusional losses inside the DMA $\left(\frac{\Delta(L_{\text{lines}}/Q_{\text{lines}})}{L_{\text{lines}}/Q_{\text{lines}}} = 10\,\%\right)$			16	7	3
Nano-SMPS correction factor $\left(\frac{\Delta D_{\text{p},i}}{D_{\text{p},i}} = 5\,\%\right)$			32	17	10
Random error in $D_{\bar{m}} = 3.6\,\text{nm}$ case (102 °C)	61	22	–[a]	72	–[a]
Random error in $D_{\bar{m}} = 19\,\text{nm}$ case (157.2 °C)	∞[b]	250	–[a]	24	10

[a] Cannot be calculated due to insufficient particle counts.
[b] For this point, $\nu(2\,\text{nm}) = 0$ but $\Delta\nu$ is a non-zero number due to standard deviation.

Random errors caused by the instability of the particle generation and low counting statistics of the Nano-SMPS also have significant effects for the both devices if there is not a notable amount of concentration in a specific size range. In the case with $D_{\bar{m}} = 3.6\,\mathrm{nm}$, there is a notable amount of concentration in the PSM+CPC size range, and thus, the error bars are relatively low (22 ... 61 %) for the PSM+CPC system. For the Nano-SMPS, the standard deviation for 6 nm particles is 72 %, which is, however, the most accurately measured particle size in that case: larger particles are inexistent and smaller particles are not detected; thus, low counting statistics cause high errors. In the case with $D_{\bar{m}} = 19\,\mathrm{nm}$, the Nano-SMPS suits well in measuring at the particle size of 10 nm (the standard deviation of 10 % originating mainly from the instability in the particle generation) and also relatively well at the particle size of 6 nm (the standard deviation of 24 %), but the errors increase with the particles smaller than 6 nm. Conversely, the PSM+CPC system has high error bars because the concentration in the PSM+CPC size range is so low that the difference between the concentrations measured with different cut-diameters are smaller than the standard deviation of the concentrations (see Fig. 10), which is always a problem with the PSM having a cumulative nature in measuring concentrations, if the cut-diameters of the adjacent saturator flow rates are too near or the measured signal is too instable. This issue can be overcome by skipping the data measured with the adjacent cut-diameters or even by considering only the data measured with the smallest and with the largest cut-diameter. However, while the error bars will be narrower in this alternative method, the information on the shape of the size distribution in that size range will diminish.

The error bars for the size distributions shown in Fig. 4 are presented in Fig. S5. By considering the error bars, the distributions from the both devices agree for the cases in panes (a) and (c), whereas the case in pane (b) has still some disagreement implying that other error sources than accounted here can be involved in the measurements using these devices. According to the error bars near the particle size of 4 nm connecting the two size distributions, the PSM+CPC system provides more reliable results in the cases in panes (a) and (b). Conversely, in the case in pane (c), the Nano-SMPS provides more reliable results because, although there are two points in the PSM+CPC distribution, the alternative method shows no particles at all. However, the error bars for the alternative method are high; thus, the probability of the existence of particles in the PSM+CPC size range is high. Nevertheless, the fraction of particles in that size range compared to the total particle count is, definitely, some orders of magnitude smaller than in the cases in panes (a) and (b). Figure S6 presents the error bars for the distributions shown in Fig. 11.

In conclusion, the suitability of the Nano-SMPS for the particle sizes smaller than $\sim$10 nm is weak especially due to the uncertainties involved in the radioactive charger efficiency and the CPC 3776 detection efficiency. Wiedensohler et al. (2012) have performed an intercomparison of several mobility particle sizers, in which the different devices provided a good agreement for the particle sizes larger than $\sim$15 nm but had significant disagreements for the smaller particle sizes, without explanation. Due to the incapability of the Nano-SMPS in determining the size distribution reliably in sub-10 nm diameter range, in all of the cases studied here and elsewhere, the PSM+CPC system suits clearly better in determining the size distribution in that particle size range, or at least the total number concentration of particles larger than $\sim$1 nm.

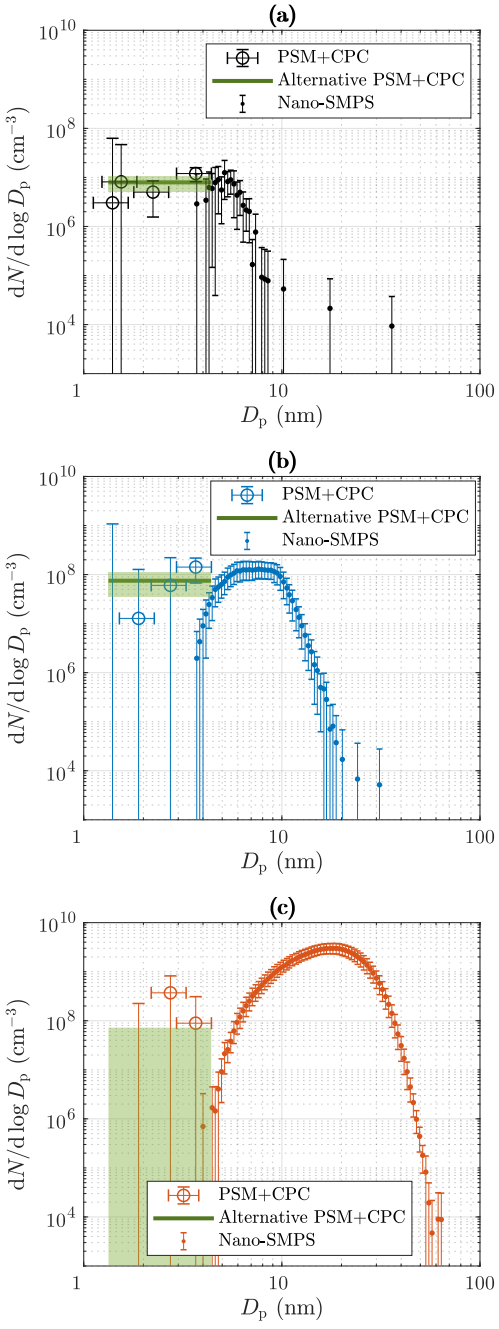

Figure S5. The measured size distributions for the measurement cases having the T_{sa} of (a) 102 °C, (b) 135.5 °C, and (c) 157.2 °C, as shown in Fig. 4, with the error bars. The alternative PSM+CPC distributions represent the distributions using only the concentrations measured with the smallest and the largest cut-diameters, in order to narrow the error bars. The green shaded areas denote the error bars for the distributions from the alternative method. The error bars for the particle sizes from the Nano-SMPS (±5 %) are not shown for clarity.

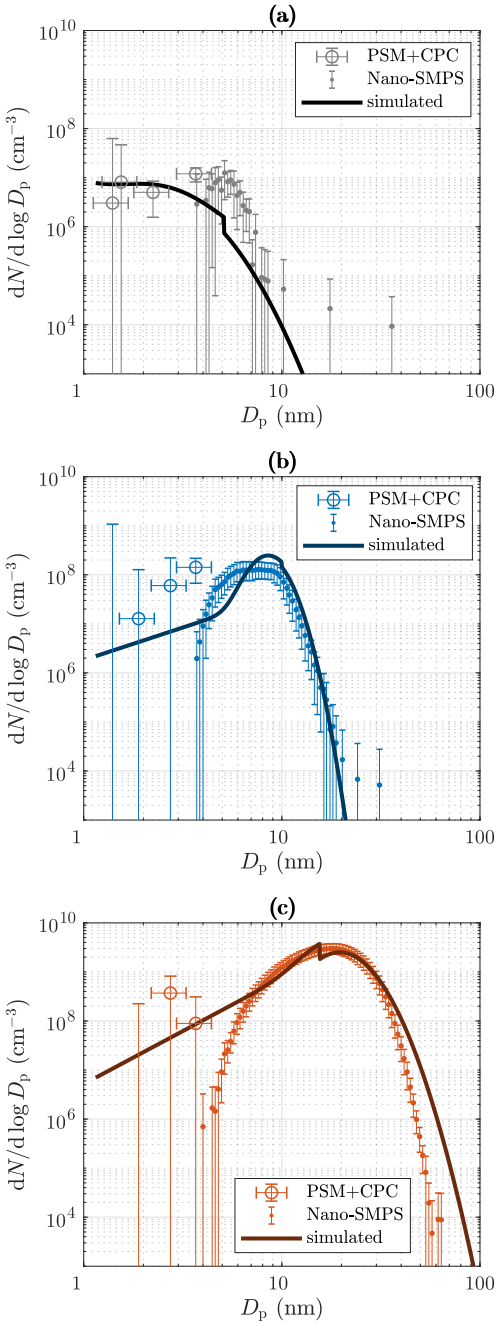

Figure S6. The simulated and measured size distributions for the measurement cases having the T_{sa} of (a) 102 °C, (b) 135.5 °C, and (c) 157.2 °C, as shown in Fig. 11, with the error bars. The error bars for the particle sizes from the Nano-SMPS (±5 %) are not shown for clarity.

2.4 Calculating the error bars for the diameters with the average mass

The diameter with the average mass of a distribution is calculated by

$$D_{\bar{m}} = \left(\frac{M'}{N}\right)^{\frac{1}{3}} = \left(\frac{\sum_i^{\mathrm{PC}} \nu(D_{\mathrm{p},i}) \cdot \mathrm{d}\log D_{\mathrm{p},i} \cdot D_{\mathrm{p},i}^3 + \sum_i^{\mathrm{NS}} \nu(D_{\mathrm{p},i}) \cdot \mathrm{d}\log D_{\mathrm{p},i} \cdot D_{\mathrm{p},i}^3}{\sum_i \nu(D_{\mathrm{p},i}) \cdot \mathrm{d}\log D_{\mathrm{p},i}}\right)^{\frac{1}{3}} = \left(\frac{M'_{\mathrm{PC}} + M'_{\mathrm{NS}}}{N}\right)^{\frac{1}{3}} \tag{S9}$$

where M' is the third moment of the distribution, M'_{PC} and M'_{NS} are the parts of the third moment from the PSM+CPC data and from the Nano-SMPS data, respectively, and N is the total number concentration.

The error bars for $D_{\bar{m}}$ can be calculated with the equation

$$\frac{\Delta D_{\bar{m}}}{D_{\bar{m}}} = \sqrt{\left(\left.\frac{\Delta D_{\bar{m}}}{D_{\bar{m}}}\right|_{\Delta D_{\mathrm{p}}}\right)^2 + \left(\left.\frac{\Delta D_{\bar{m}}}{D_{\bar{m}}}\right|_{\Delta \nu_{\mathrm{s}}}\right)^2 + \left(\left.\frac{\Delta D_{\bar{m}}}{D_{\bar{m}}}\right|_{\Delta \nu_{\mathrm{r}}}\right)^2} \tag{S10}$$

where the first term represents the uncertainty caused by the uncertainty of the interpreted particle diameters, the second term the uncertainty caused by the uncertainty of the number size distribution due to the systematic errors of the devices, and the last term the uncertainty caused by the uncertainty of the number size distribution due to the random error.

The first term in Eq. (S10) is separated to the effects of the PSM+CPC system and of the Nano-SMPS, respectively:

$$\left.\frac{\Delta D_{\bar{m}}}{D_{\bar{m}}}\right|_{\Delta D_{\mathrm{p}}} = \sqrt{\left(\left.\frac{\Delta D_{\bar{m}}}{D_{\bar{m}}}\right|_{\Delta D_{\mathrm{p,PC_1}}}\right)^2 + \left(\left.\frac{\Delta D_{\bar{m}}}{D_{\bar{m}}}\right|_{\Delta D_{\mathrm{p,NS_1}}}\right)^2}. \tag{S11}$$

Because particle diameters are dependent variables for a specific device, i.e., if one diameter is shifted to a direction, other diameters are most probably shifted to the same direction and with almost the same magnitude, the diameters in Eq. (S9) are separated to dependent and independent parts:

$$\begin{aligned} D_{\mathrm{p},i} &= D_{\mathrm{p,PC_1}} \cdot D'_{\mathrm{p},i} \\ D_{\mathrm{p},i} &= D_{\mathrm{p,NS_1}} \cdot D'_{\mathrm{p},i}. \end{aligned} \tag{S12}$$

where $D_{\mathrm{p,PC_1}}$ and $D_{\mathrm{p,NS_1}}$ denote the smallest diameters measured by the PSM+CPC system and by the Nano-SMPS, respectively, and $D'_{\mathrm{p},i}$ is a dimensionless variable denoting the ratios of all other diameters to the smallest diameter. Hence, the third moments can be expressed as

$$\begin{aligned} M'_{\mathrm{PC}} &= \sum_i^{\mathrm{PC}} \nu(D_{\mathrm{p},i}) \cdot \mathrm{d}\log D_{\mathrm{p},i} \cdot D_{\mathrm{p},i}^3 = \sum_i^{\mathrm{PC}} \nu(D_{\mathrm{p},i}) \cdot \mathrm{d}\log D_{\mathrm{p},i} \cdot (D_{\mathrm{p,PC_1}} \cdot D'_{\mathrm{p},i})^3 = D_{\mathrm{p,PC_1}}^3 \cdot \sum_i^{\mathrm{PC}} \nu(D_{\mathrm{p},i}) \cdot \mathrm{d}\log D_{\mathrm{p},i} \cdot D'^3_{\mathrm{p},i} \\ M'_{\mathrm{NS}} &= \sum_i^{\mathrm{NS}} \nu(D_{\mathrm{p},i}) \cdot \mathrm{d}\log D_{\mathrm{p},i} \cdot D_{\mathrm{p},i}^3 = \sum_i^{\mathrm{NS}} \nu(D_{\mathrm{p},i}) \cdot \mathrm{d}\log D_{\mathrm{p},i} \cdot (D_{\mathrm{p,NS_1}} \cdot D'_{\mathrm{p},i})^3 = D_{\mathrm{p,NS_1}}^3 \cdot \sum_i^{\mathrm{NS}} \nu(D_{\mathrm{p},i}) \cdot \mathrm{d}\log D_{\mathrm{p},i} \cdot D'^3_{\mathrm{p},i}. \end{aligned} \tag{S13}$$

The uncertainties in Eq. (S11) can now be calculated by

$$\begin{aligned} \left.\frac{\Delta D_{\bar{m}}}{D_{\bar{m}}}\right|_{\Delta D_{\mathrm{p,PC_1}}} &= \frac{\partial D_{\bar{m}}}{\partial D_{\mathrm{p,PC_1}}} \cdot \frac{\Delta D_{\mathrm{p,PC_1}}}{D_{\bar{m}}} = \frac{1}{3}\frac{D_{\bar{m}}}{M'} \cdot \frac{\partial M'_{\mathrm{PC}}}{\partial D_{\mathrm{p,PC_1}}} \cdot \frac{\Delta D_{\mathrm{p,PC_1}}}{D_{\bar{m}}} = \frac{M'_{\mathrm{PC}}}{M'} \cdot \frac{\Delta D_{\mathrm{p,PC_1}}}{D_{\mathrm{p,PC_1}}} \\ \left.\frac{\Delta D_{\bar{m}}}{D_{\bar{m}}}\right|_{\Delta D_{\mathrm{p,NS_1}}} &= \frac{\partial D_{\bar{m}}}{\partial D_{\mathrm{p,NS_1}}} \cdot \frac{\Delta D_{\mathrm{p,NS_1}}}{D_{\bar{m}}} = \frac{1}{3}\frac{D_{\bar{m}}}{M'} \cdot \frac{\partial M'_{\mathrm{NS}}}{\partial D_{\mathrm{p,NS_1}}} \cdot \frac{\Delta D_{\mathrm{p,NS_1}}}{D_{\bar{m}}} = \frac{M'_{\mathrm{NS}}}{M'} \cdot \frac{\Delta D_{\mathrm{p,NS_1}}}{D_{\mathrm{p,NS_1}}}. \end{aligned} \tag{S14}$$

As 20 and 5 % uncertainties for the diameters for the PSM+CPC system and for the Nano-SMPS, respectively, were estimated, Eq. (S11) becomes

$$\left.\frac{\Delta D_{\bar{m}}}{D_{\bar{m}}}\right|_{\Delta D_\mathrm{p}} = \frac{1}{M'}\sqrt{\left(M'_\mathrm{PC}\cdot 0.2\right)^2 + \left(M'_\mathrm{NS}\cdot 0.05\right)^2}. \tag{S15}$$

The last two terms in Eq. (S10) related to the systematic and random errors separate the errors because the systematic errors for all size bins are presumably to the same direction and in almost the same magnitude and the random errors are randomly directed between different size bins because they are measured at different times. The number size distributions can be separated to the parts involving the sources for the systematic ($\Delta\nu_\mathrm{s}$) and for the random ($\Delta\nu_\mathrm{r}$) errors, respectively, using $\nu = \nu_\mathrm{s}\cdot\nu_\mathrm{r}$. The systematic errors for ν_s are independent variables for the different devices, but dependent variables for the different size bins of a specific device. Hence, the second term in Eq. (S10) is further separated to the PSM+CPC system and to the Nano-SMPS, respectively, using

$$\begin{aligned}\left.\frac{\Delta D_{\bar{m}}}{D_{\bar{m}}}\right|_{\Delta\nu_\mathrm{s}} &= \sqrt{\left(\left.\frac{\Delta D_{\bar{m}}}{D_{\bar{m}}}\right|_{\Delta\nu_{\mathrm{s,PC}}}\right)^2 + \left(\left.\frac{\Delta D_{\bar{m}}}{D_{\bar{m}}}\right|_{\Delta\nu_{\mathrm{s,NS}}}\right)^2} \\ &= \sqrt{\left[\frac{D_{\bar{m}}\left(\nu+\Delta\nu_{\mathrm{s,PC}}\right) - D_{\bar{m}}\left(\nu-\Delta\nu_{\mathrm{s,PC}}\right)}{2D_{\bar{m}}}\right]^2 + \left[\frac{D_{\bar{m}}\left(\nu+\Delta\nu_{\mathrm{s,NS}}\right) - D_{\bar{m}}\left(\nu-\Delta\nu_{\mathrm{s,NS}}\right)}{2D_{\bar{m}}}\right]^2}.\end{aligned} \tag{S16}$$

The last term in Eq. (S10), related to the random error, is calculated by

$$\begin{aligned}\left.\frac{\Delta D_{\bar{m}}}{D_{\bar{m}}}\right|_{\Delta\nu_\mathrm{r}} &= \sqrt{\sum_i\left[\frac{\partial D_{\bar{m}}}{\partial\nu_\mathrm{r}(D_{\mathrm{p},i})}\cdot\frac{\Delta\nu_\mathrm{r}(D_{\mathrm{p},i})}{D_{\bar{m}}}\right]^2} = \sqrt{\sum_i\left[\left(\frac{1}{3M'}\frac{\partial M'}{\partial\nu_\mathrm{r}(D_{\mathrm{p},i})} - \frac{1}{3N}\frac{\partial N}{\partial\nu_\mathrm{r}(D_{\mathrm{p},i})}\right)\Delta\nu_\mathrm{r}(D_{\mathrm{p},i})\right]^2} \\ &= \frac{1}{3}\sqrt{\sum_i\left[\left(\frac{\mathrm{d}\log D_{\mathrm{p},i}\cdot D_{\mathrm{p},i}^3}{M'} - \frac{\mathrm{d}\log D_{\mathrm{p},i}}{N}\right)\Delta\nu_\mathrm{r}(D_{\mathrm{p},i})\right]^2}.\end{aligned} \tag{S17}$$

The calculated error bars for the diameters with the average mass are presented in Fig. 13.

References

Adachi, M., Kousaka, Y., and Okuyama, K.: Unipolar and bipolar diffusion charging of ultrafine aerosol particles, J. Aerosol Sci., 16, 109 – 123, https://doi.org/https://doi.org/10.1016/0021-8502(85)90079-5, http://www.sciencedirect.com/science/article/pii/0021850285900795, 1985.

Alonso, M., Kousaka, Y., Nomura, T., Hashimoto, N., and Hashimoto, T.: Bipolar charging and neutralization of nanometer-sized aerosol particles, J. Aerosol Sci., 28, 1479 – 1490, https://doi.org/https://doi.org/10.1016/S0021-8502(97)00036-0, http://www.sciencedirect.com/science/article/pii/S0021850297000360, 1997.

de La Verpilliere, J. L., Swanson, J. J., and Boies, A. M.: Unsteady bipolar diffusion charging in aerosol neutralisers: A non-dimensional approach to predict charge distribution equilibrium behaviour, J. Aerosol Sci., 86, 55 – 68, https://doi.org/https://doi.org/10.1016/j.jaerosci.2015.03.006, http://www.sciencedirect.com/science/article/pii/S0021850215000440, 2015.

Gormley, P. G. and Kennedy, M.: Diffusion from a Stream Flowing through a Cylindrical Tube, P. Roy. Irish Acad. A, 52, 163–169, https://doi.org/10.2307/20488498, 1948.

Hermann, M., Wehner, B., Bischof, O., Han, H.-S., Krinke, T., Liu, W., Zerrath, A., and Wiedensohler, A.: Particle counting efficiencies of new TSI condensation particle counters, J. Aerosol Sci., 38, 674 – 682, https://doi.org/https://doi.org/10.1016/j.jaerosci.2007.05.001, http://www.sciencedirect.com/science/article/pii/S0021850207000705, 2007.

Hussin, A., Scheibel, H., Becker, K., and Porstendörfer, J.: Bipolar diffusion charging of aerosol particles—I: experimental results within the diameter range 4–30 nm, J. Aerosol Sci., 14, 671 – 677, https://doi.org/https://doi.org/10.1016/0021-8502(83)90071-X, http://www.sciencedirect.com/science/article/pii/002185028390071X, 1983.

Jokinen, T., Sipilä, M., Junninen, H., Ehn, M., Lönn, G., Hakala, J., Petäjä, T., Mauldin III, R. L., Kulmala, M., and Worsnop, D. R.: Atmospheric sulphuric acid and neutral cluster measurements using CI-APi-TOF, Atmos. Chem. Phys., 12, 4117–4125, https://doi.org/10.5194/acp-12-4117-2012, 2012.

Lehtipalo, K., Leppä, J., Kontkanen, J., Kangasluoma, J., Franchin, A., Wimmer, D., Schobesberger, S., Junninen, H., Petäjä, T., Sipilä, M., Mikkilä, J., Vanhanen, J., Worsnop, D., and Kulmala, M.: Methods for determining particle size distribution and growth rates between 1 and 3 nm using the Particle Size Magnifier, Bor. Env. Res., 19, 215–236, https://doi.org/10.1029/2001JD001010, 2014.

Mordas, G., Manninen, H., Petäjä, T., Aalto, P., Hämeri, K., and Kulmala, M.: On operation of the ultra-fine water-based CPC TSI 3786 and comparison with other TSI models (TSI 3776, TSI 3772, TSI 3025, TSI 3010, TSI 3007), Aerosol Sci. Tech., 42, 152–158, https://doi.org/10.1080/02786820701846252, 2008.

Sulonen, M. L., Kokko, M. E., Lakaniemi, A.-M., and Puhakka, J. A.: Electricity generation from tetrathionate in microbial fuel cells by acidophiles, J. Hazard. Mater., 284, 182–189, https://doi.org/10.1016/j.jhazmat.2014.10.045, 2015.

Tröstl, J., Chuang, W. K., Gordon, H., Heinritzi, M., Yan, C., Molteni, U., Ahlm, L., Frege, C., Bianchi, F., Wagner, R., Simon, M., Lehtipalo, K., Williamson, C., Craven, J. S., Duplissy, J., Adamov, A., Almeida, J., Bernhammer, A.-K., Breitenlechner, M., Brilke, S., Dias, A., Ehrhart, S., Flagan, R. C., Franchin, A., Fuchs, C., Guida, R., Gysel, M., Hansel, A., Hoyle, C. R., Jokinen, T., Junninen, H., Kangasluoma, J., Keskinen, H., Kim, J., Krapf, M., Kürten, A., Laaksonen, A., Lawler, M., Leiminger, M., Mathot, S., Möhler, O., Nieminen, T., Onnela, A., Petäjä, T., Piel, F. M., Miettinen, P., Rissanen, M. P., Rondo, L., Sarnela, N., Schobesberger, S., Sengupta, K., Sipilä, M., Smith, J. N., Steiner, G., Tomè, A., Virtanen, A., Wagner, A. C., Weingartner, E., Wimmer, D., Winkler, P. M., Ye, P., Carslaw, K. S., Curtius, J., Dommen, J., Kirkby, J., Kulmala, M., Riipinen, I., Worsnop, D. R., Donahue, N. M., and Baltensperger, U.: The role of low-volatility organic compounds in initial particle growth in the atmosphere, Nature, 533, 527–531, https://doi.org/10.1038/nature18271, 2016.

Wiedensohler, A.: An approximation of the bipolar charge distribution for particles in the submicron size range, J. Aerosol Sci., 19, 387 – 389, https://doi.org/https://doi.org/10.1016/0021-8502(88)90278-9, http://www.sciencedirect.com/science/article/pii/0021850288902789, 1988.

Wiedensohler, A., Lütkemeier, E., Feldpausch, M., and Helsper, C.: Investigation of the bipolar charge distribution at various gas conditions, J. Aerosol Sci., 17, 413 – 416, https://doi.org/https://doi.org/10.1016/0021-8502(86)90118-7, http://www.sciencedirect.com/science/article/pii/0021850286901187, 1986.

Wiedensohler, A., Birmili, W., Nowak, A., Sonntag, A., Weinhold, K., Merkel, M., Wehner, B., Tuch, T., Pfeifer, S., Fiebig, M., Fjäraa, A. M., Asmi, E., Sellegri, K., Depuy, R., Venzac, H., Villani, P., Laj, P., Aalto, P., Ogren, J. A., Swietlicki, E., Williams, P., Roldin, P., Quincey, P., Hüglin, C., Fierz-Schmidhauser, R., Gysel, M., Weingartner, E., Riccobono, F., Santos, S., Grüning, C., Faloon, K., Beddows, D., Harrison, R., Monahan, C., Jennings, S. G., O'Dowd, C. D., Marinoni, A., Horn, H.-G., Keck, L., Jiang, J., Scheckman, J., McMurry, P. H., Deng, Z., Zhao, C. S., Moerman, M., Henzing, B., de Leeuw, G., Löschau, G., and Bastian, S.: Mobility particle size spectrometers: harmonization of technical standards and data structure to facilitate high quality long-term observations of atmospheric particle number size distributions, Atmos. Meas. Tech., 5, 657–685, https://doi.org/10.5194/amt-5-657-2012, https://www.atmos-meas-tech.net/5/657/2012/, 2012.